AD-A268 355

8000180

Atlas of Formability,

Haynes 188,
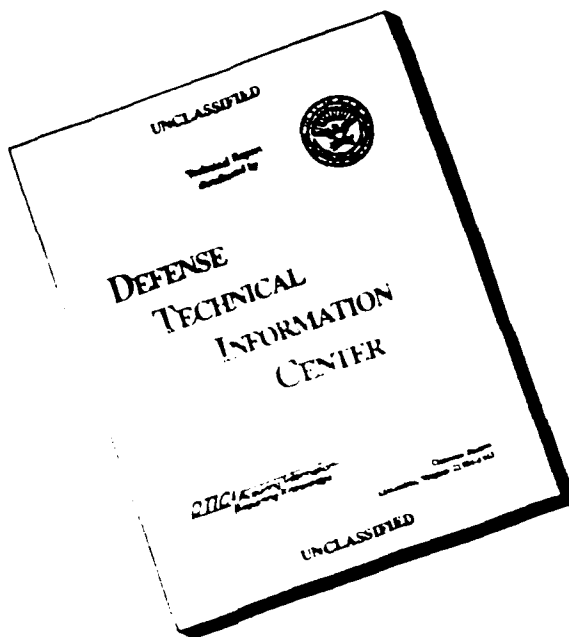
DTIC
ELECTE
AUG 18 1993
S B D

93-18963

NCEMT

93 8 16 032

DISCLAIMER NOTICE

THIS DOCUMENT IS BEST QUALITY AVAILABLE. THE COPY FURNISHED TO DTIC CONTAINED A SIGNIFICANT NUMBER OF PAGES WHICH DO NOT REPRODUCE LEGIBLY.

ATLAS OF FORMABILITY

HAYNES 188

by

Prabir K. Chaudhury and Dan Zhao

National Center for Excellence in Metalworking Technology
1450 Scalp Avenue
Johnstown, PA 15904

for

Naval Industrial Resource Support Activity
Building 75-2, Naval Base
Philadelphia, PA 19112-5078

February 28, 1993

REPORT DOCUMENTATION PAGE

Public reporting burden for this collection of information is estimated to average 1 hour per response, including the time for reviewing instructions, searching existing data sources, gathering and maintaining the data needed, and completing and reviewing the collection of information. Send comments regarding this burden estimate or any other aspect of this collection of information, including suggestions for reducing this burden, to Washington Headquarters Services, Directorate for Information Operations and Reports, 1215 Jefferson Davis Highway, Suite 1204, Arlington, VA 22202-4302, and to the Office of Management and Budget, Paperwork Reduction Project (0704-0188), Washington, DC 20503.

1. AGENCY USE ONLY (Leave blank)	2. REPORT DATE February 28, 1993	3. REPORT TYPE AND DATES COVERED Final, Nov. 30, 1992 - Feb. 28, 1993

4. TITLE AND SUBTITLE

ATLAS OF FORMABILITY
HAYNES 188

5. FUNDING NUMBERS

C-N00140-88-C-RC21

6. AUTHOR(S)

Prabir K. Chaudhury
Dan Zhao

7. PERFORMING ORGANIZATION NAME(S) AND ADDRESS(ES)

National Center for Excellence in Metalworking Technology (NCEMT)
1450 Scalp Avenue
Johnstown, PA 15904

8. PERFORMING ORGANIZATION REPORT NUMBER

9. SPONSORING / MONITORING AGENCY NAME(S) AND ADDRESS(ES)

Naval Industrial Resources Support Activity
Building 75-2, Naval Base
Philadelphia, PA 19112-5078

10. SPONSORING / MONITORING AGENCY REPORT NUMBER

11. SUPPLEMENTARY NOTES

12a. DISTRIBUTION / AVAILABILITY STATEMENT

12b. DISTRIBUTION CODE

13. ABSTRACT (Maximum 200 words)

In this investigation, flow behavior of Haynes 188 alloy was studied by conducting compression tests over a wide range of temperatures (950 - 1200 C) and strain rates (0.001 - 20 s^{-1}). The true stress-true strain flow curves are presented for each test condition. Constitutive relations were determined from the flow behavior, and a dynamic material modeling was performed on this alloy. Thus, the optimum processing condition in terms of temperature and strain rate was identified as 1100 C and 0.001 s^{-1} for this alloy. Microstructural changes during high temperature deformation were also characterized, and selective micrographs are presented together with corresponding flow curves. Dynamic recrystallization and grain growth occurred during high temperature deformation over the range of temperatures tested. This report supplies ample mechanical and microstructural data on Haynes 188 alloy for engineers in the field of metalworking process design. The data presented here are also very helpful in finite element analysis of metalworking processes.

14. SUBJECT TERMS

Haynes 188, Deformation Processing, High Temperature Deformation, Processing Map, Metalworking, Deformed Microstructure

15. NUMBER OF PAGES

68

16. PRICE CODE

17. SECURITY CLASSIFICATION OF REPORT	18. SECURITY CLASSIFICATION OF THIS PAGE	19. SECURITY CLASSIFICATION OF ABSTRACT	20. LIMITATION OF ABSTRACT
Unclassified	Unclassified	Unclassified	

TABLE OF CONTENTS

ST #A, AUTH USNAVIRSA (MR PLONSKY 8/443-6684)
PER TELECON, 17 AUG 93 CB

LIST OF TABLE

Haynes 188

Introduction

Haynes 188 alloy combines excellent high temperature strength with very good resistance to oxidizing environments up to 1095 C. The alloy also has good forming and welding characteristics, but work-hardens rapidly. The understanding of mechanical and microstructural behavior during high temperature deformation is very important for the forming processes of this material. In this investigation, flow behavior of Haynes 188 was studied by conducting compression tests over a wide range of temperatures and strain rates. Constitutive relations were determined from the flow behavior and subsequently, a dynamic material modeling for this alloy was performed. Thus, the optimum processing condition in terms of temperature and strain rate was determined. Microstructural changes during high temperature deformation were also characterized to help process design engineers select processing conditions for desired microstructure.

Experimental Procedure

The material used in this investigation was commercially available Haynes 188 wrought bars in annealed condition with approximately 16 mm diameter. The typical microstructure of the as-received material is shown in Figure 1. The chemical composition is as follows (wt%, bal. Co):

C	S	Mn	Si	Cr	B	Fe	Ni	W	P
0.11	<0.002	0.78	0.41	22.04	0.004	2.20	22.67	13.81	0.014

Cylindrical compression test specimens with a diameter of 12.7 mm and a height of 15.9 mm were machined from the bars. Isothermal compression tests were conducted in vacuum on an MTS testing machine. The test matrix was as follows:

Temperature, C (F): 950 (1742), 1000 (1832), 1050 (1922), 1100 (2012), 1150 (2102), 1175 (2147), and 1200 (2192);

Strain rate, s^{-1}: 0.001, 0.01, 0.05, 0.1, 0.5, 1, 5 and 20.

Load and stroke data were acquired during the tests by a computer and later converted to true stress-true strain curves. Immediately after the compression test, the specimens were quenched with forced helium gas in order to retain the deformed microstructure. Longitudinal sections of the specimens were examined by optical microscopy. The photomicrographs were taken from the center of the longitudinal section of the specimens.

Results

Table 1 is a list of the figures, test conditions, and the observed microstructures. The true stress-true strain flow curves with selective corresponding deformed microstructure are shown in Figure 2 to Figure 57. True stress versus strain rate was plotted in log-log scale in Figure 58 at a true strain of 0.5. The slope of the plot gives the strain rate sensitivity m, which is not constant over the range of temperatures and strain rates tested. Log stress vs. 1/T at the same true strain is shown in Figure 59. A processing map at this strain was developed and is shown in Figure 60. The optimum processing condition from the map can be obtained by selecting the temperature and strain rate combination which provides the maximum efficiency in the stable region. This condition is approximately 1100 C and 10^{-3} s^{-1} for this material.

Table 1. List of figures, testing conditions and microstructural observations for Haynes 188.

Figure No	Temperature C (F)	Strain Rate s⁻¹	Microstructure Optical Microscopy	Page No
1	As received		Equiaxed grains with an average size of 54.4 μm, multiple twins in some grains and presence of precipitates.	4
2	950 (1742)	0.001	Deformed grains with an average size of 59 μm, ~30% dynamically recrystallized (DRX) grains with <2 μm in size surrounding the large deformed grains, presence of fine precipitates.	5
3	950 (1742)	0.01		6
4	950 (1742)	0.05	Same as above, but with some twins.	7
5	950 (1742)	0.1	Elongated grains with an average size of 55.3 μm, ~20% recrystallized grains with < 2 μm in size.	8
6	950 (1742)	0.5		9
7	950 (1742)	1	Severely deformed grains with ~ 50% DRX grains (<2 μm in size) and some necklacing at the grain boundaries.	10
8	950 (1742)	5		11
9	950 (1742)	20	Same as above, but with less amount of recrystallized grains (~10%) and presence of substructure.	12
10	1000 (1882)	0.001	Deformed grains with serrated boundaries and ~100% substructure formation.	13
11	1000 (1882)	0.01	Same as above but with less substructure formation.	14
12	1000 (1882)	0.05		15
13	1000 (1882)	0.1		16
14	1000 (1882)	0.5	Severely deformed grains with ~80% DRX (< 4 μm grain size) presence of deformed original grain boundaries.	17
15	1000 (1882)	1	Same as above.	18
16	1000 (1882)	5		19
17	1000 (1882)	20	Same as above but with ~60% DRX.	20
18	1050 (1922)	0.001	~90% DRX (~8 μm grain size), the deformed original grain boundaries hardly visible.	21
19	1050 (1922)	0.01		22
20	1050 (1922)	0.05	Large severely deformed grains with ~80% DRX, presence of deformed origianl grain boundaries.	23
21	1050 (1922)	0.1		24
22	1050 (1922)	0.5		25
23	1050 (1922)	1	Same as above, but with less amount of DRX.	26
24	1050 (1922)	5	Same as above.	27
25	1050 (1922)	20	Same as above.	28
26	1100 (1212)	0.001	100% DRX equiaxed grains (average grain size of 8.2 ± 0.9 μm).	29
27	1100 (1212)	0.01	Same as above, but with a larger grain size.	30
28	1100 (1212)	0.05		31
29	1100 (1212)	0.1	100% DRX equiaxed grains (7.7 ± 0.7 μm in size) within the large deformed originalgrains.	32
30	1100 (1212)	0.5		33
31	1100 (1212)	1	~80% DRX grains (~6.5 μm in size) within the large deformed grains, some substructure formation .	34

32	1100 (1212)	5		35
33	1100 (1212)	20	100% DRX equiaxed grains (~6.1 μm in size) within the severely deformed grains.	36
34	1150 (2102)	0.001	100% DRX grains (~40 μm in size), some multiple twins and evenly dispersed fine precipitates.	37
35	1150 (2102)	0.01	Same as above, but with ~25 μm DRX grains.	38
36	1150 (2102)	0.05		39
37	1150 (2102)	0.1		40
38	1150 (2102)	0.5	100% equiaxed uniform sized grains with no evidence of prior grain boundaries.	41
39	1150 (2102)	1	Same as above but with ~15 μm DRX grain size.	42
40	1150 (2102)	5		43
41	1150 (2102)	20	Same as above, but with ~10 μm in grain size and some twinning.	44
42	1175 (2147)	0.001	100% DRX and grown grains with ~55 μm in size, some multiple twinning and evenly distributed fine precipitates.	45
43	1175 (2147)	0.01		46
44	1175 (2147)	0.05	Same as above, but with ~20 μm grain size.	47
45	1175 (2147)	0.1		48
46	1175 (2147)	0.5		49
47	1175 (2147)	1	100% DRX with non-uniform sized grains (average ~15 μm), multiple twins in some grains and evenly distributed fine precipitates.	50
48	1175 (2147)	5	Same as above with more regular grain size.	51
49	1175 (2147)	20	Same as above with even more uniformly sized grains.	52
50	1200 (2192)	0.001	100% DRX and grown equiaxed grain with an average size of 67.6 ± 15.7 μm, multiple twins in some grains and considerably less amount of fine precipitates.	53
51	1200 (2192)	0.01	Same as above, but with smaller (~40 μm) DRX grain size.	54
52	1200 (2192)	0.05		55
53	1200 (2192)	0.1	100% DRX and grown non-uniform sized grains (average ~30.5 ± 3.4 μm) with much twinning.	56
54	1200 (2192)	0.5		57
55	1200 (2192)	1	Same as above with ~ 30 μm grain size.	58
56	1200 (2192)	5		59
57	1200 (2192)	20	Same as above with ~ 26 ± 1.9 μm grain size.	60
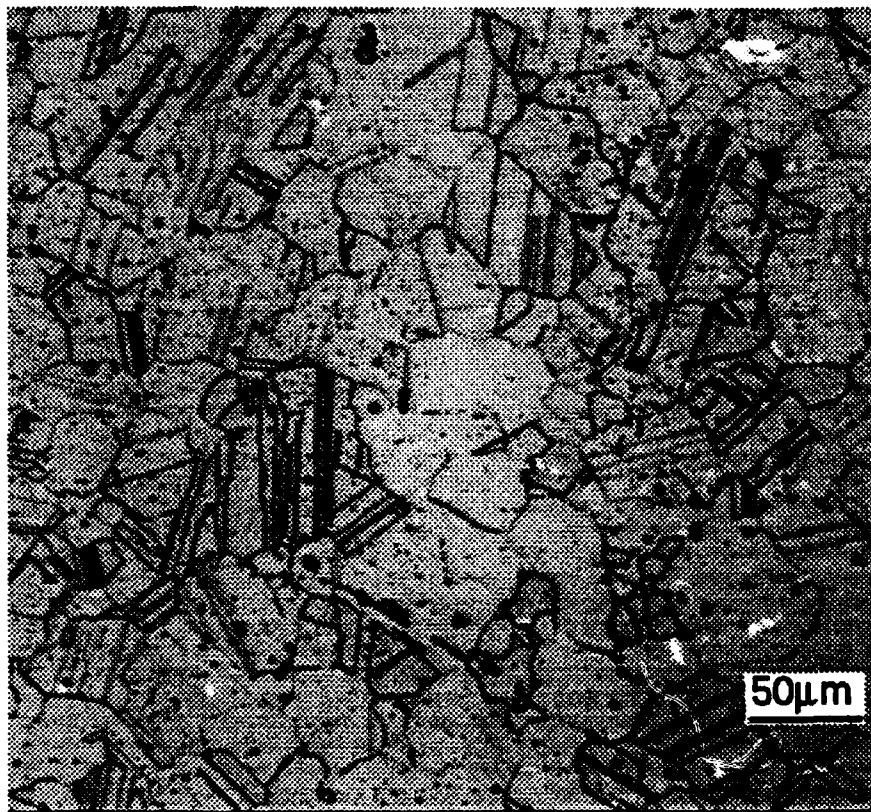
Figure 1. As-received microstructure of Haynes 188.
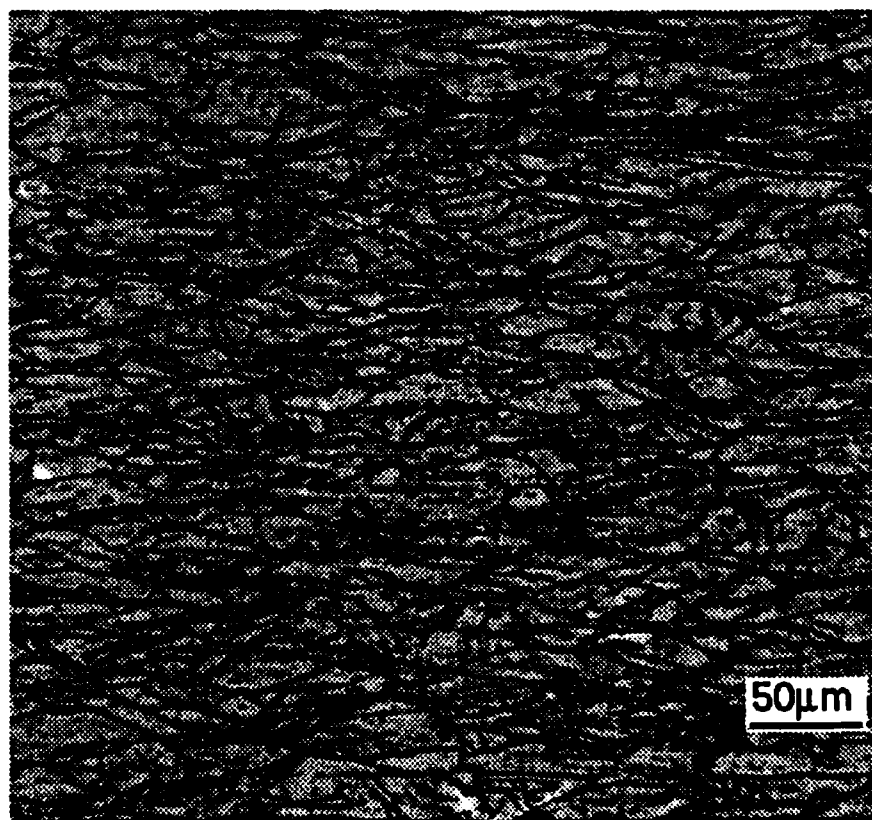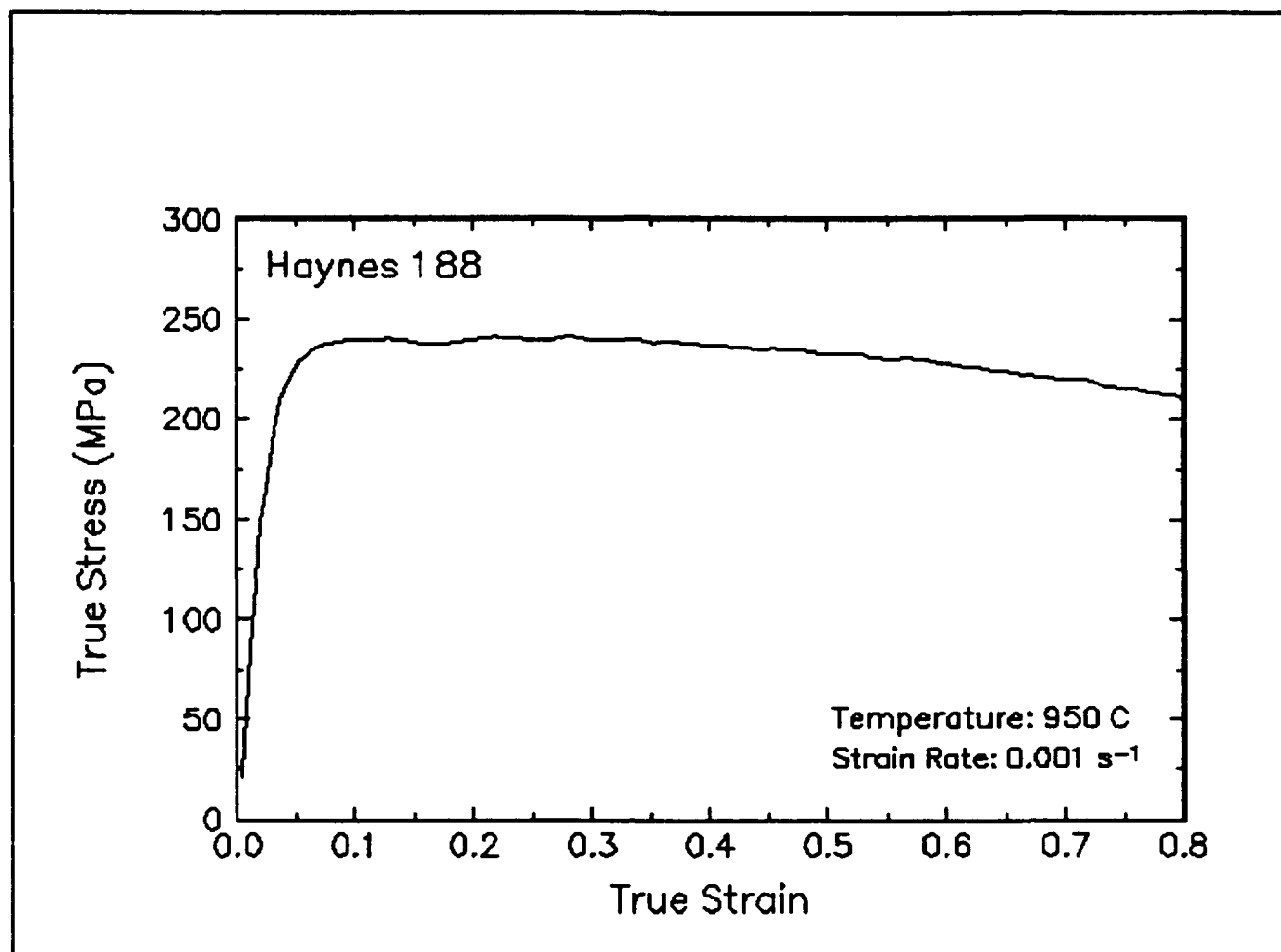
Figure 2. True stress-true strain curve and an optical micrograph from the center of the compressed sample cut through the compression axis, 950 C and 0.001 s⁻¹.
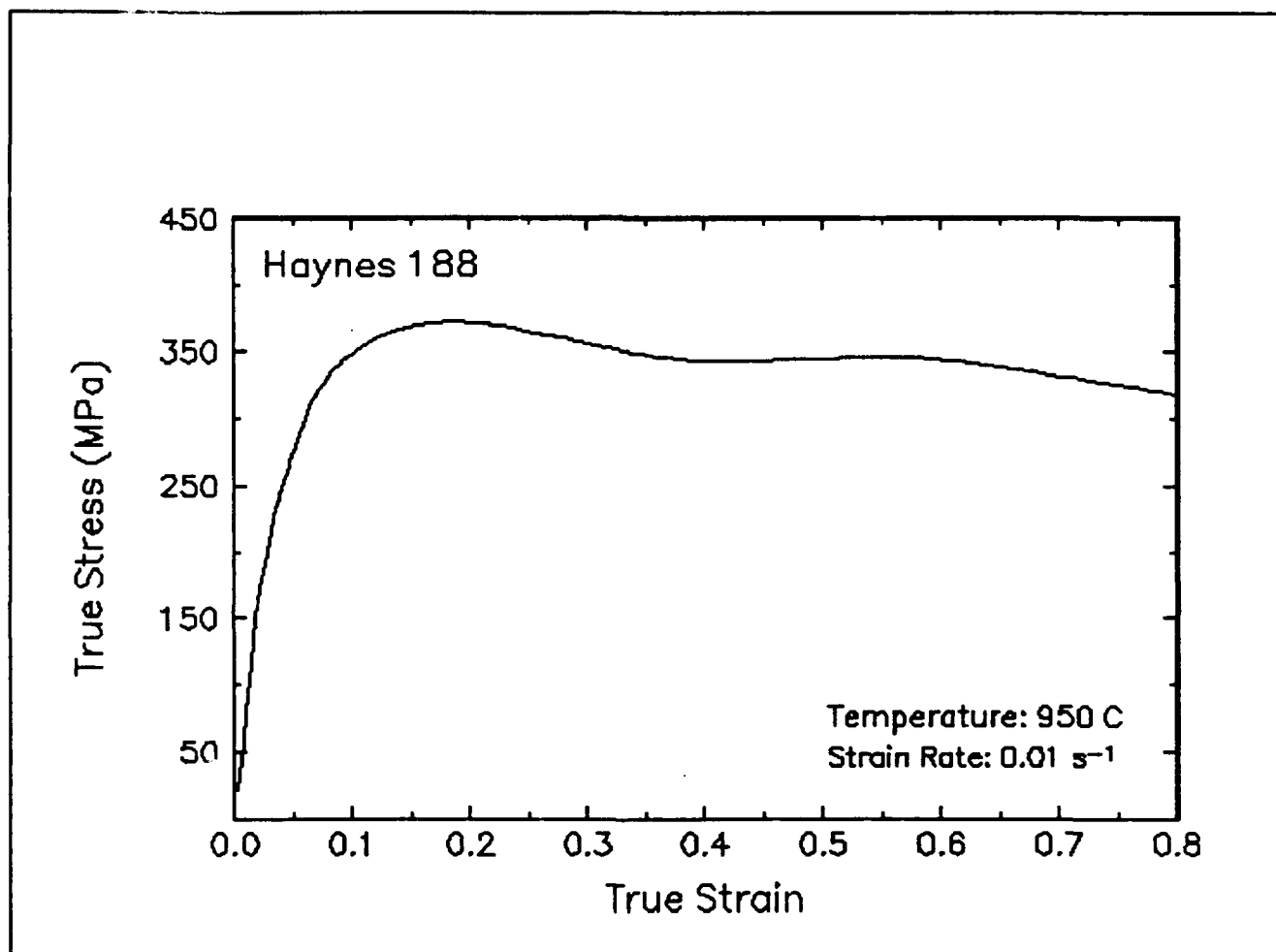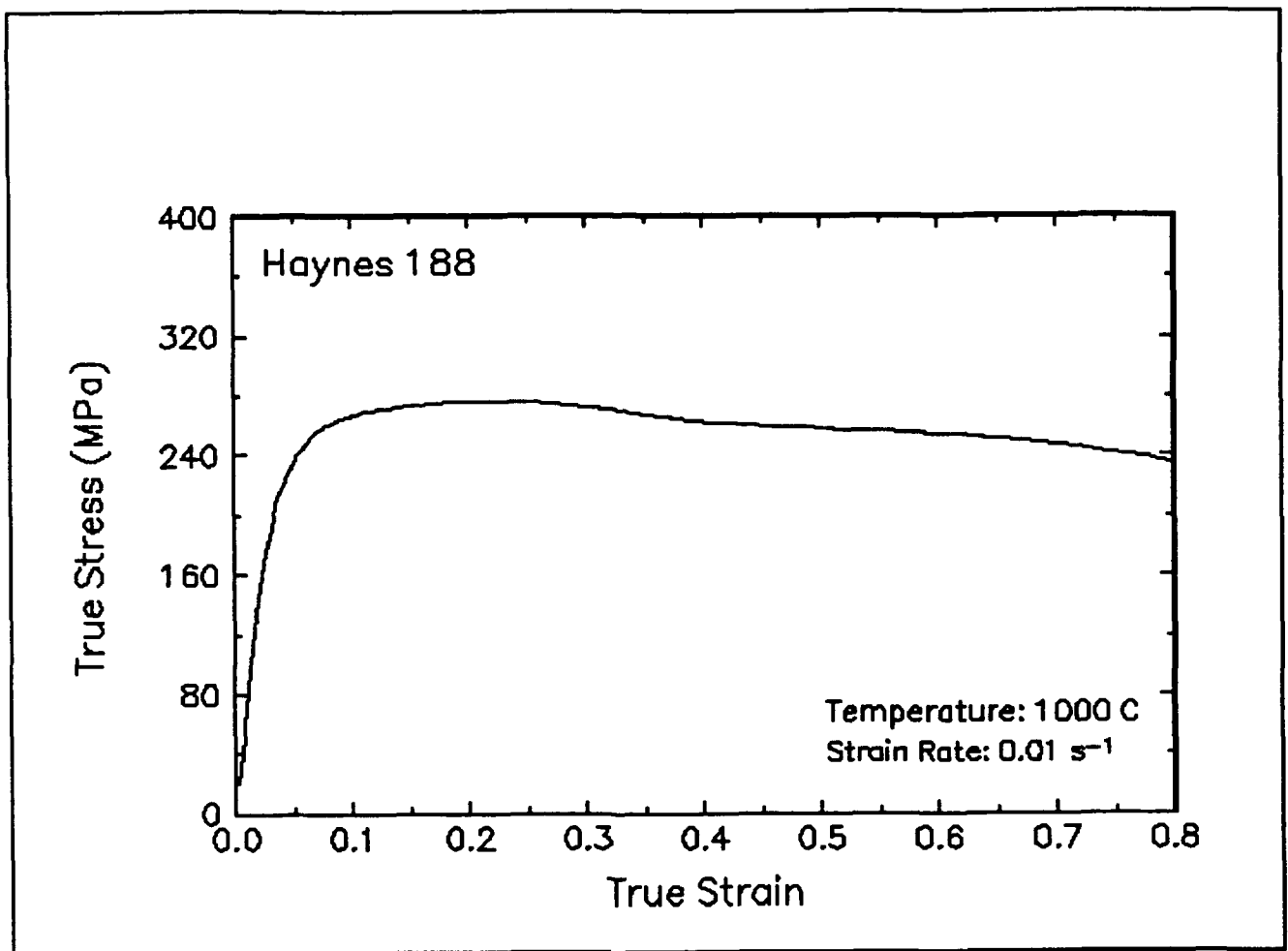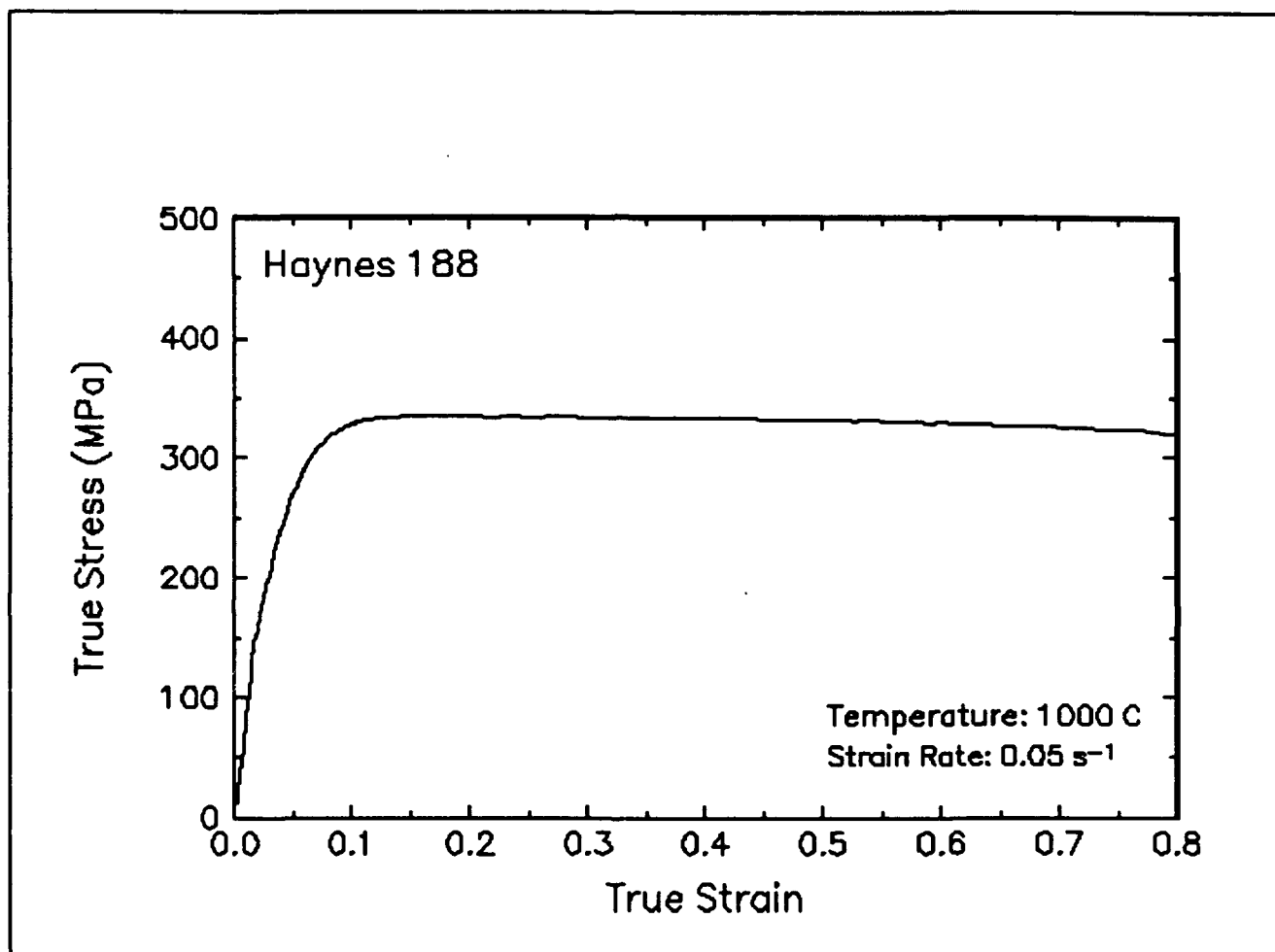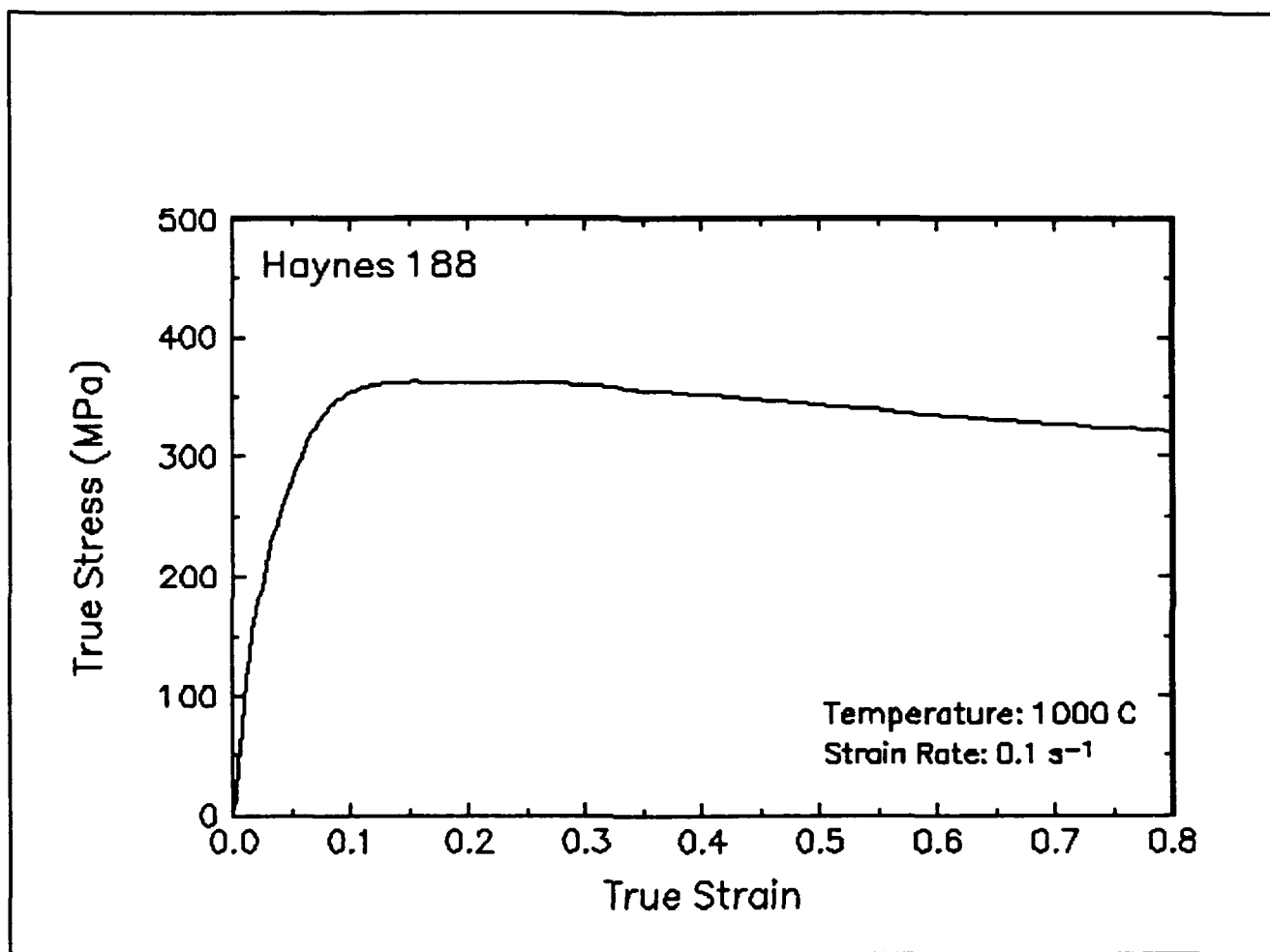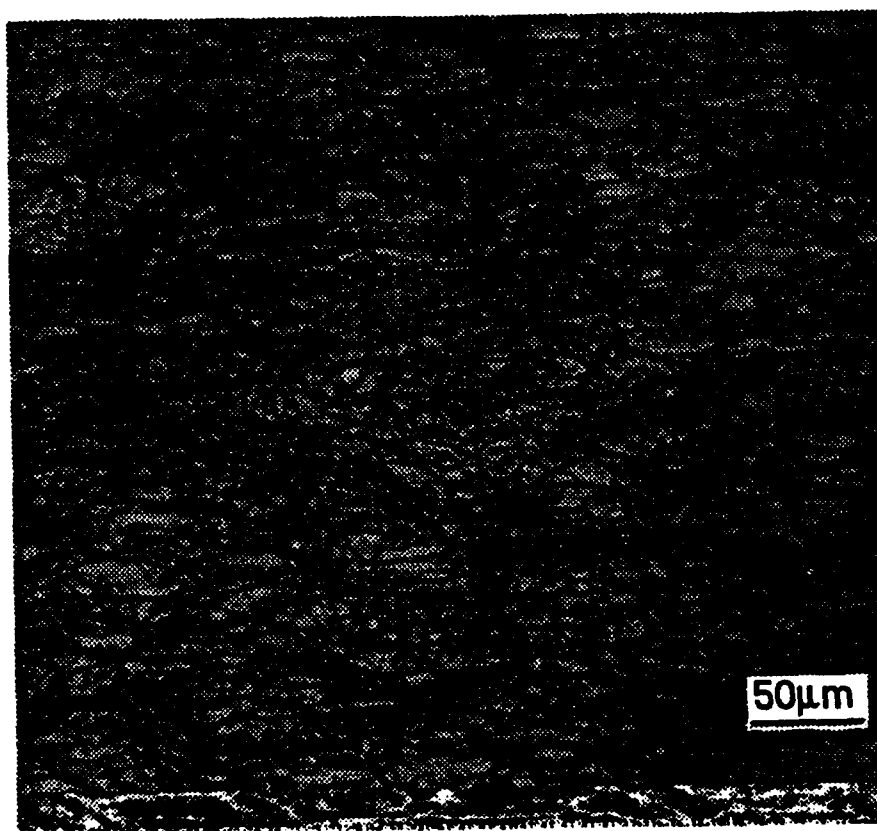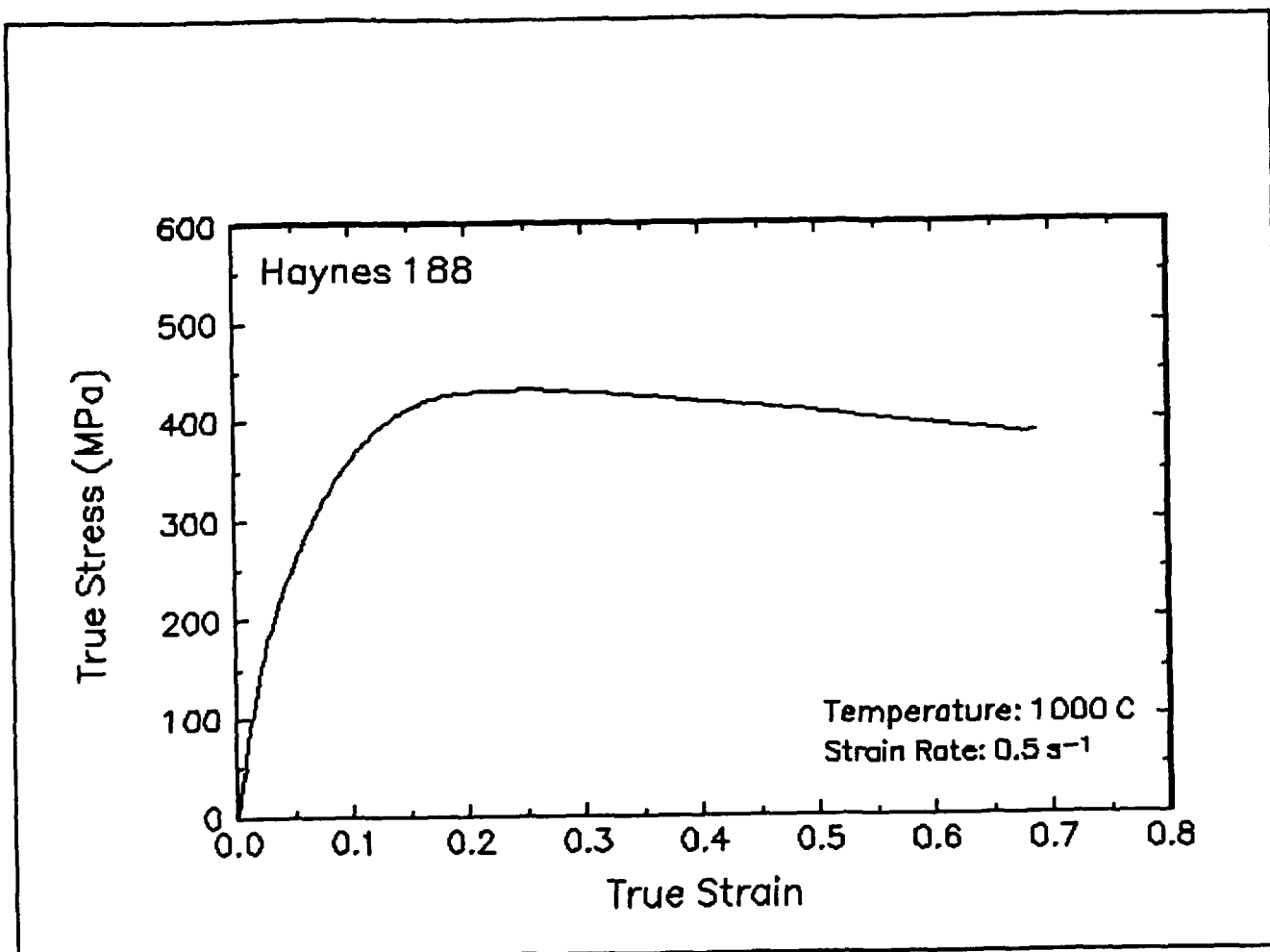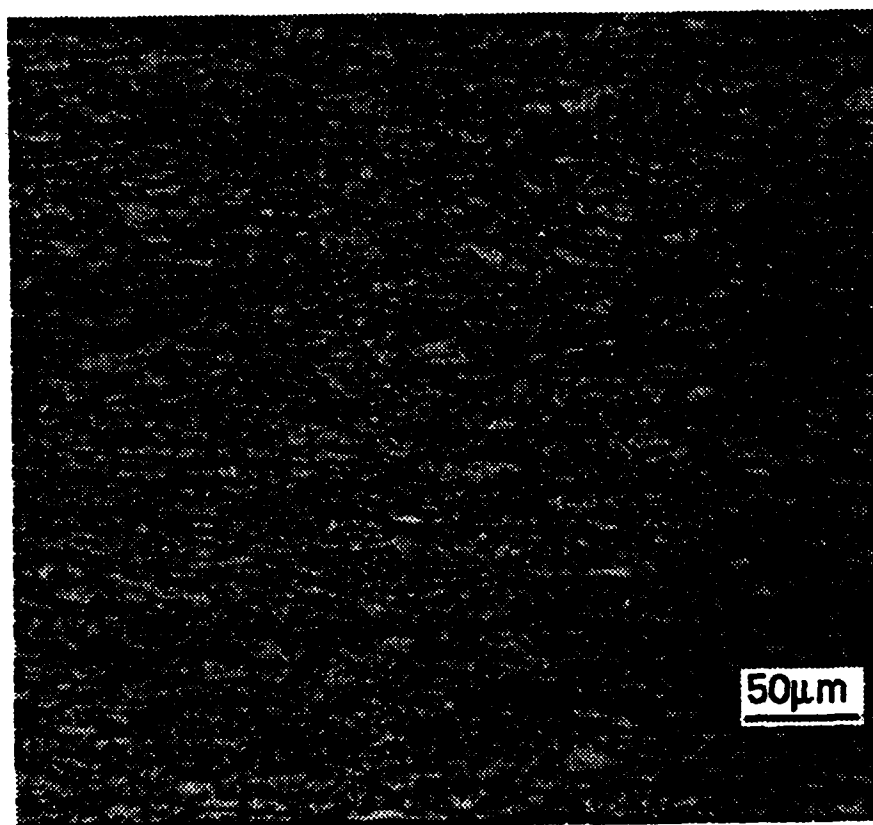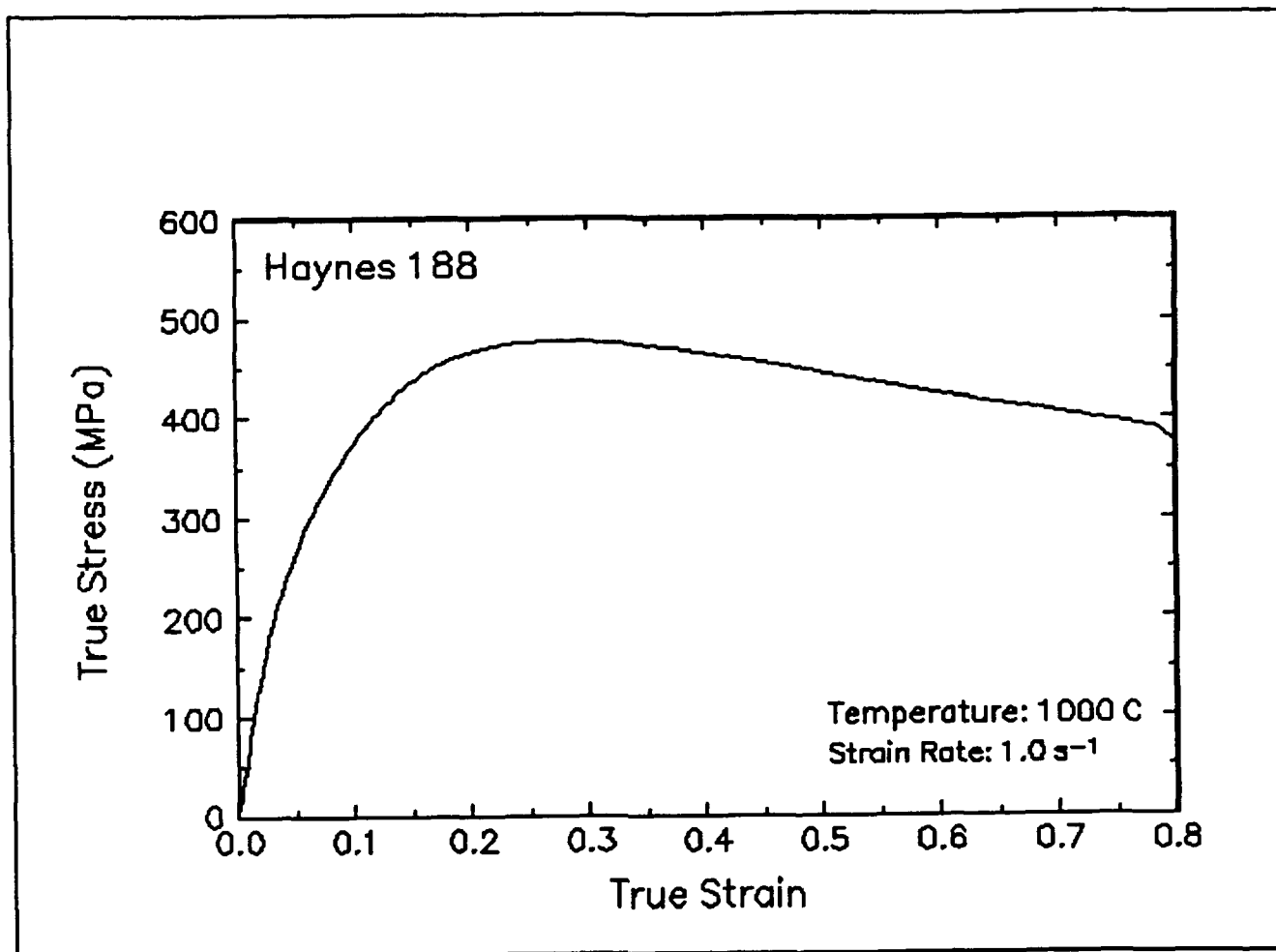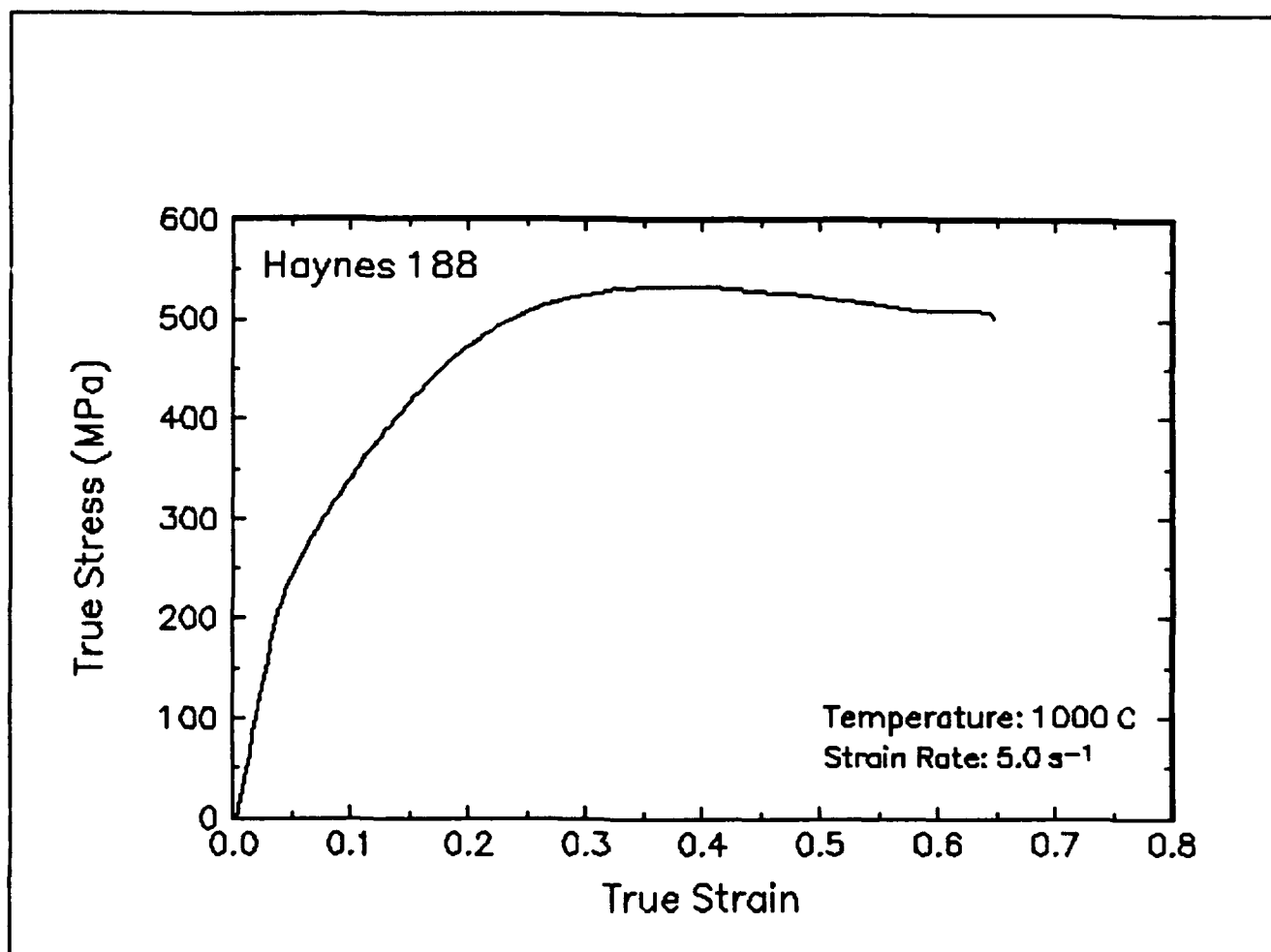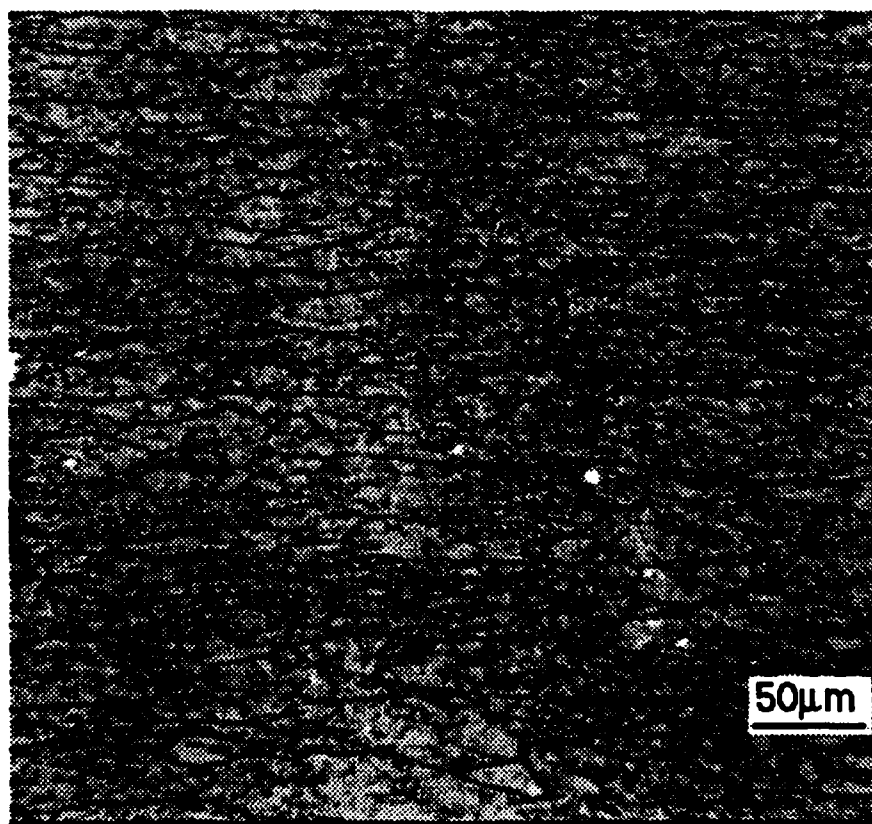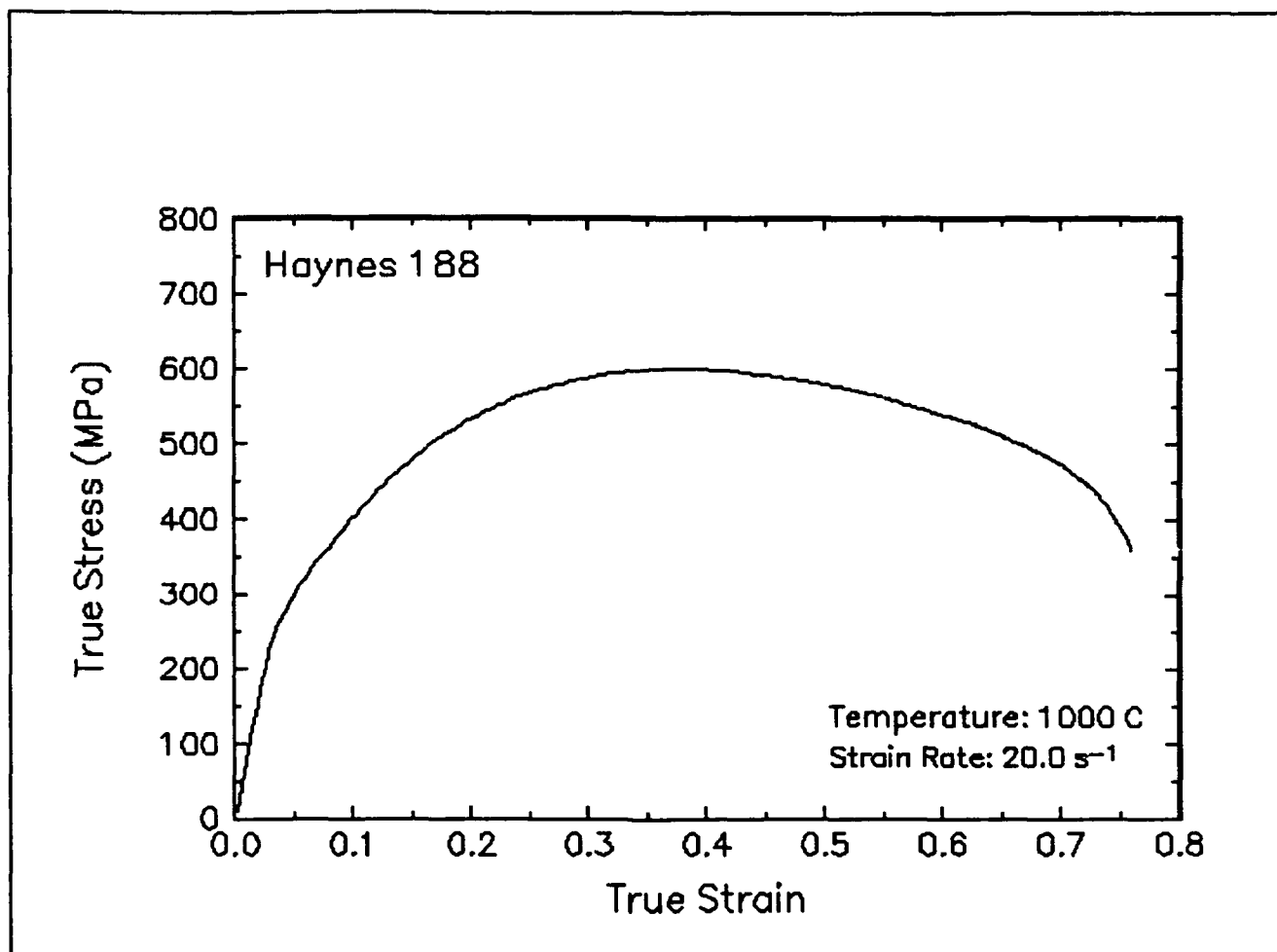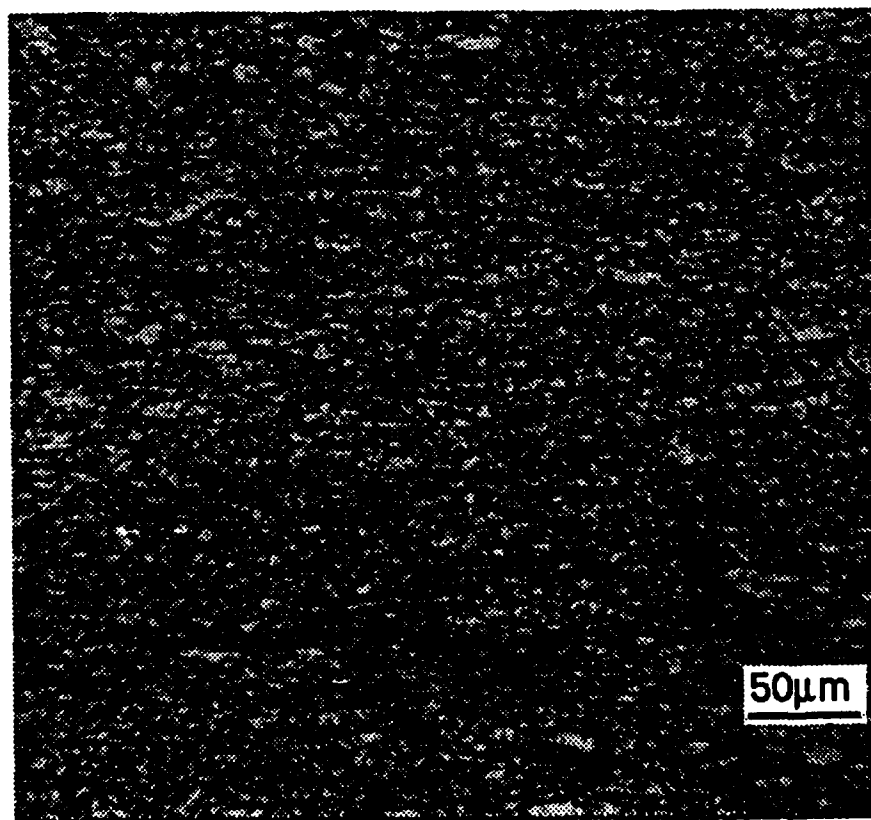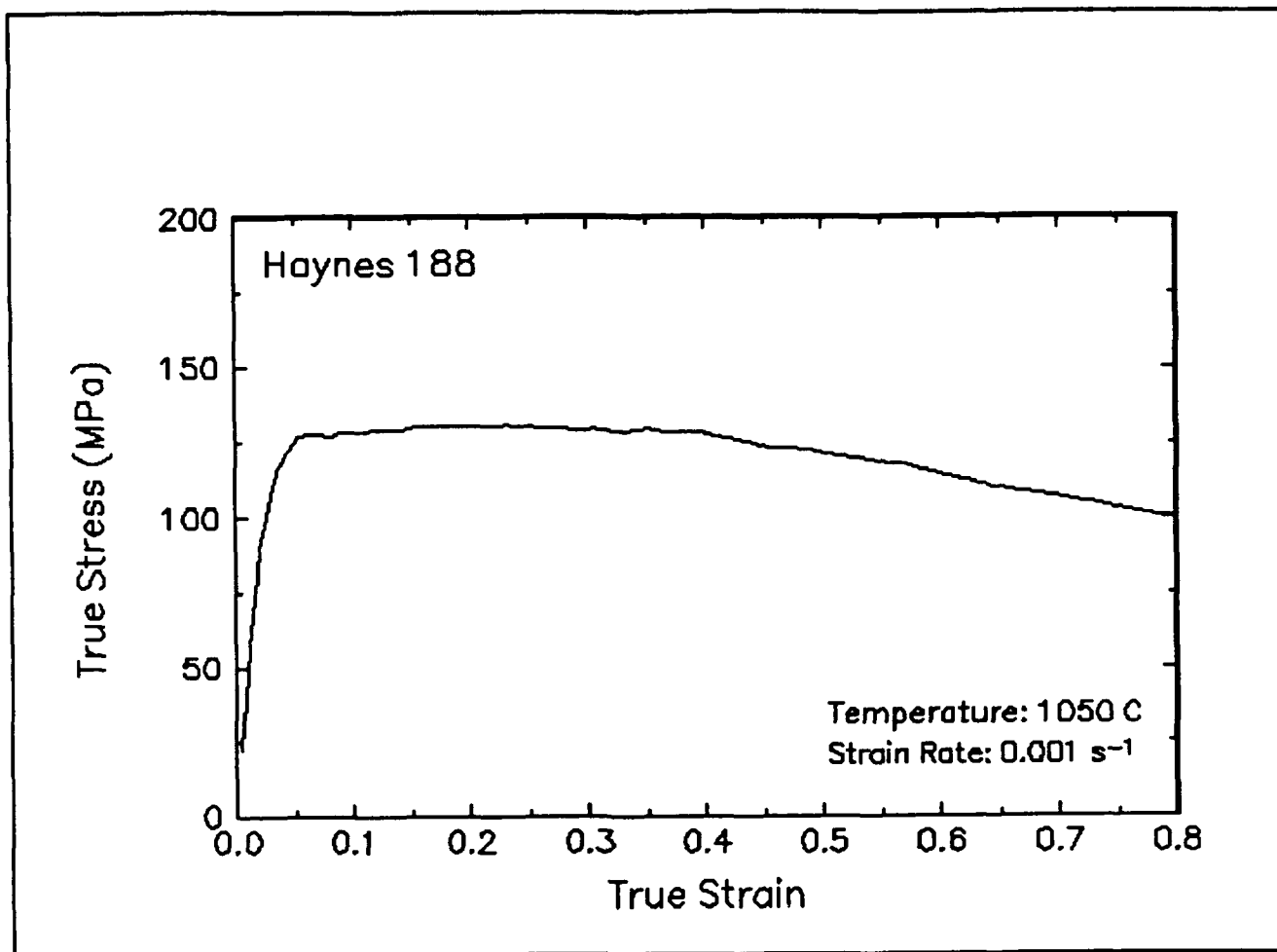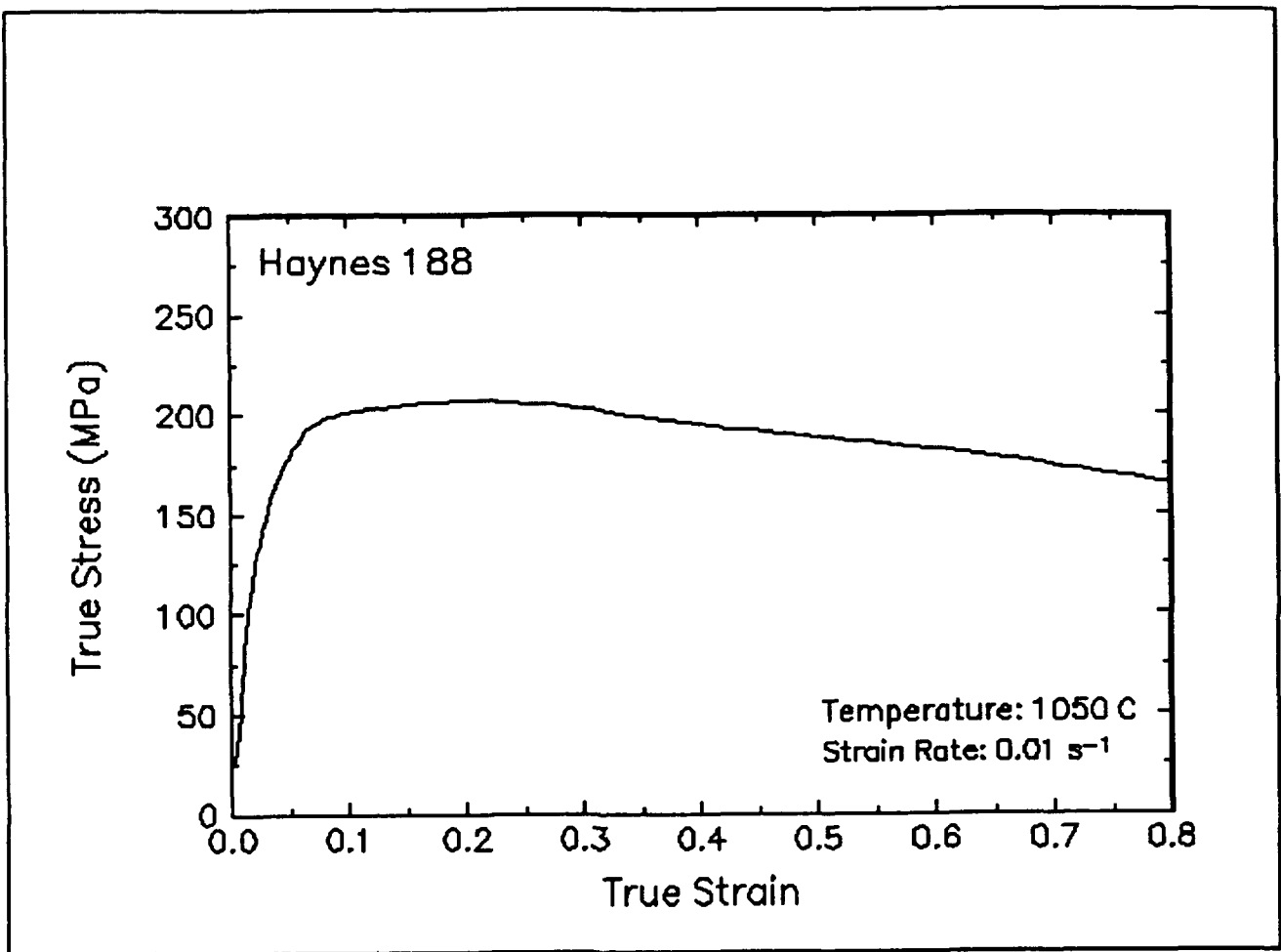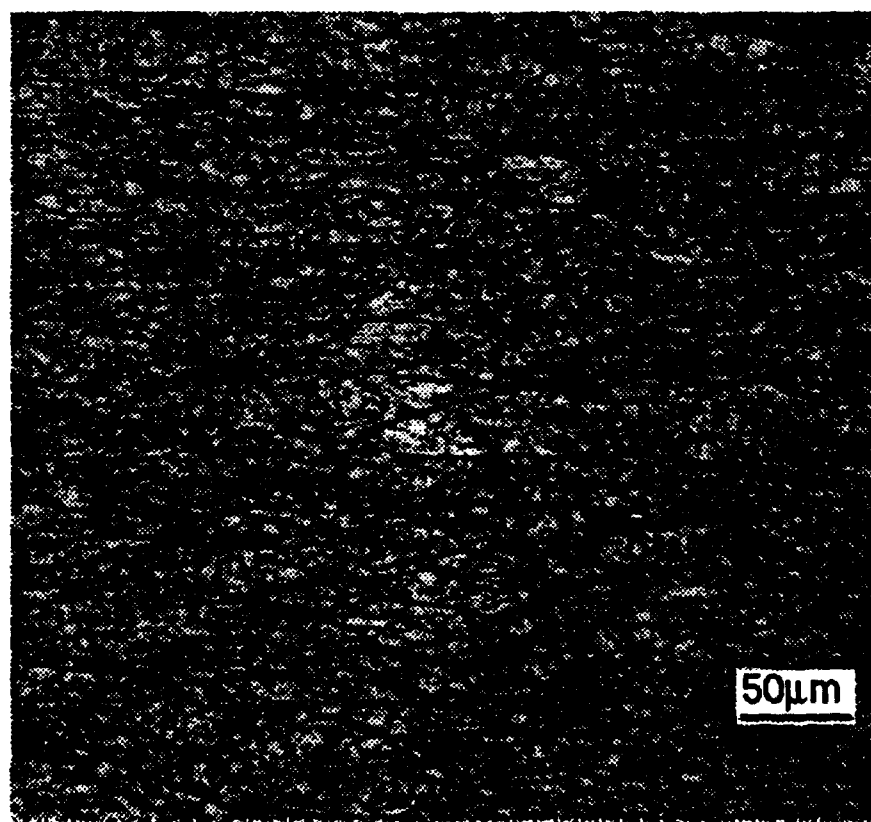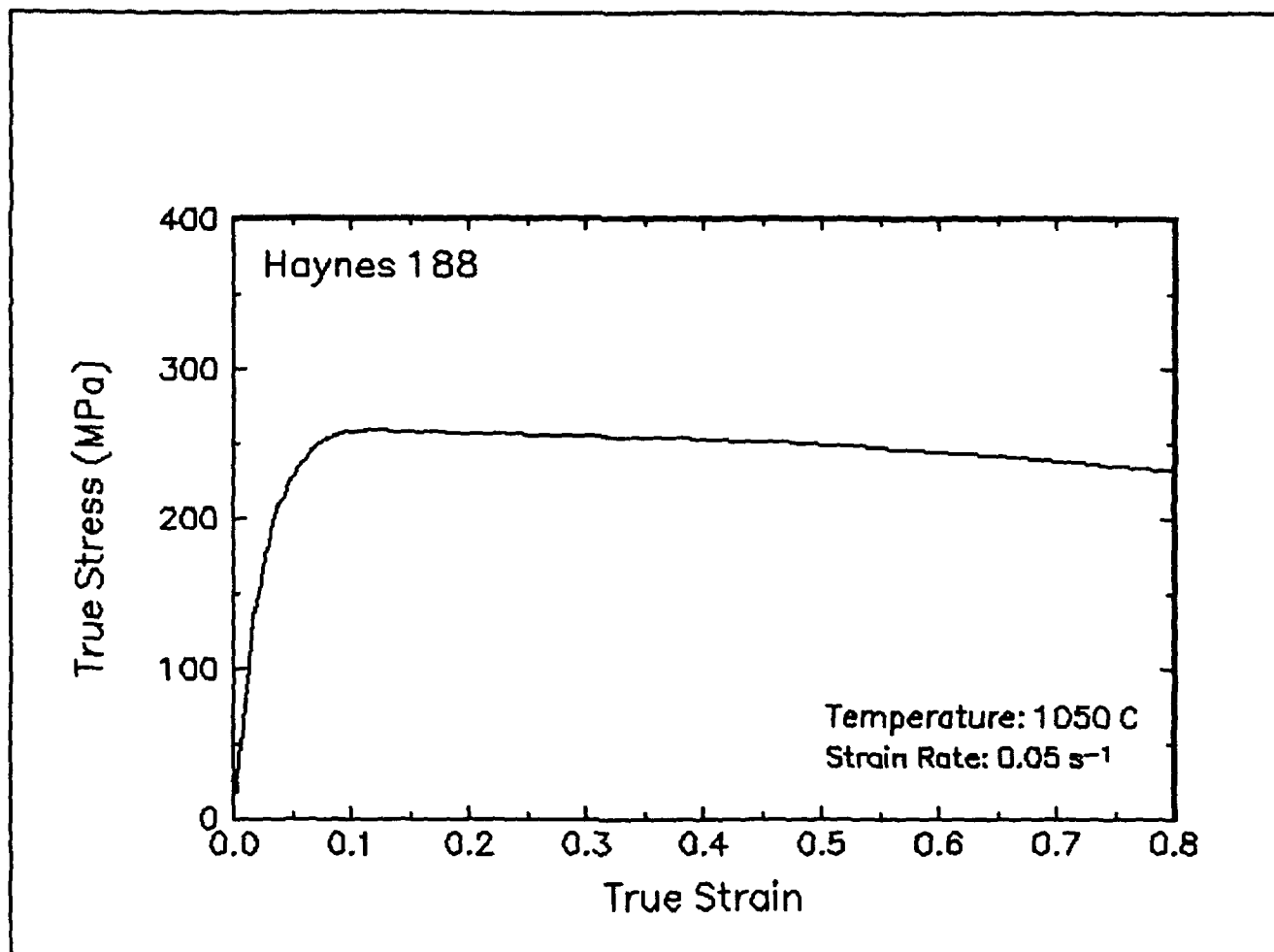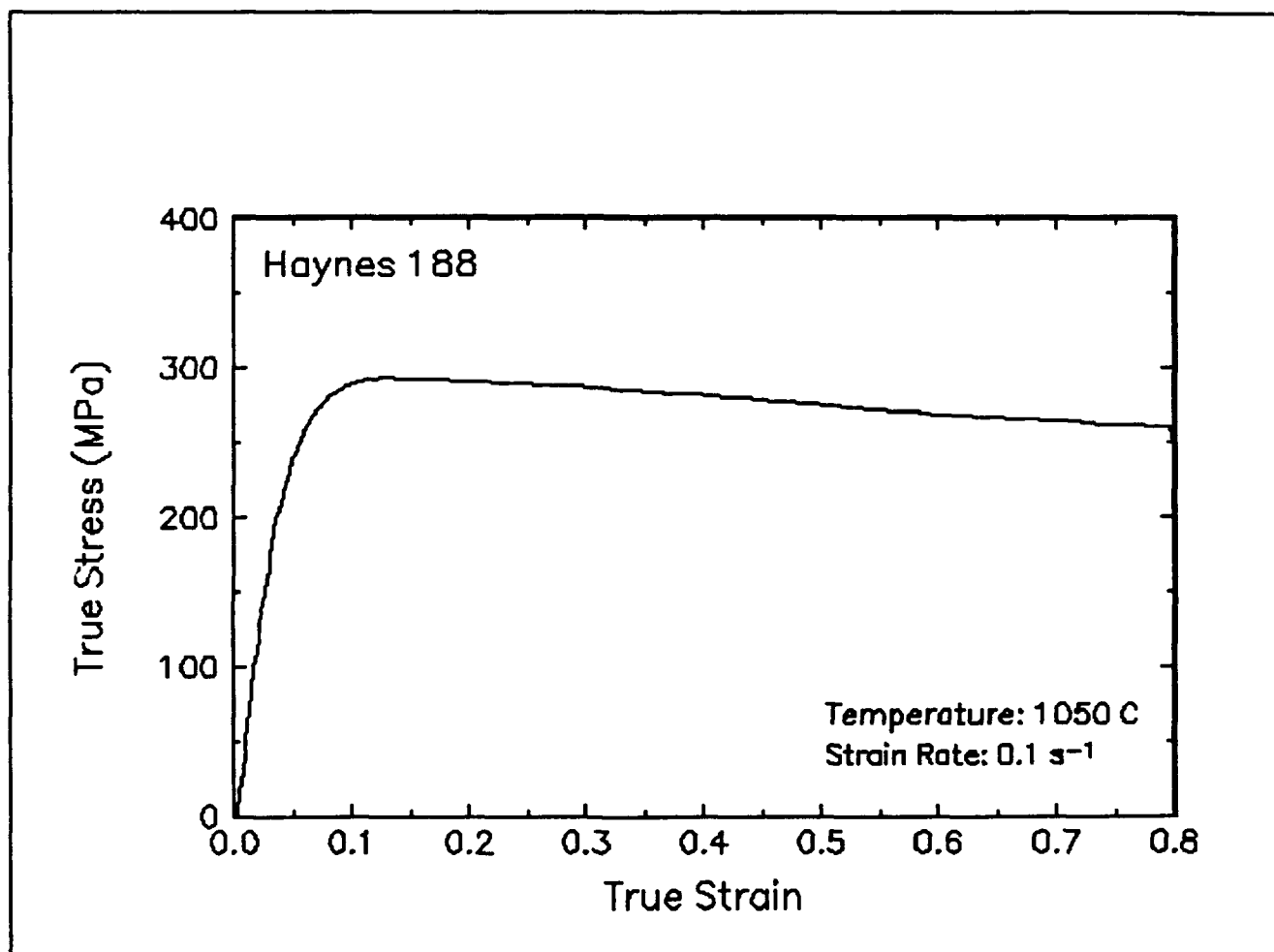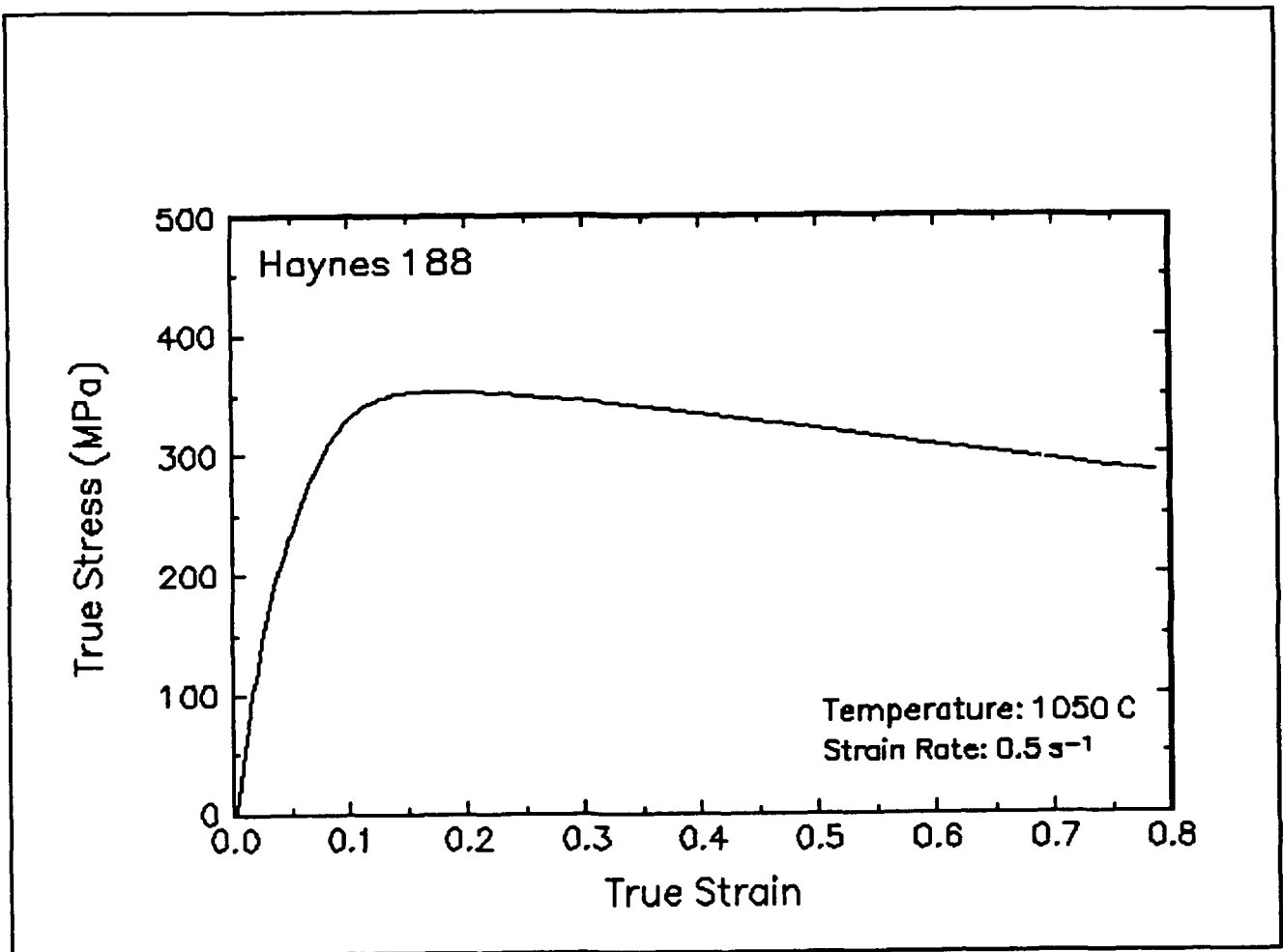
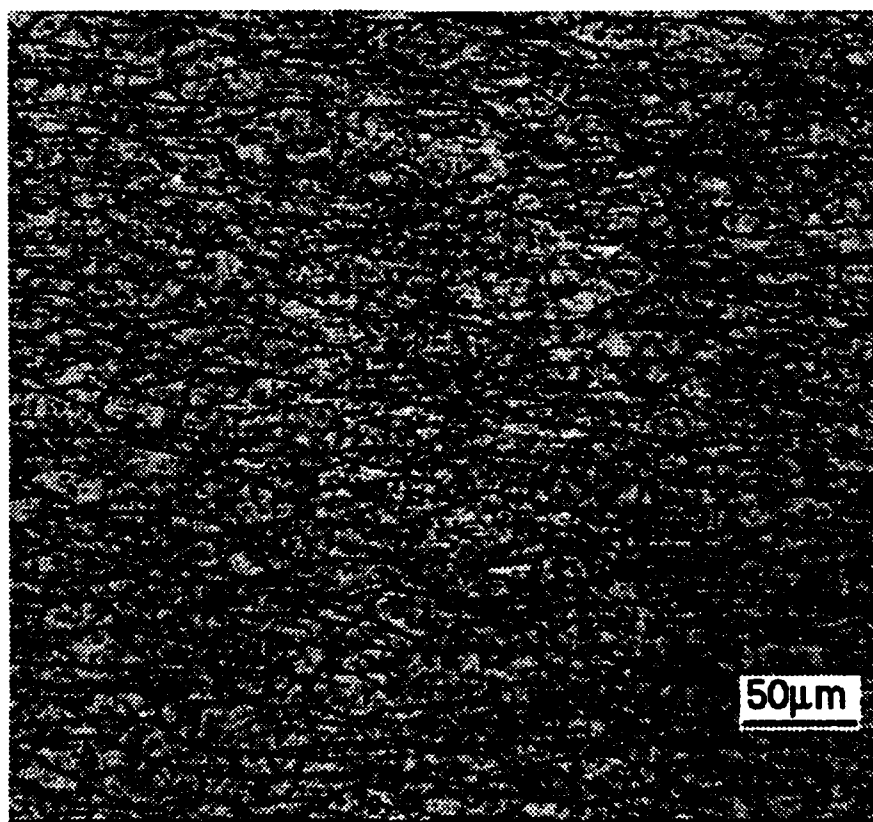Figure 3. True stress-true strain curve, 950 C and 0.01 s^{-1}.
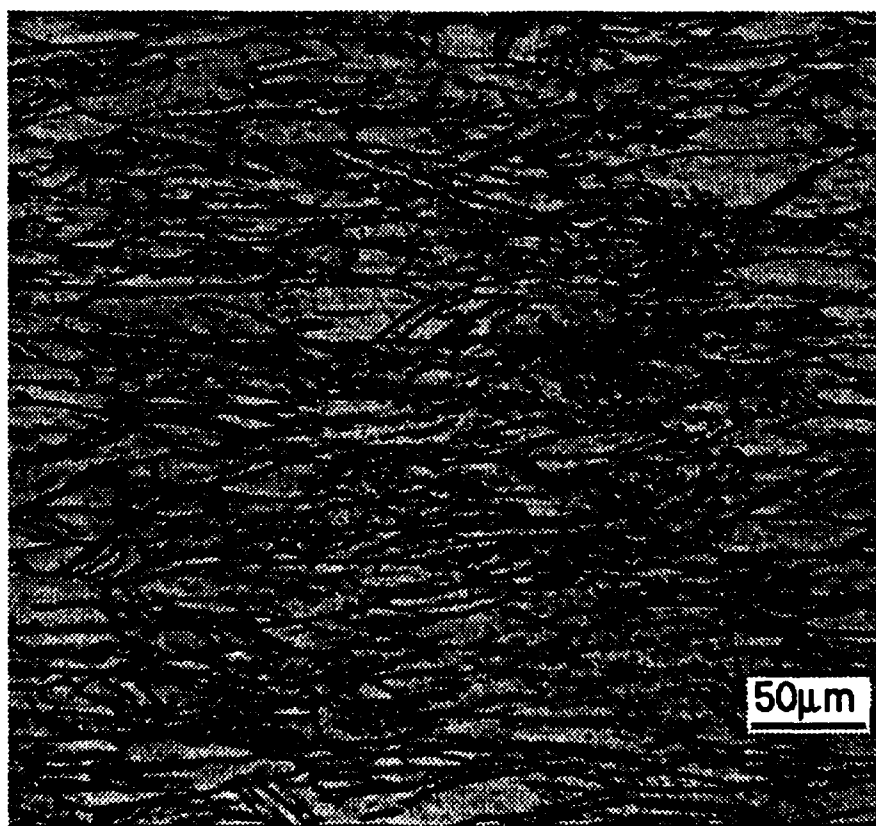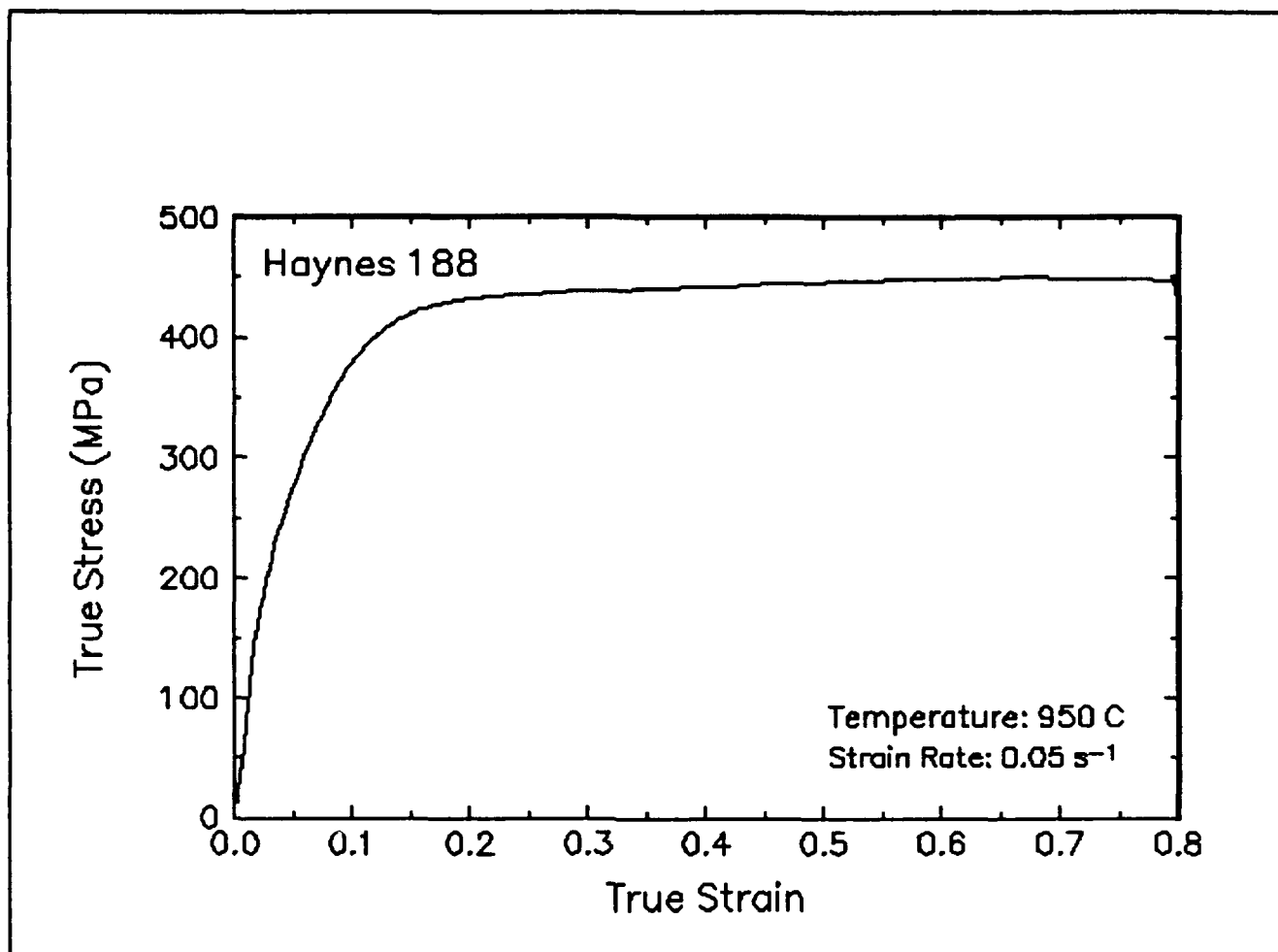
Figure 4. True stress-true strain curve and an optical micrograph from the center of the compressed sample cut through the compression axis, 950 C and 0.05 s^{-1}.
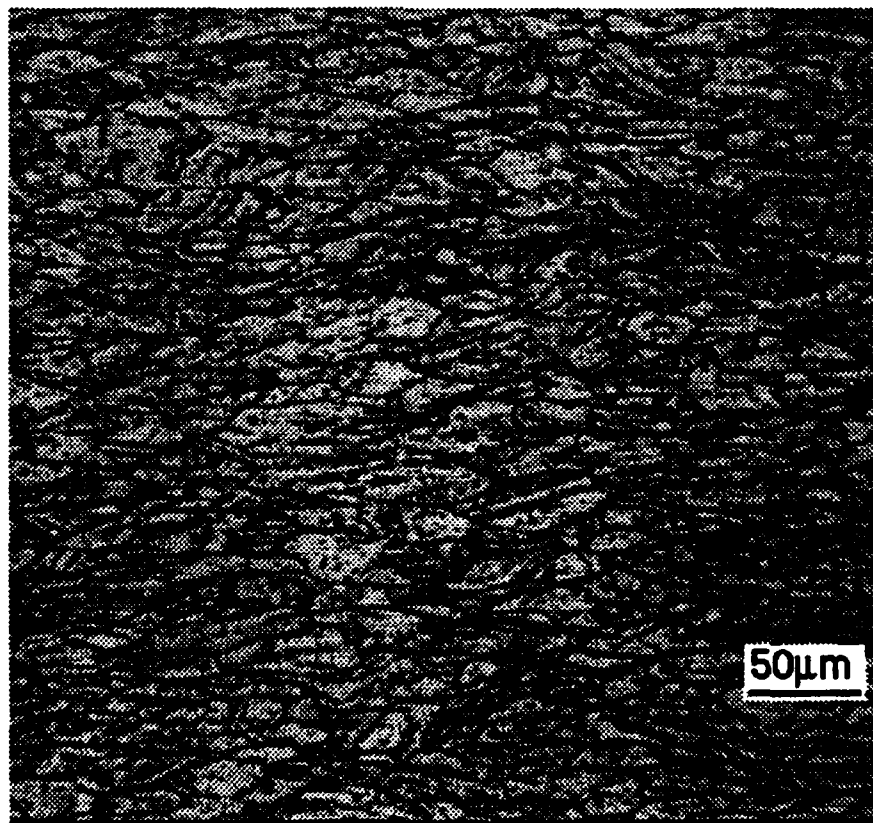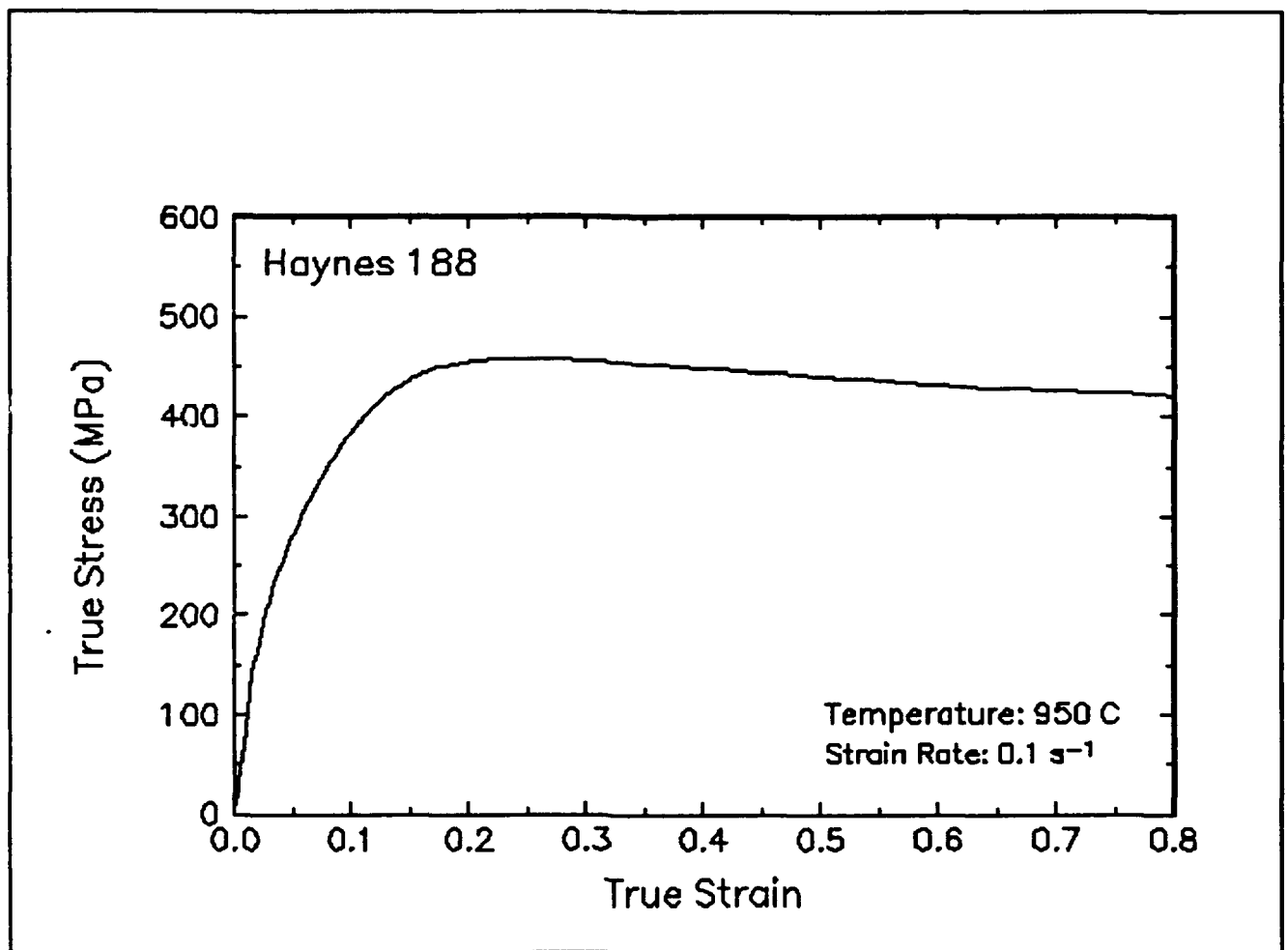
Figure 5. True stress-true strain curve and an optical micrograph from the center of the compressed sample cut through the compression axis, 950 C and 0.1 s⁻¹.
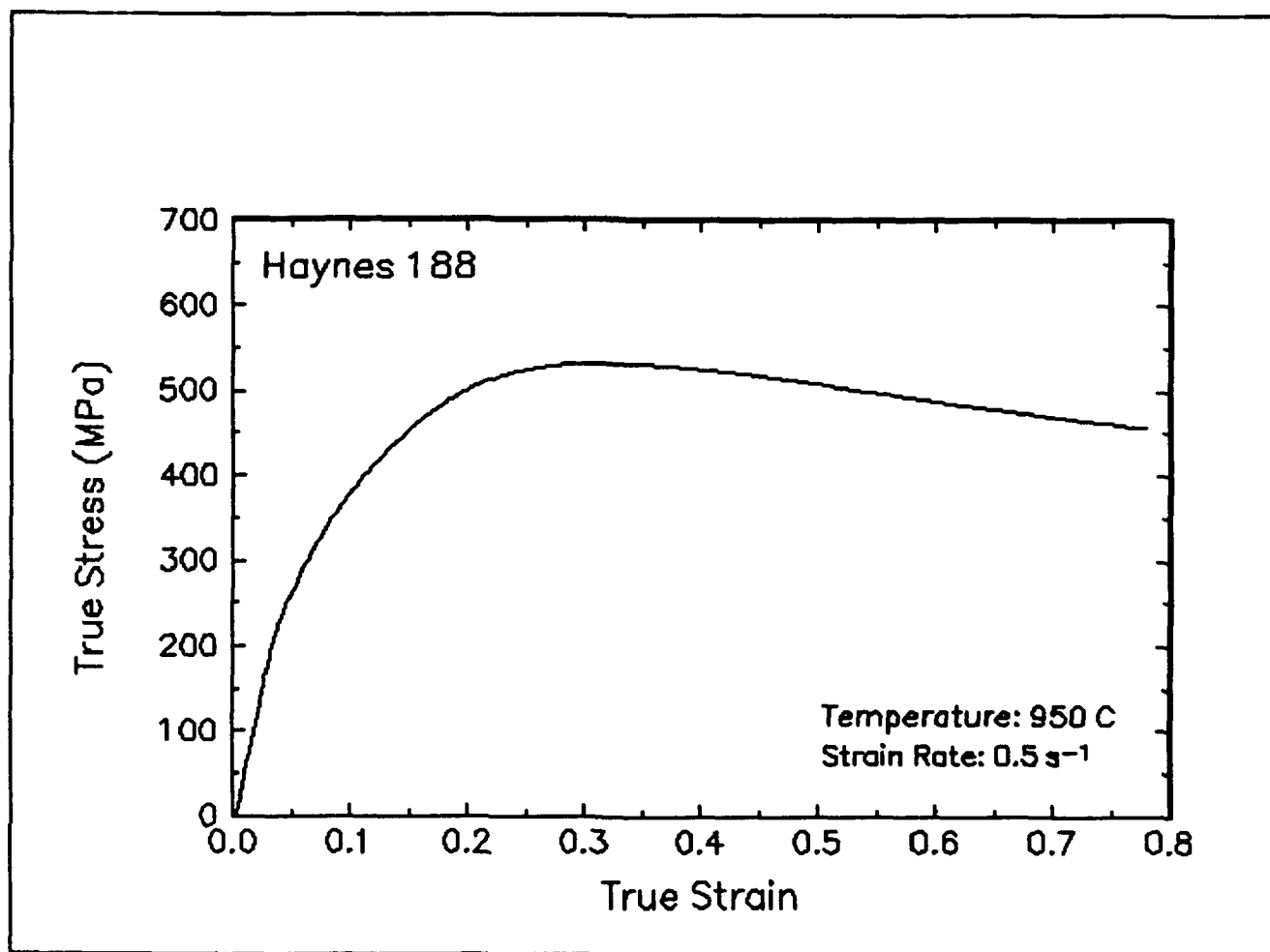
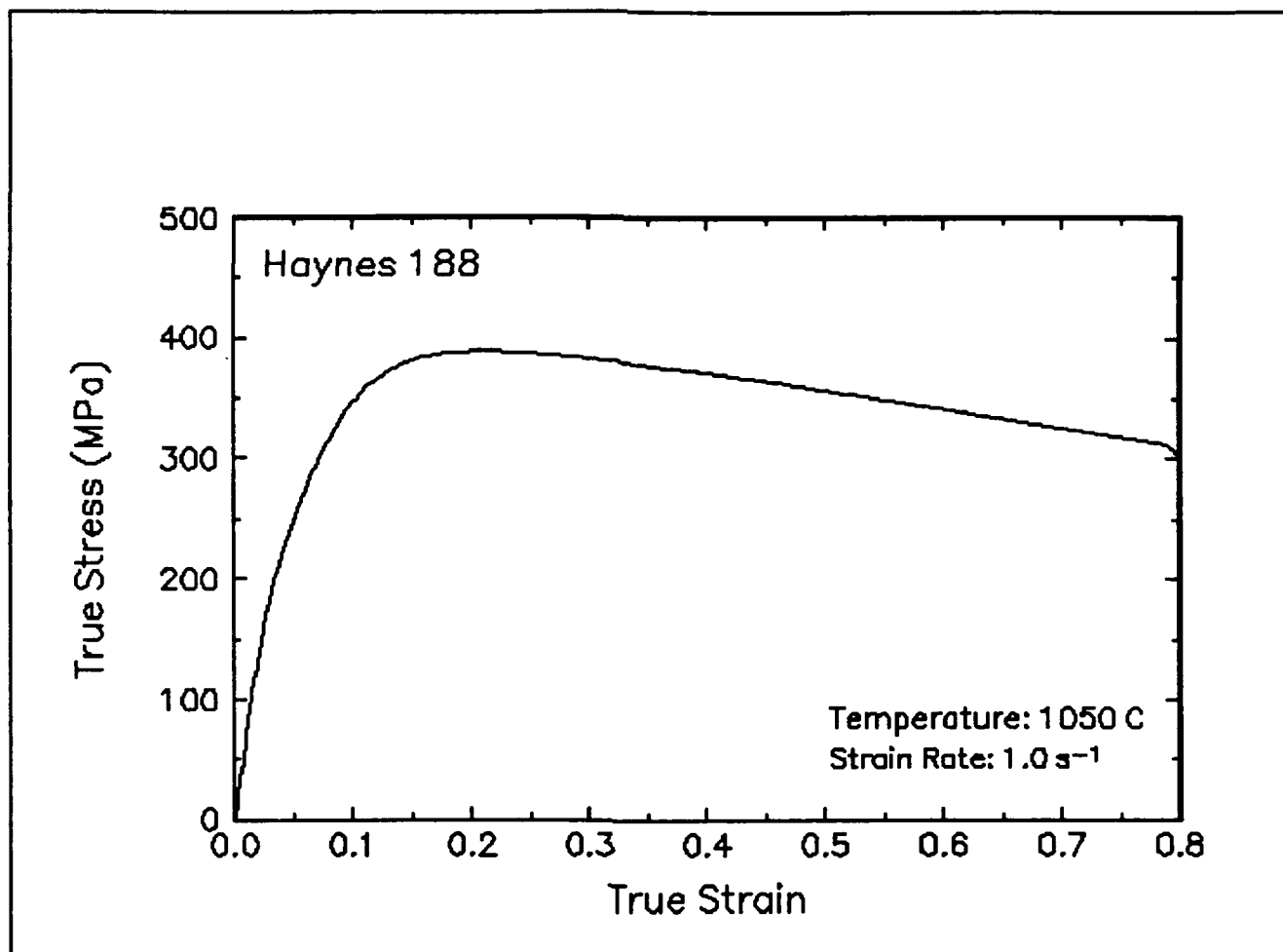Figure 6. True stress-true strain curve, 950 C and 0.5 s^{-1}.
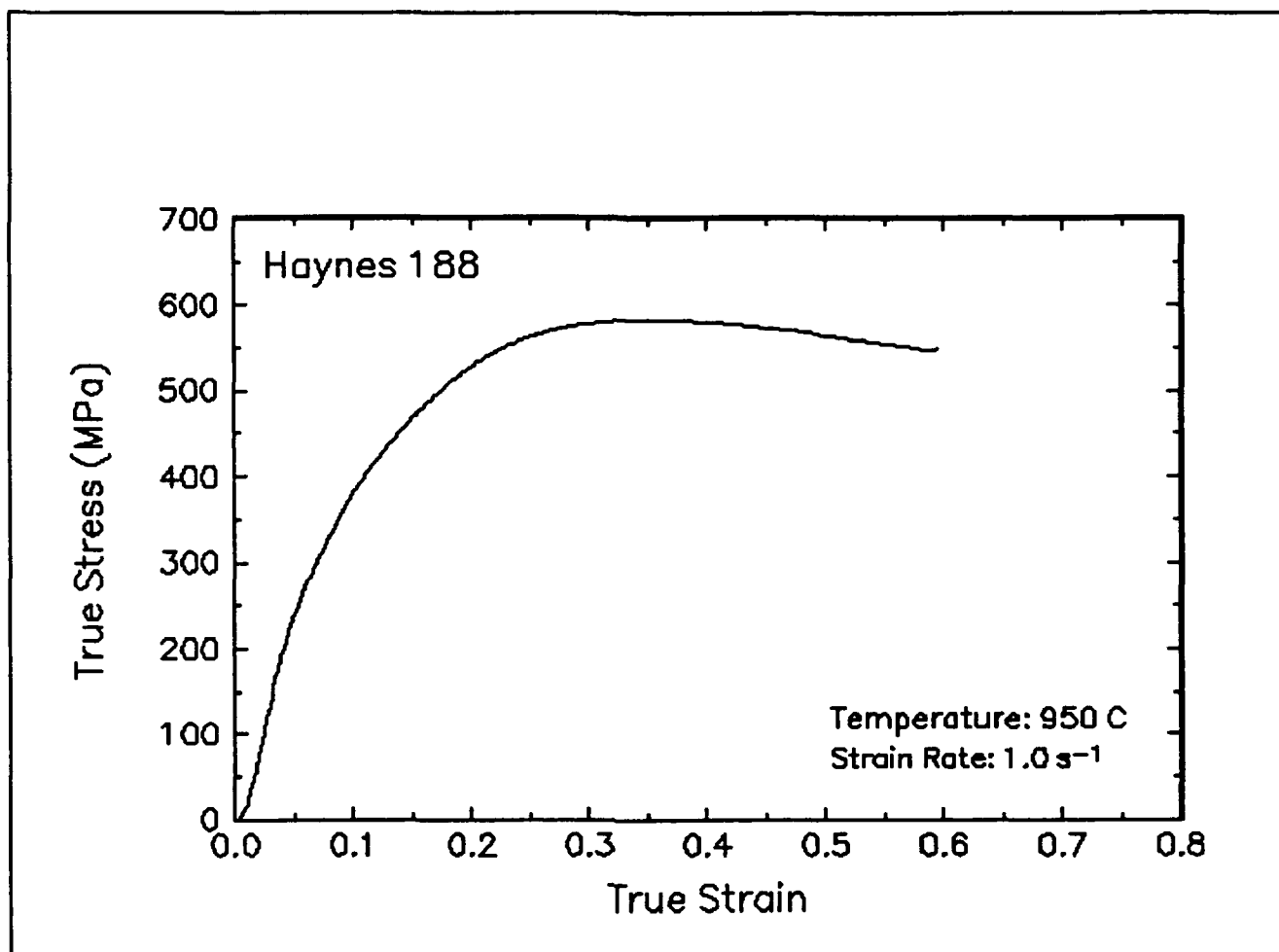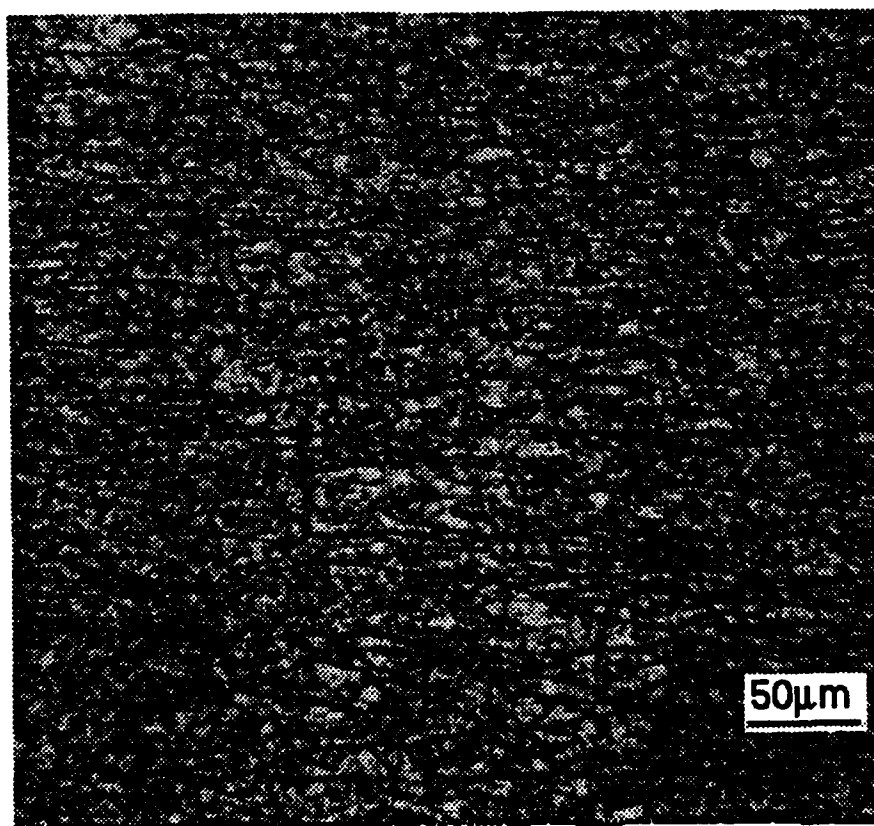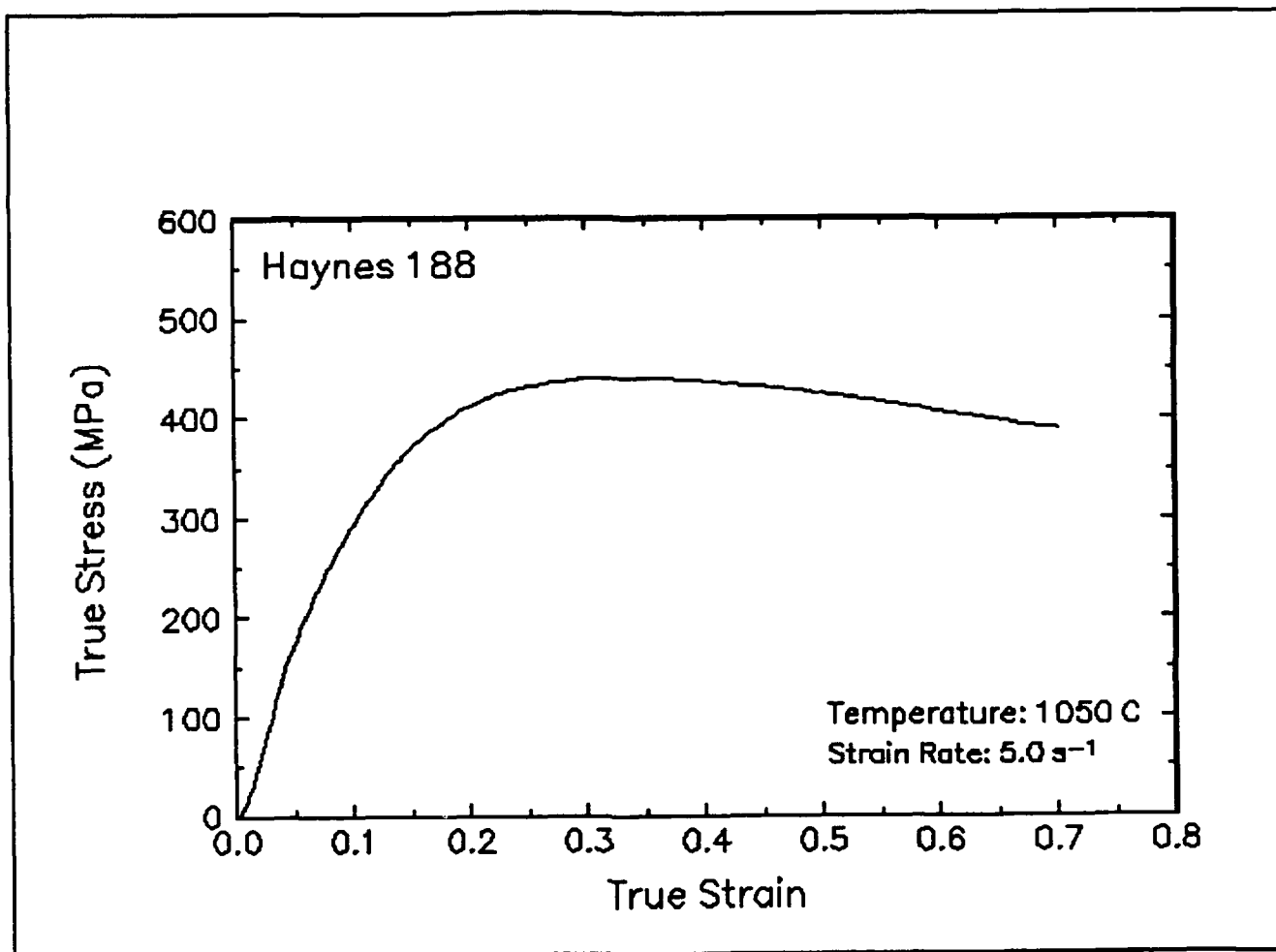
Figure 7. True stress-true strain curve and an optical micrograph from the center of the compressed sample cut through the compression axis, 950 C and 1 s^{-1}.
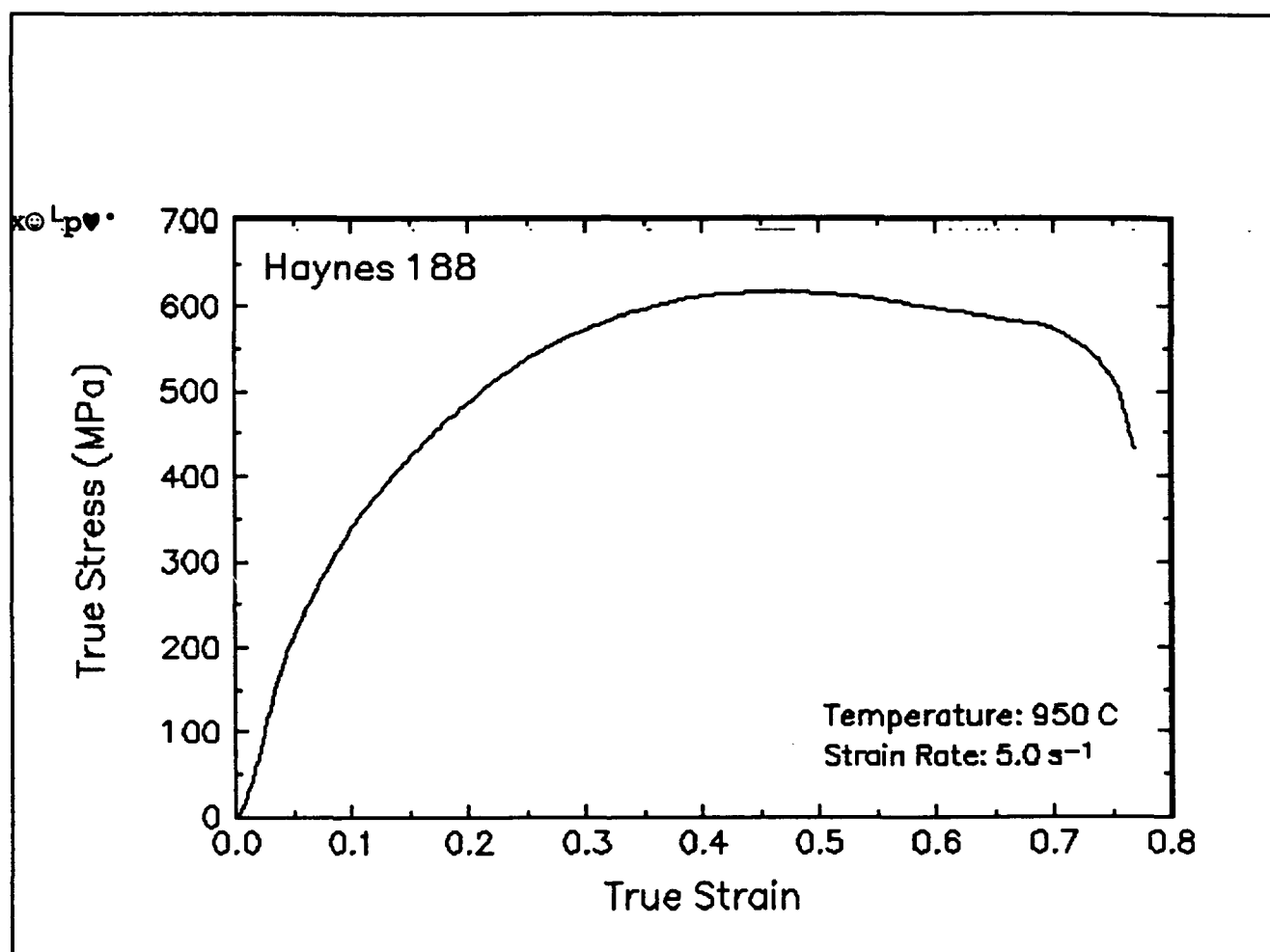
Figure 8. True stress-true strain curve, 950 C and 5 s^{-1}.
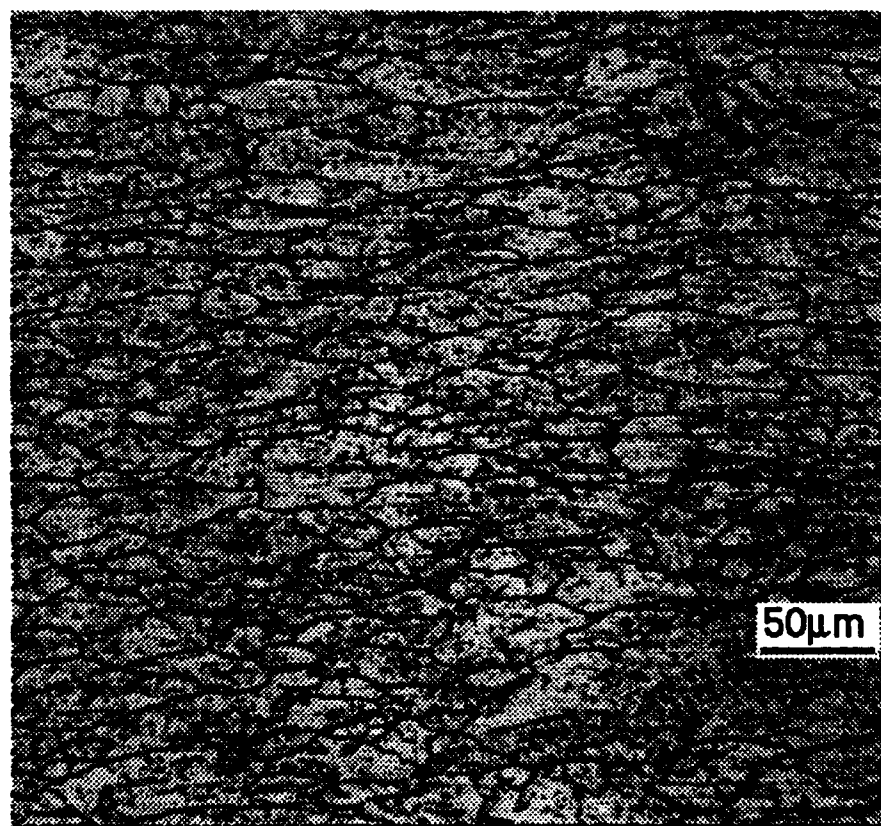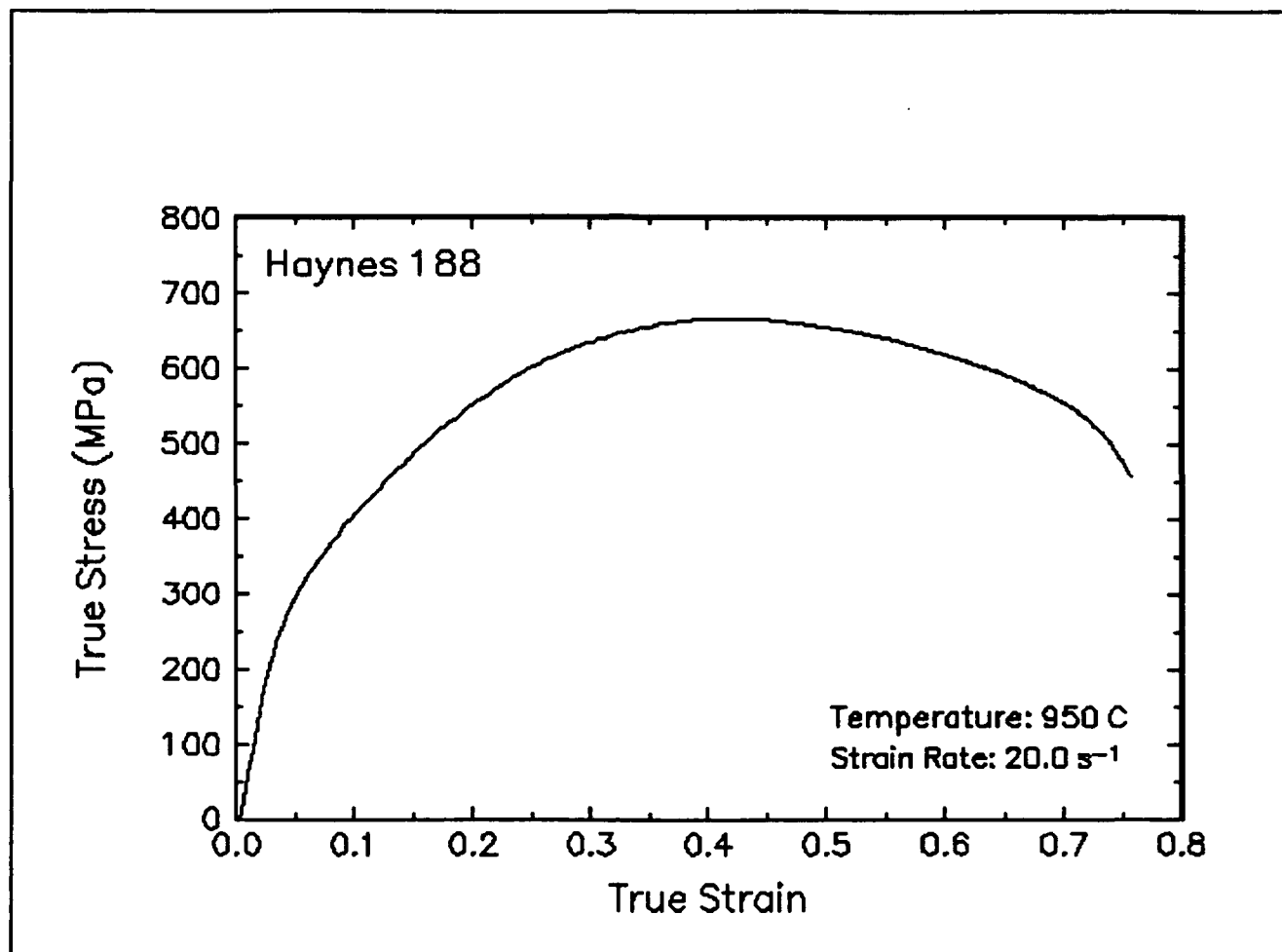
Figure 9. True stress-true strain curve and an optical micrograph from the center of the compressed sample cut through the compression axis, 950 C and 20 s^{-1}.
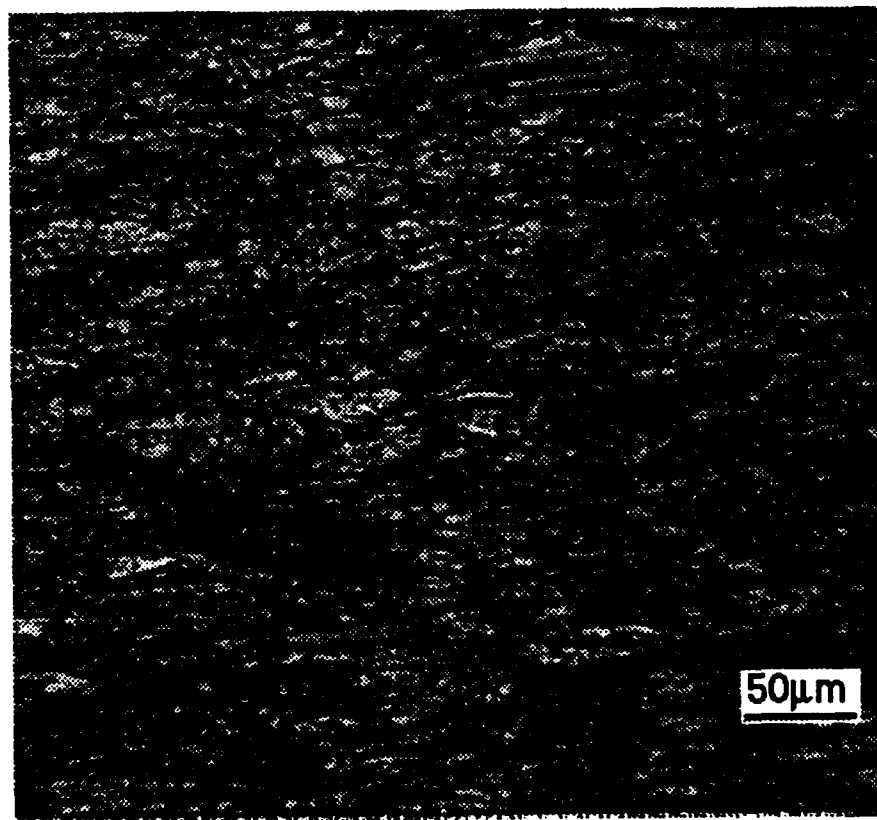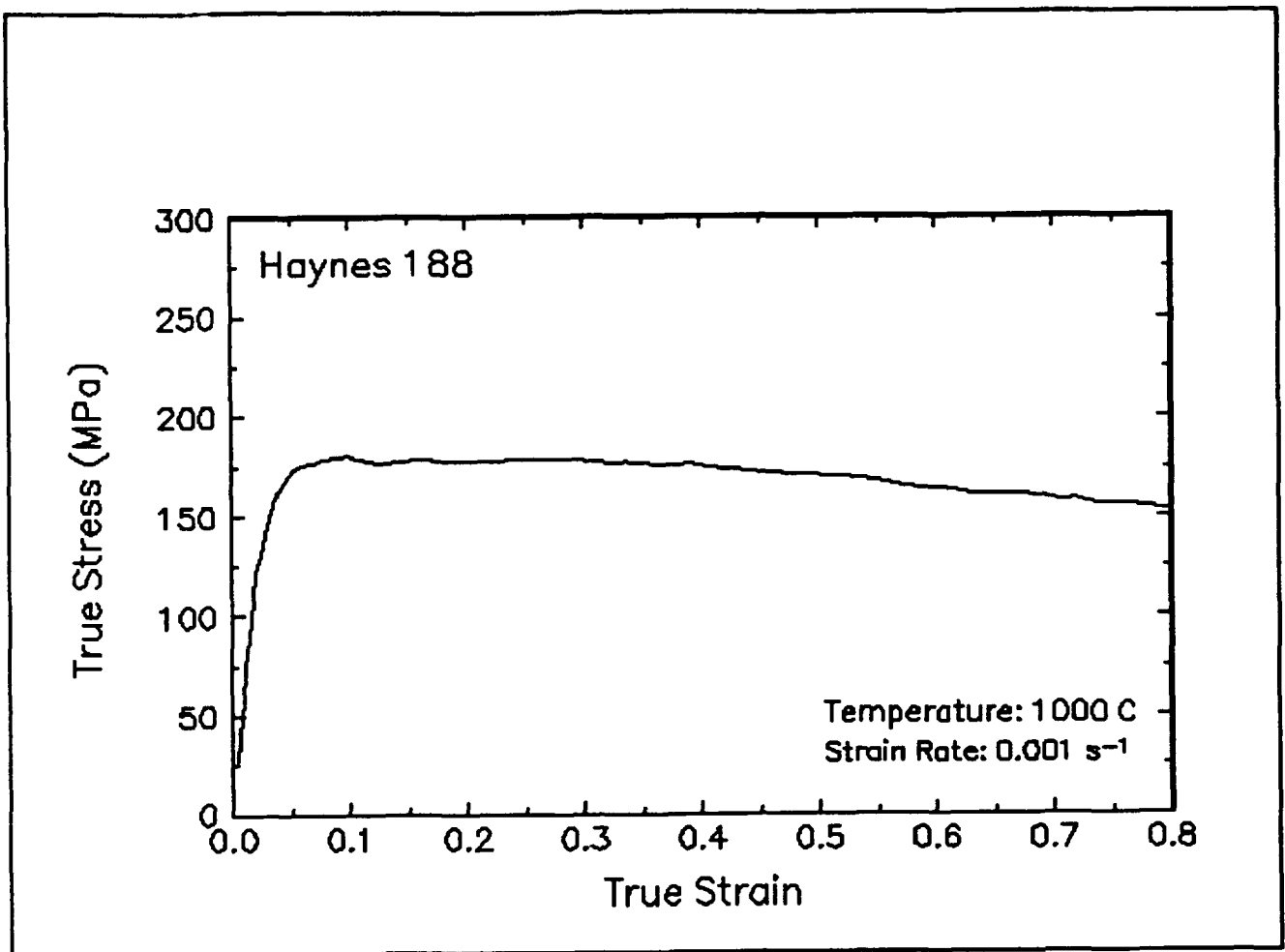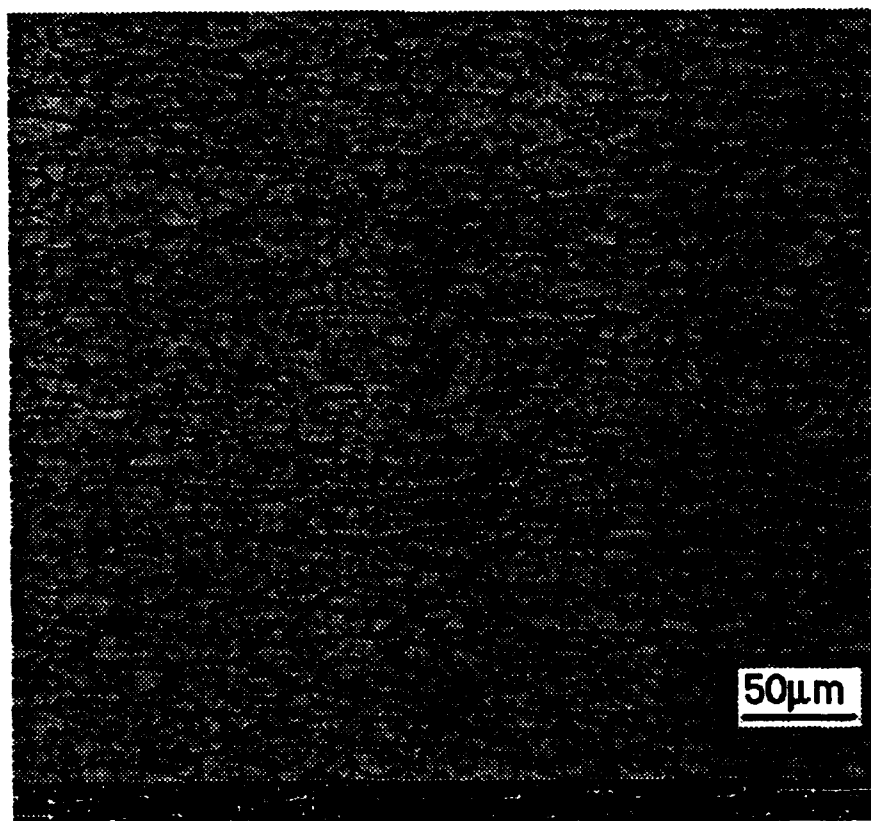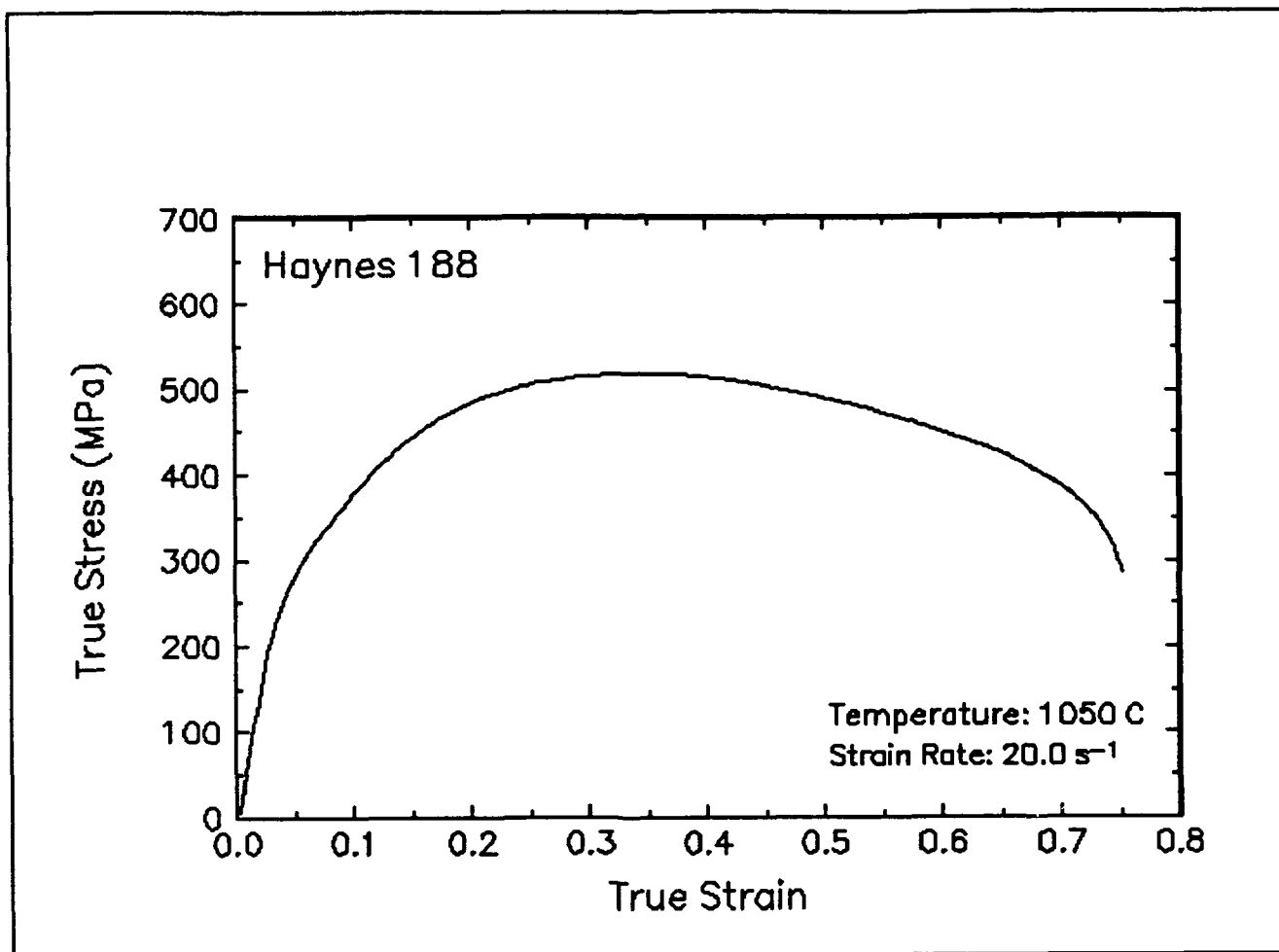
Figure 10. True stress-true strain curve and an optical micrograph from the center of the compressed sample cut through the compression axis, 1000 C and 0.001 s^{-1}.
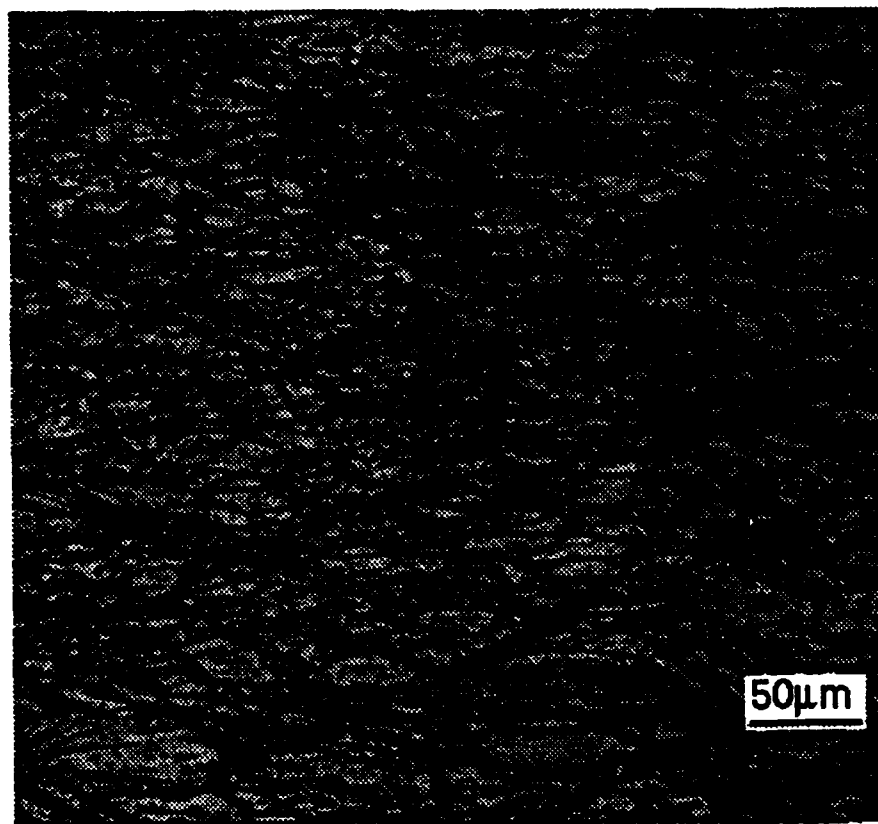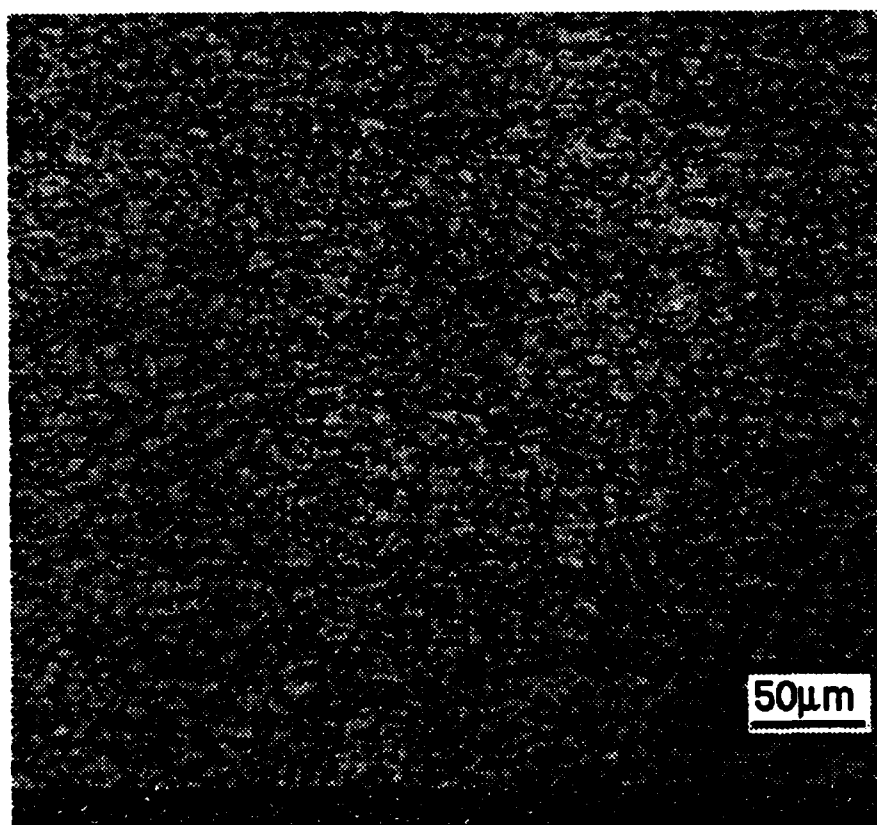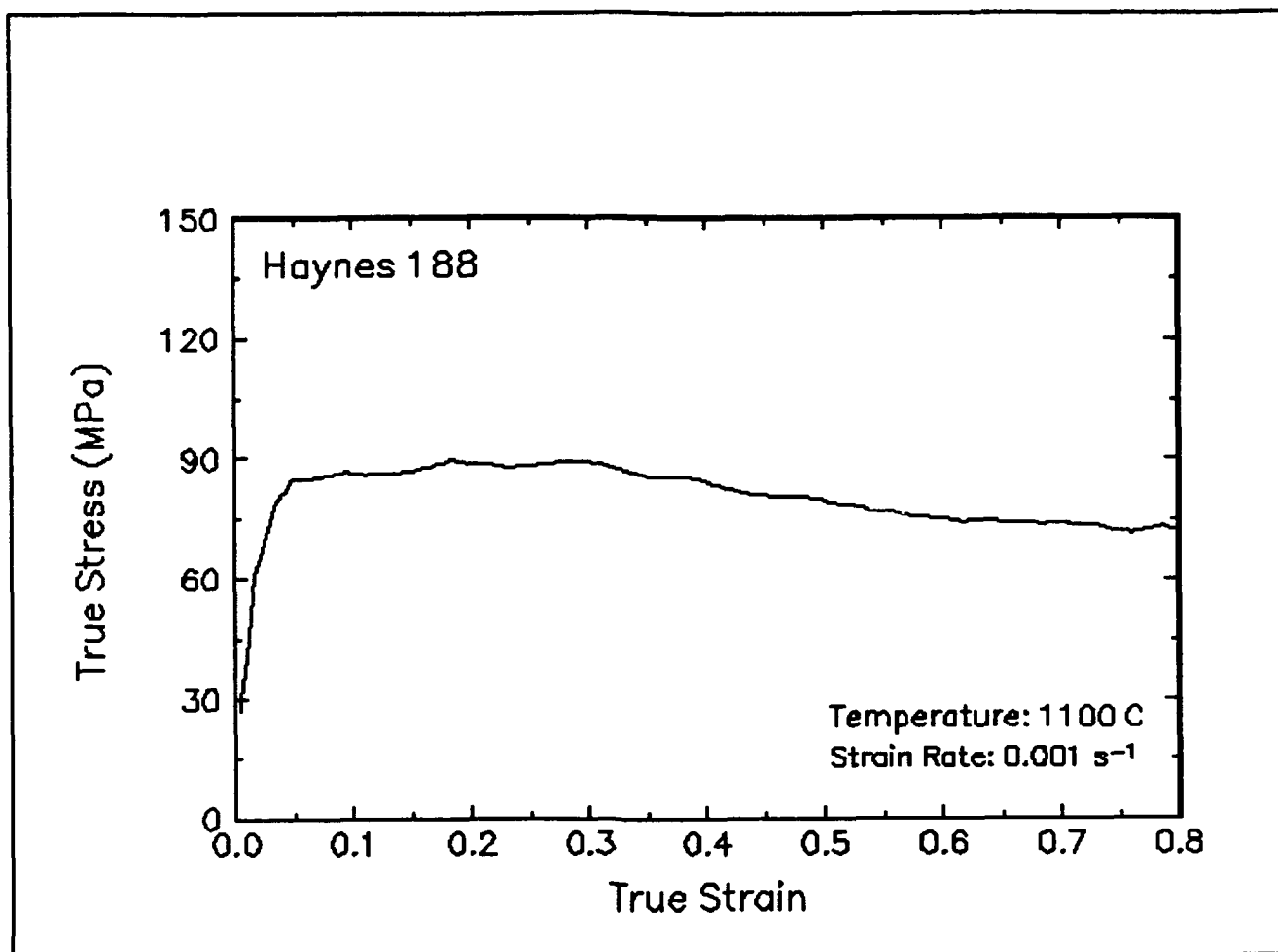
Figure 11. True stress-true strain curve and an optical micrograph from the center of the compressed sample cut through the compression axis, 1000 C and 0.01 s^{-1}.

14

Figure 12. True stress-true strain curve, 1000 C and 0.05 s^{-1}.

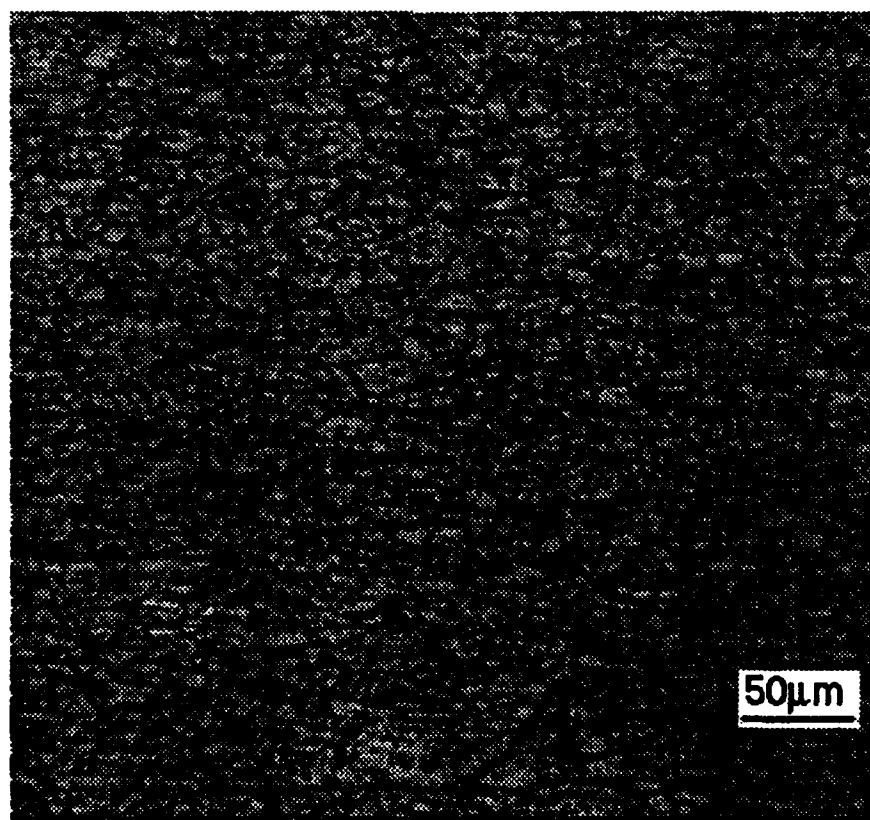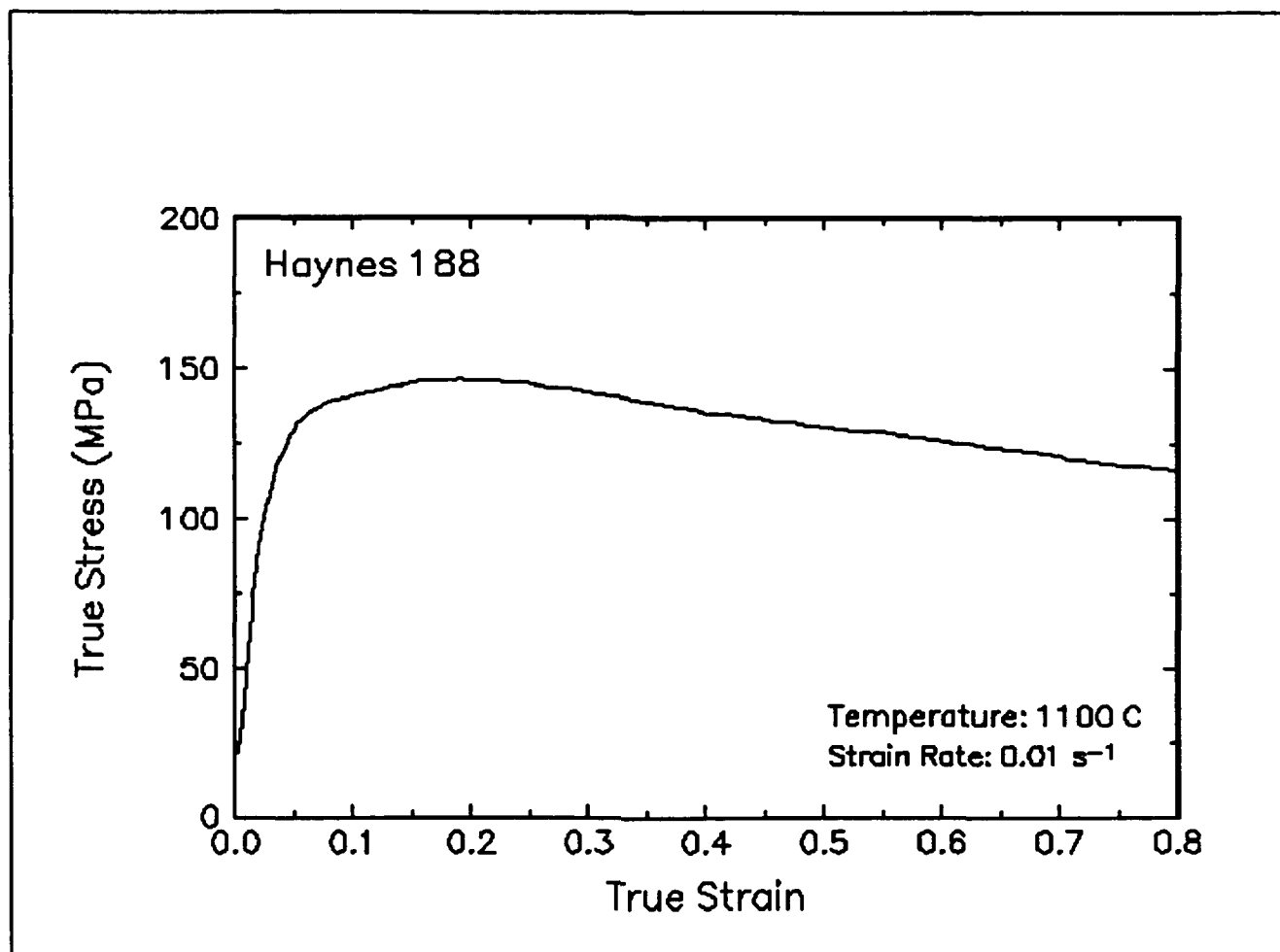Figure 13. True stress-true strain curve, 1000 C and 0.1 s^{-1}.

Figure 14. True stress-true strain curve and an optical micrograph from the center of the compressed sample cut through the compression axis, 1000 C and 0.5 s^{-1}.

17

Figure 15. True stress-true strain curve and an optical micrograph from the center of the compressed sample cut through the compression axis, 1000 C and 1 s^{-1}.

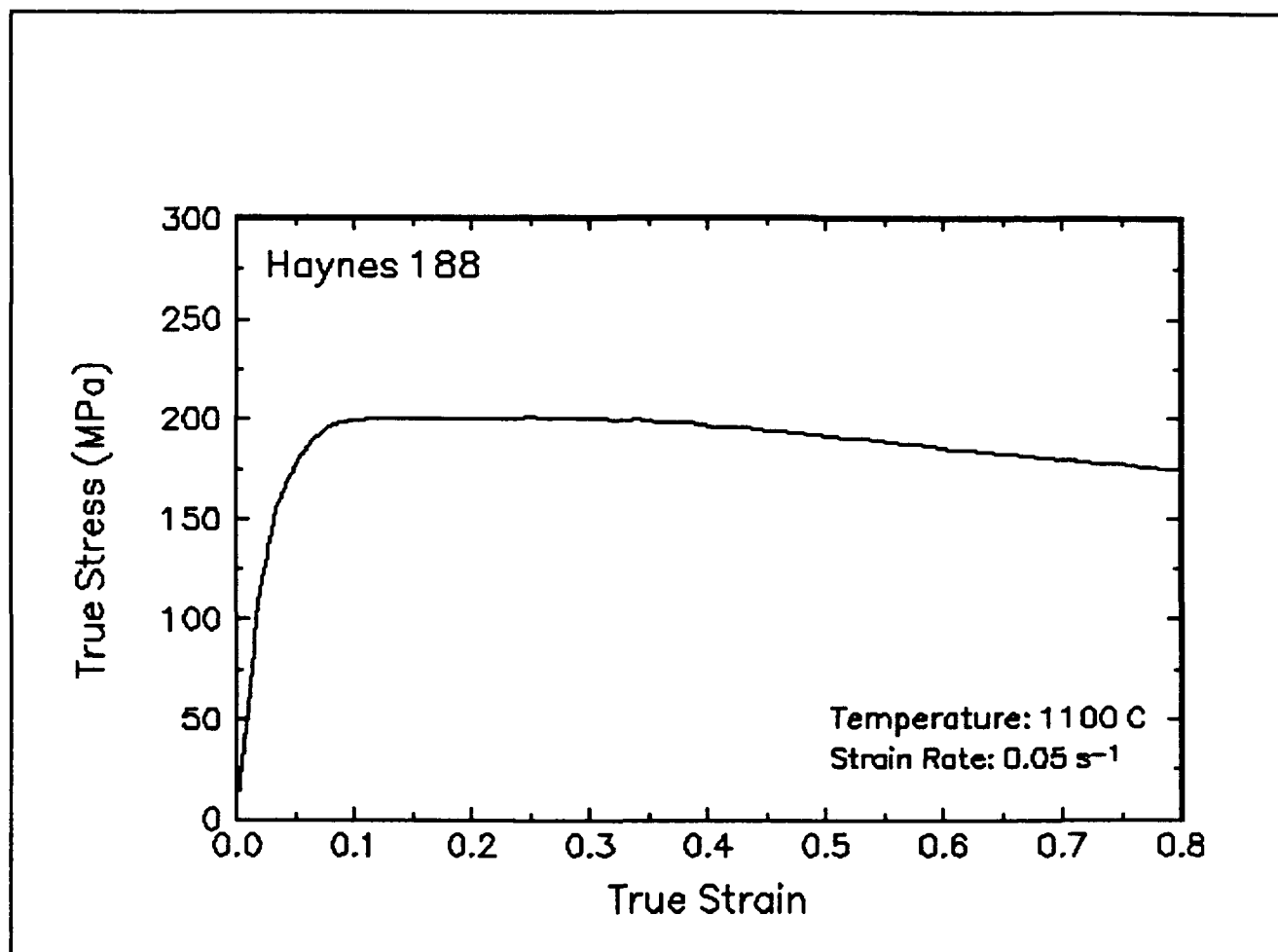18

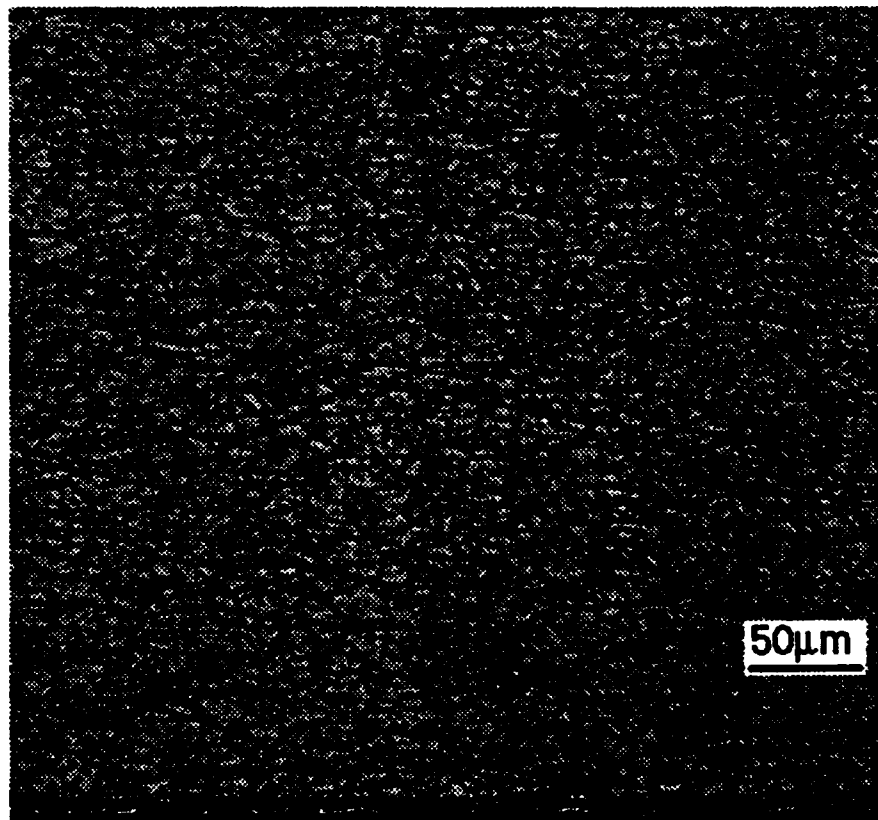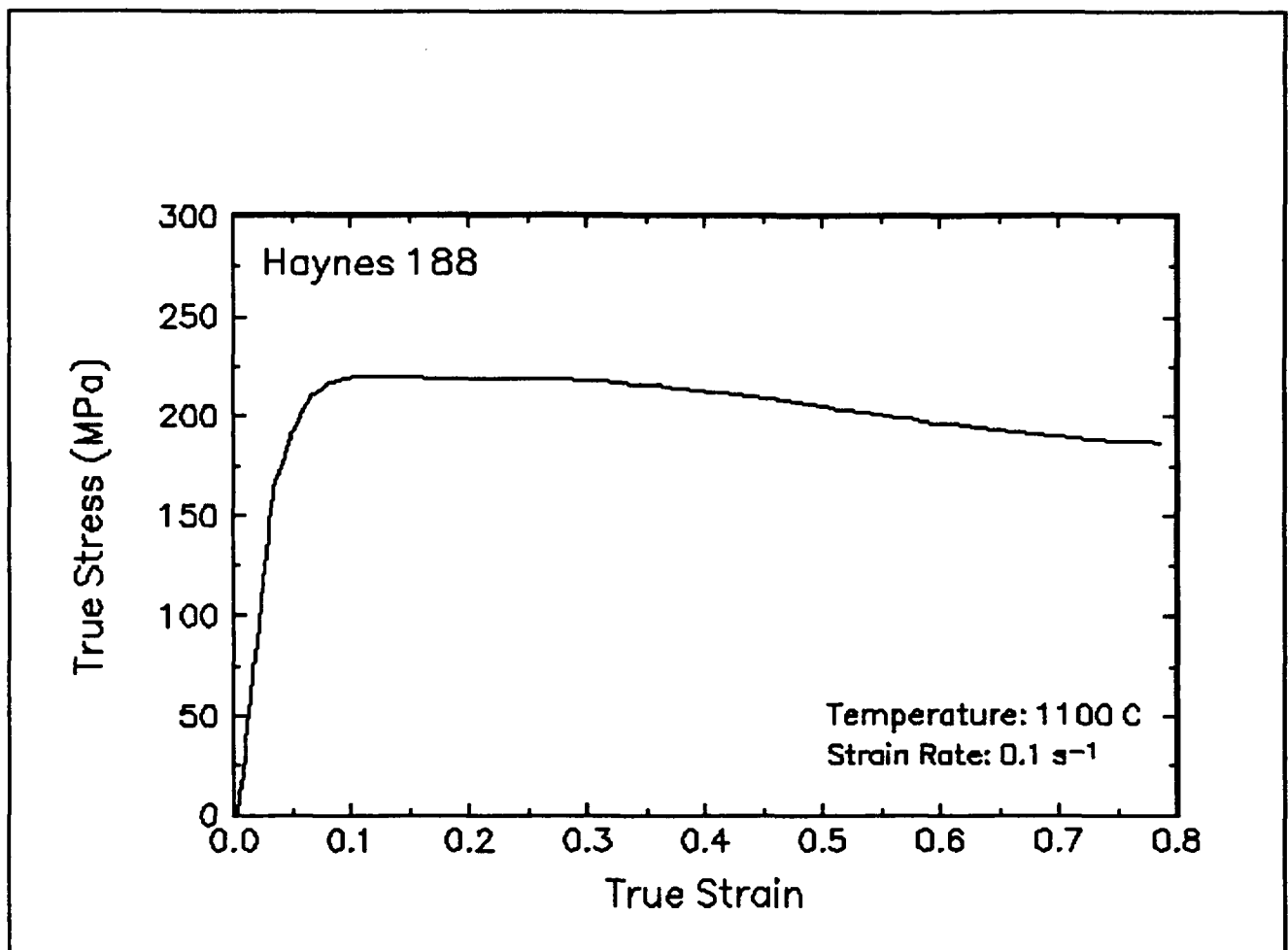Figure 16. True stress-true strain curve, 1000 C and 5 s^{-1}.

Figure 17. True stress-true strain curve and an optical micrograph from the center of the compressed sample cut through the compression axis, 1000 C and 20 s^{-1}.

Figure 18. True stress-true strain curve and an optical micrograph from the center of the compressed sample cut through the compression axis, 1050 C and 0.001 s^{-1}.

Figure 19. True stress-true strain curve, 1050 C and 0.01 s^{-1}.

Figure 20. True stress-true strain curve and an optical micrograph from the center of the compressed sample cut through the compression axis, 1050 C and 0.05 s^{-1}.
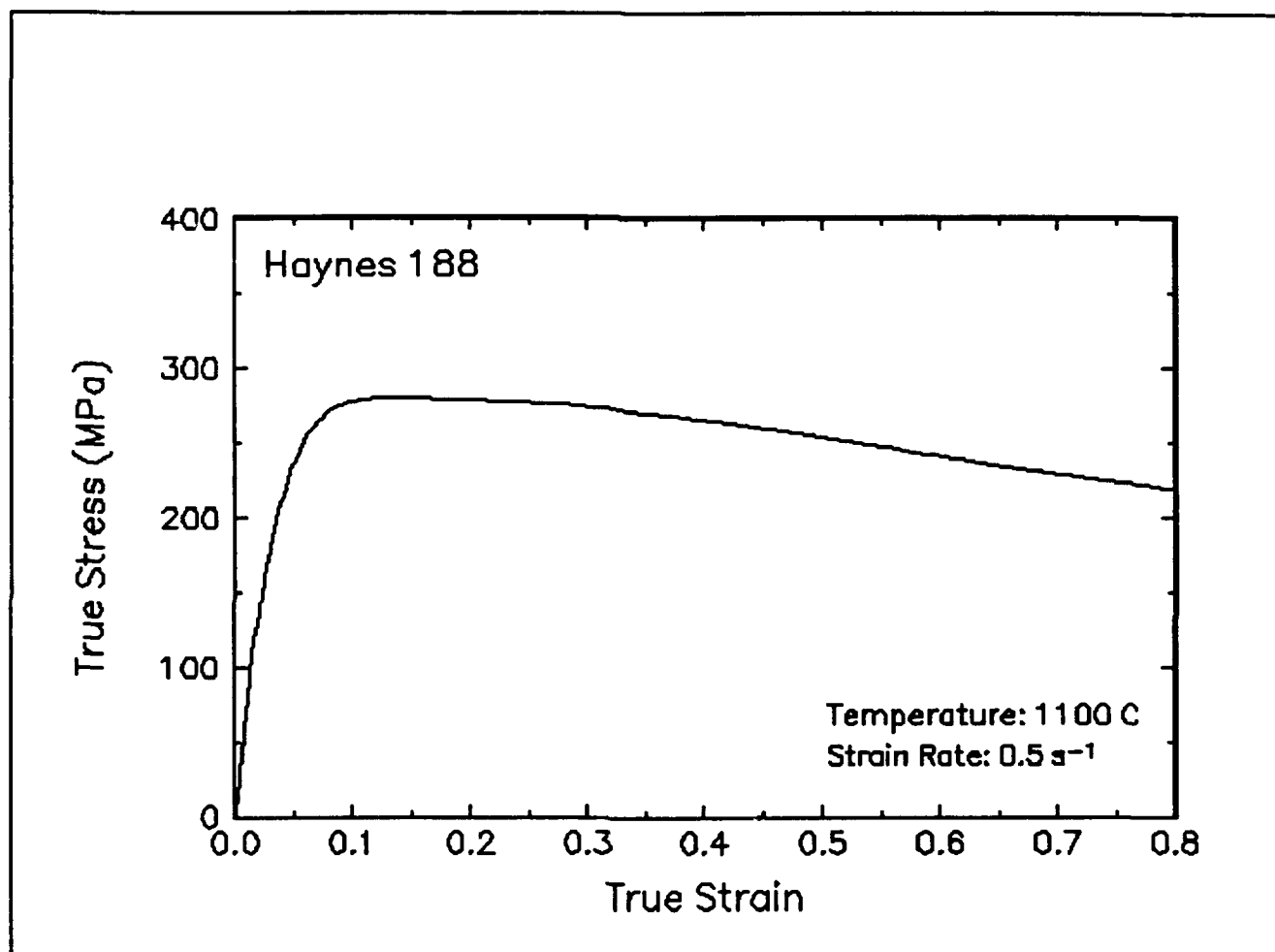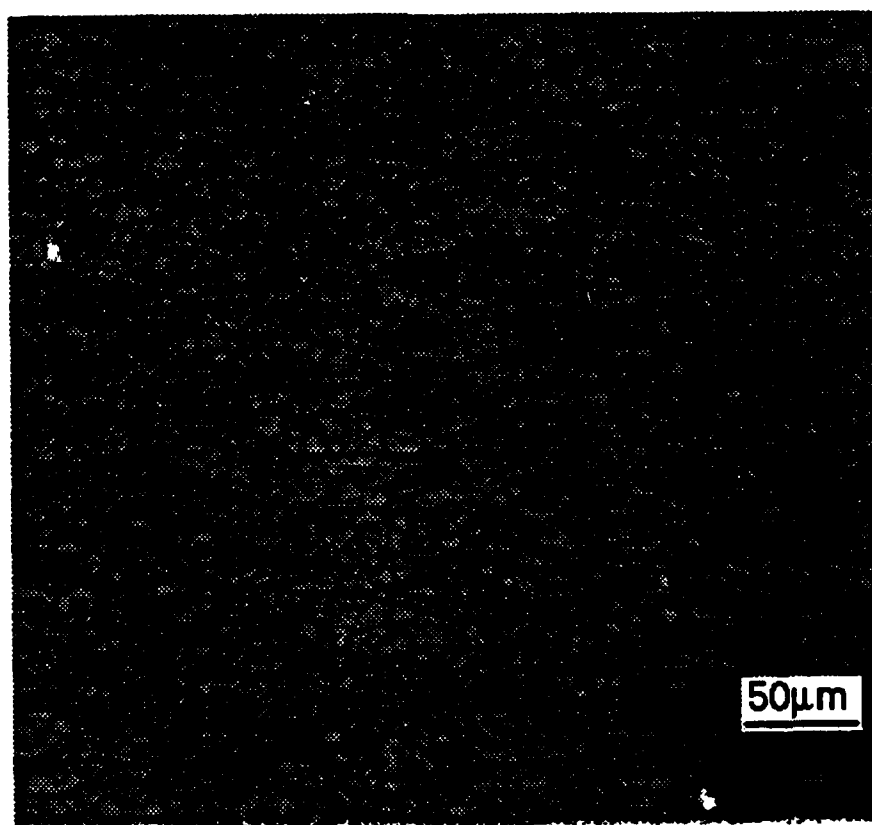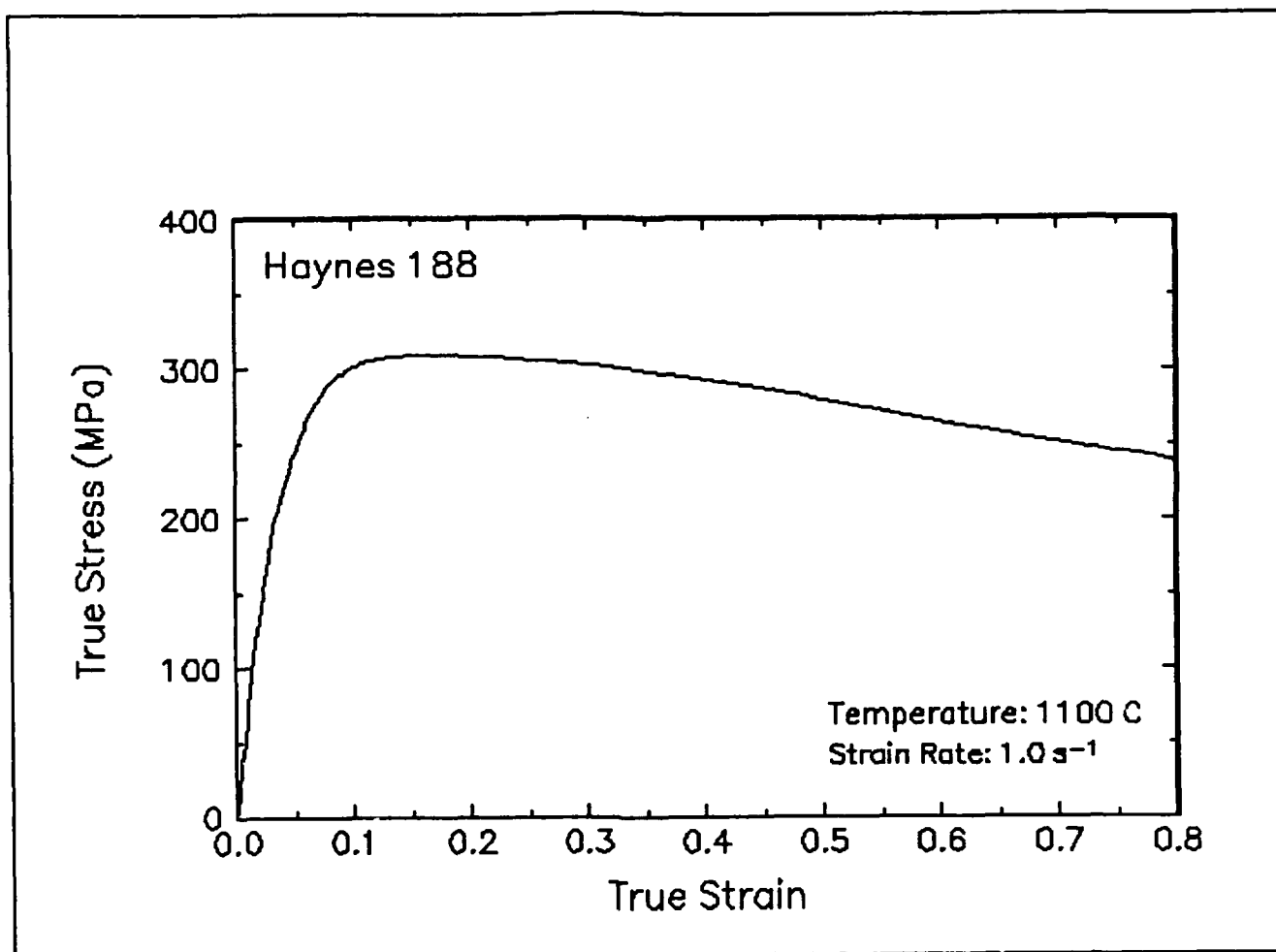
Figure 21. True stress-true strain curve, 1050 C and 0.1 s^{-1}.

Figure 22. True stress-true strain curve, 1050 C and 0.5 s^{-1}.

Figure 23. True stress-true strain curve and an optical micrograph from the center of the compressed sample cut through the compression axis, 1050 C and 1 s^{-1}.
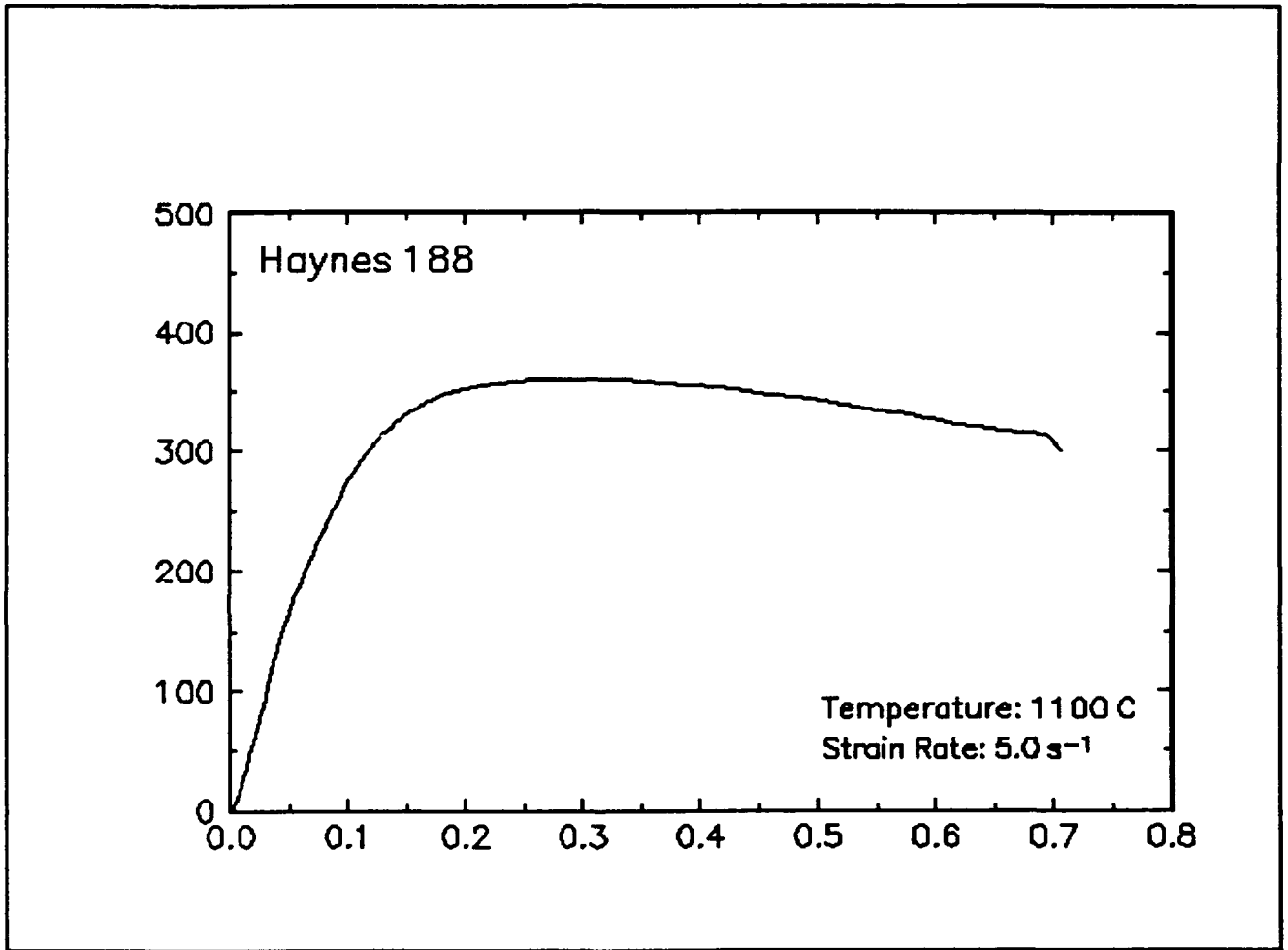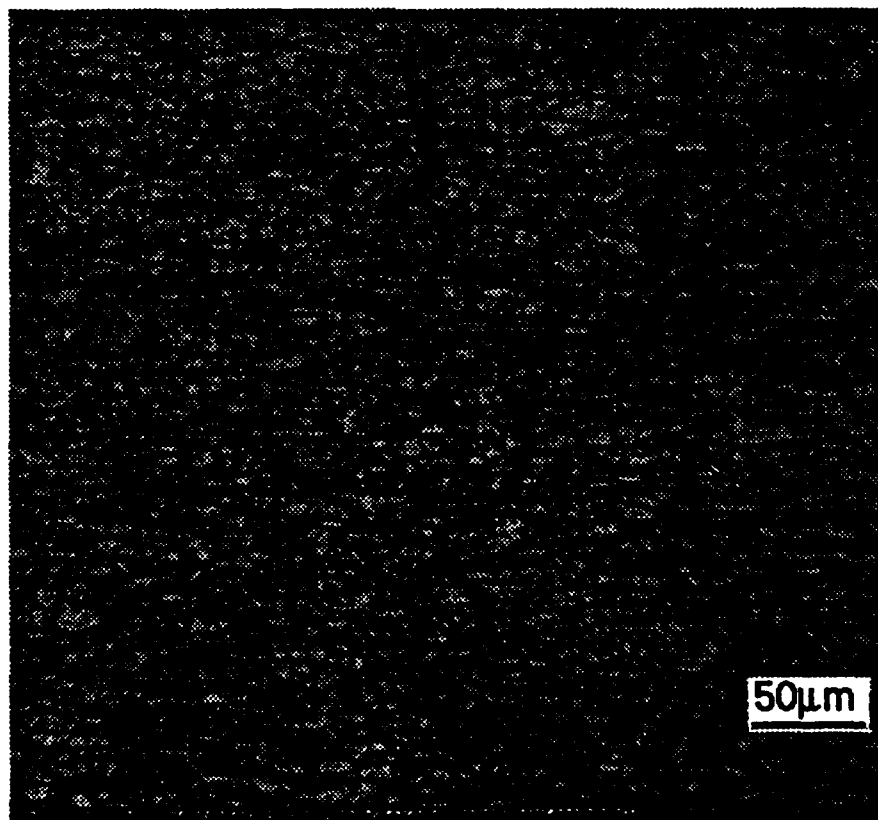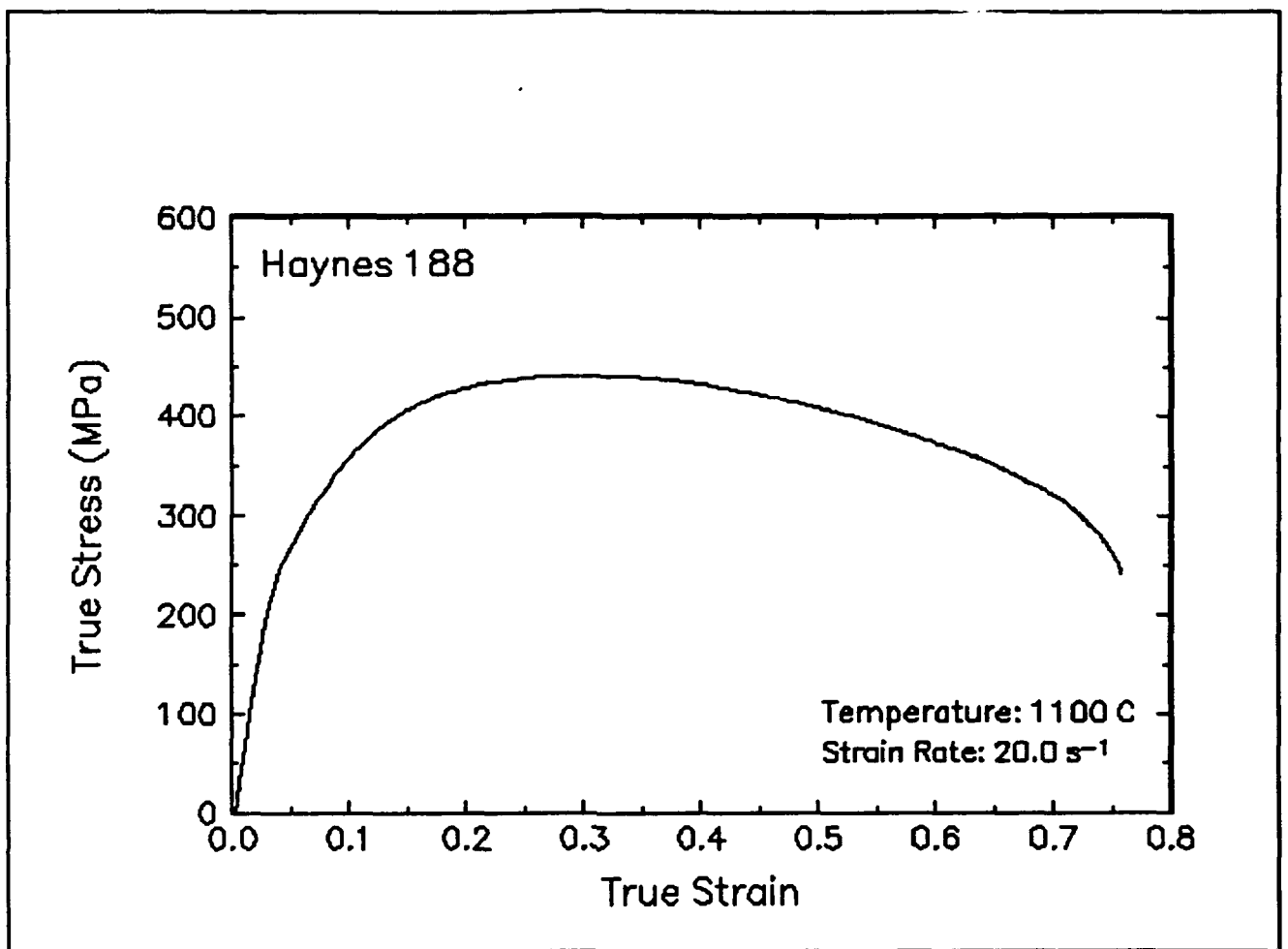
Figure 24. True stress-true strain curve and an optical micrograph from the center of the compressed sample cut through the compression axis, 1050 C and 5 s^{-1}.

27

Figure 25. True stress-true strain curve and an optical micrograph from the center of the compressed sample cut through the compression axis, 1050 C and 20 s^{-1}.
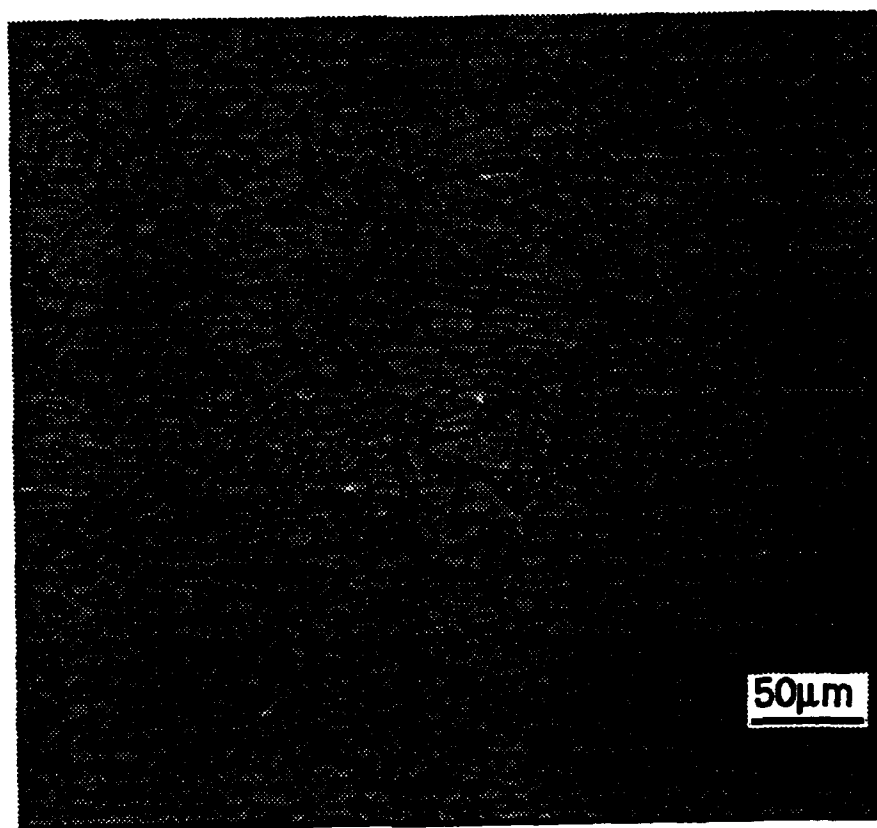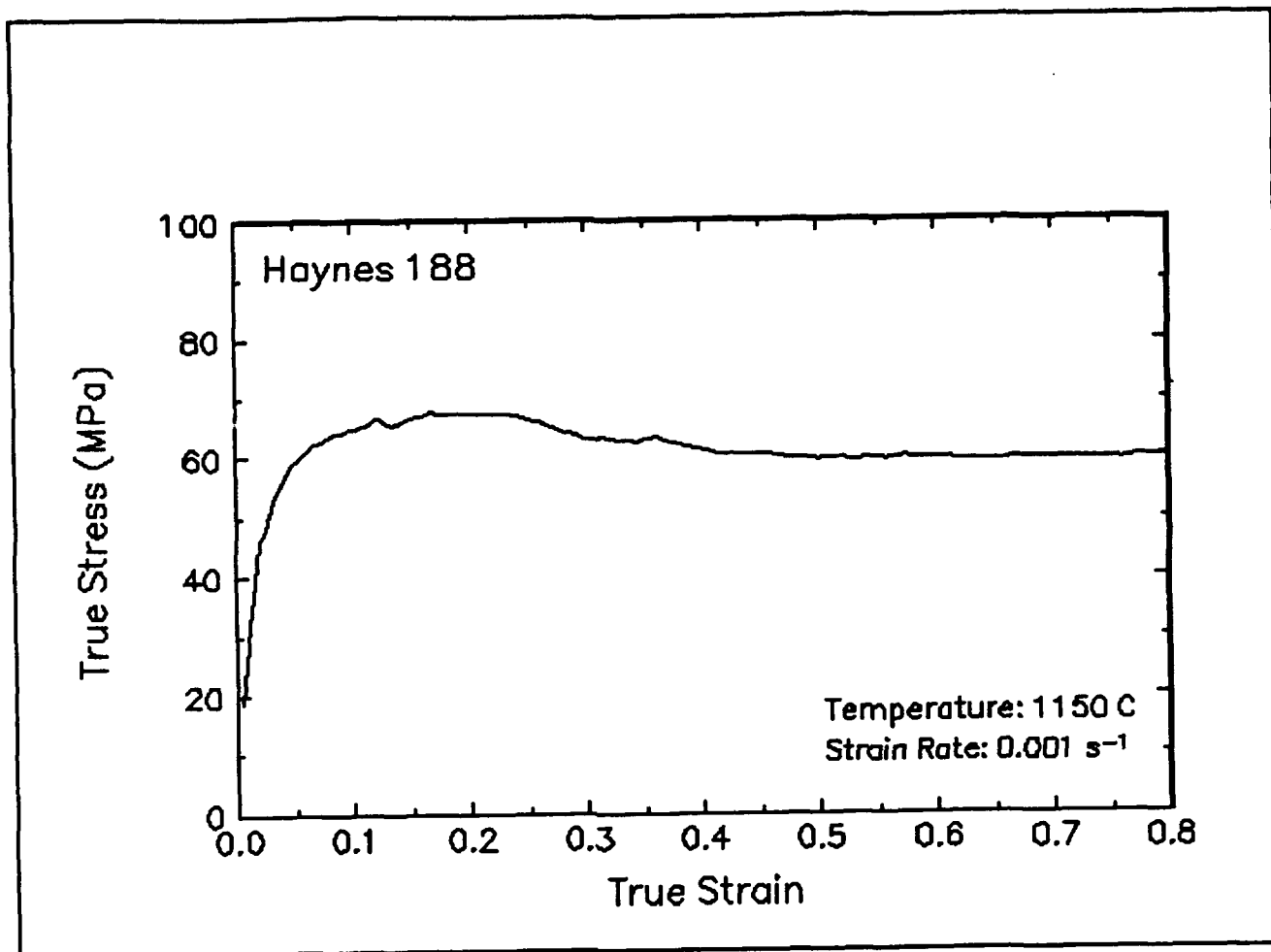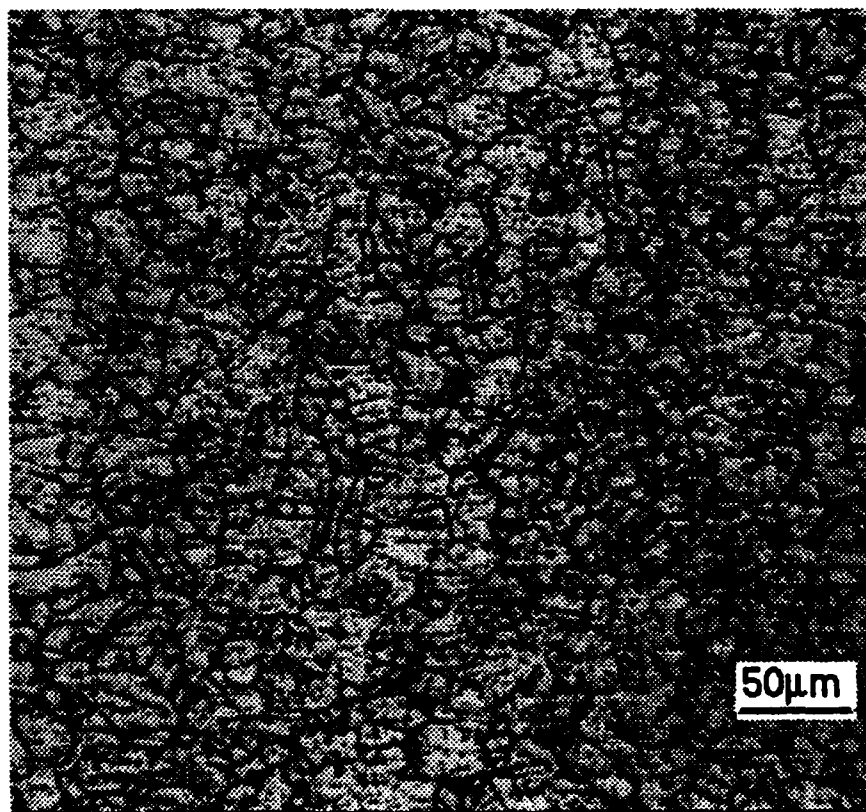
28

Figure 26. True stress-true strain curve and an optical micrograph from the center of the compressed sample cut through the compression axis, 1100 C and 0.001 s^{-1}.
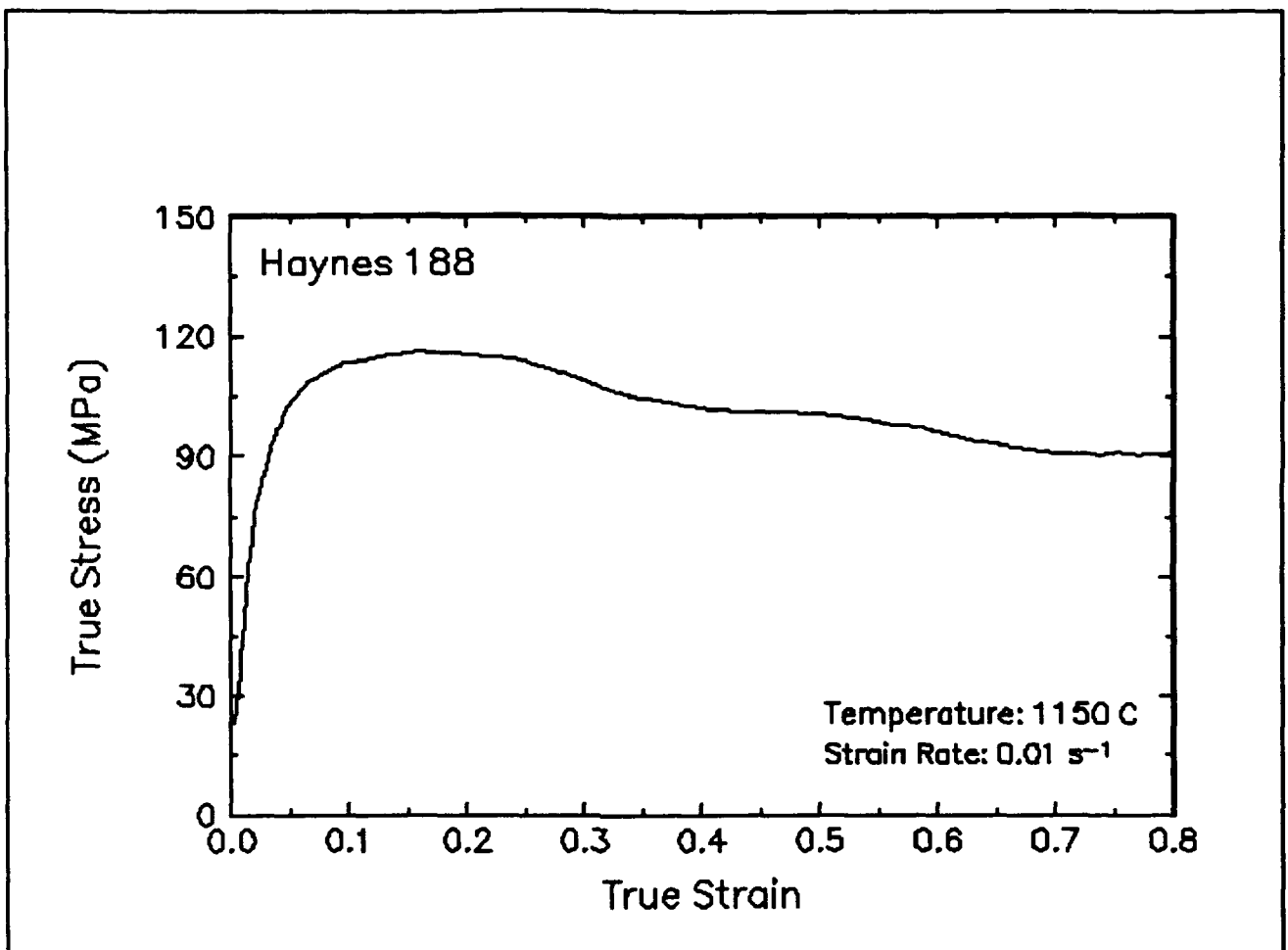
Figure 27. True stress-true strain curve and an optical micrograph from the center of the compressed sample cut through the compression axis, 1100 C and 0.01 s^{-1}.

Figure 28. True stress-true strain curve, 1100 C and 0.05 s^{-1}.

Figure 29. True stress-true strain curve and an optical micrograph from the center of the compressed sample cut through the compression axis, 1100 C and 0.1 s^{-1}.
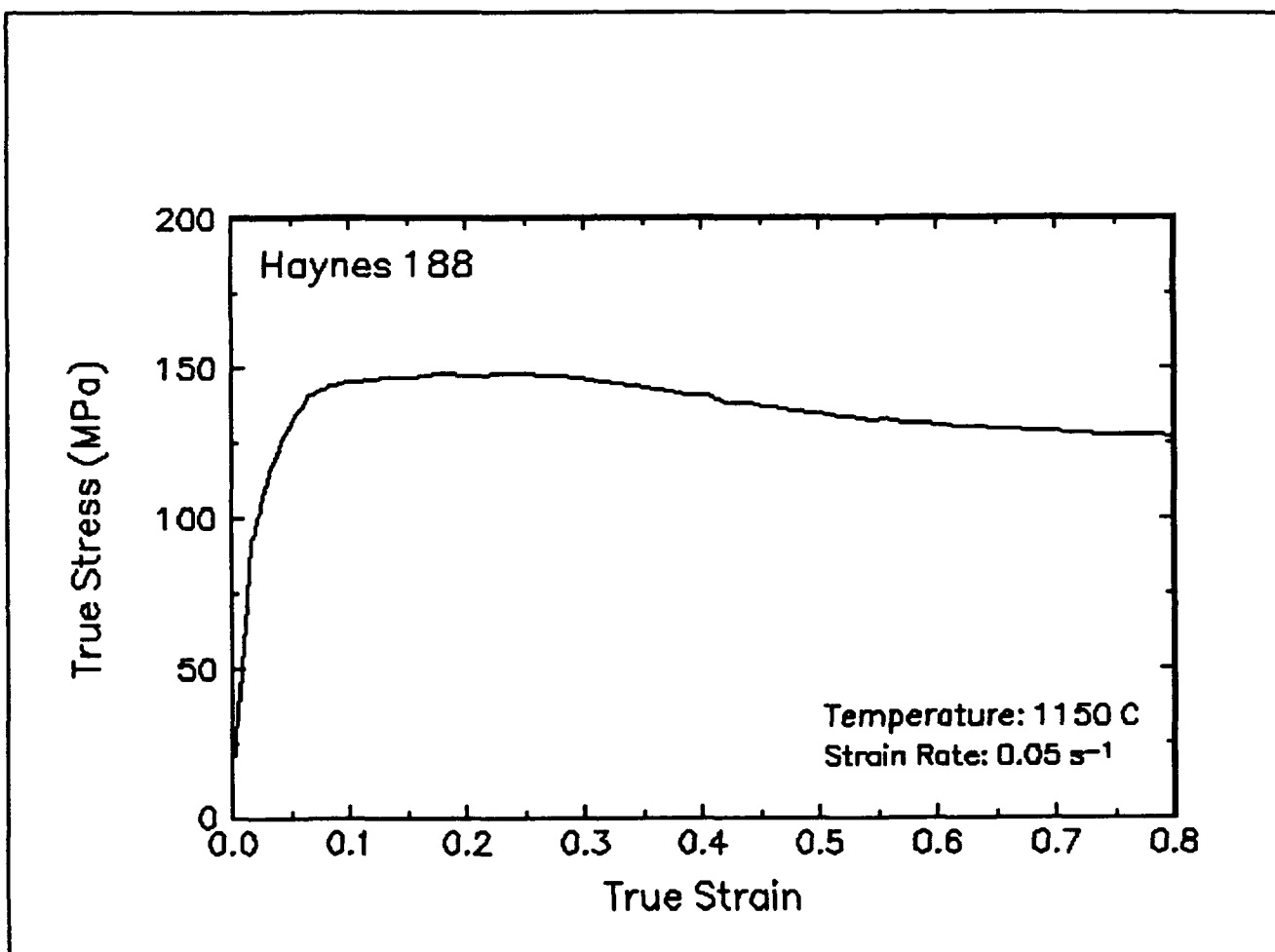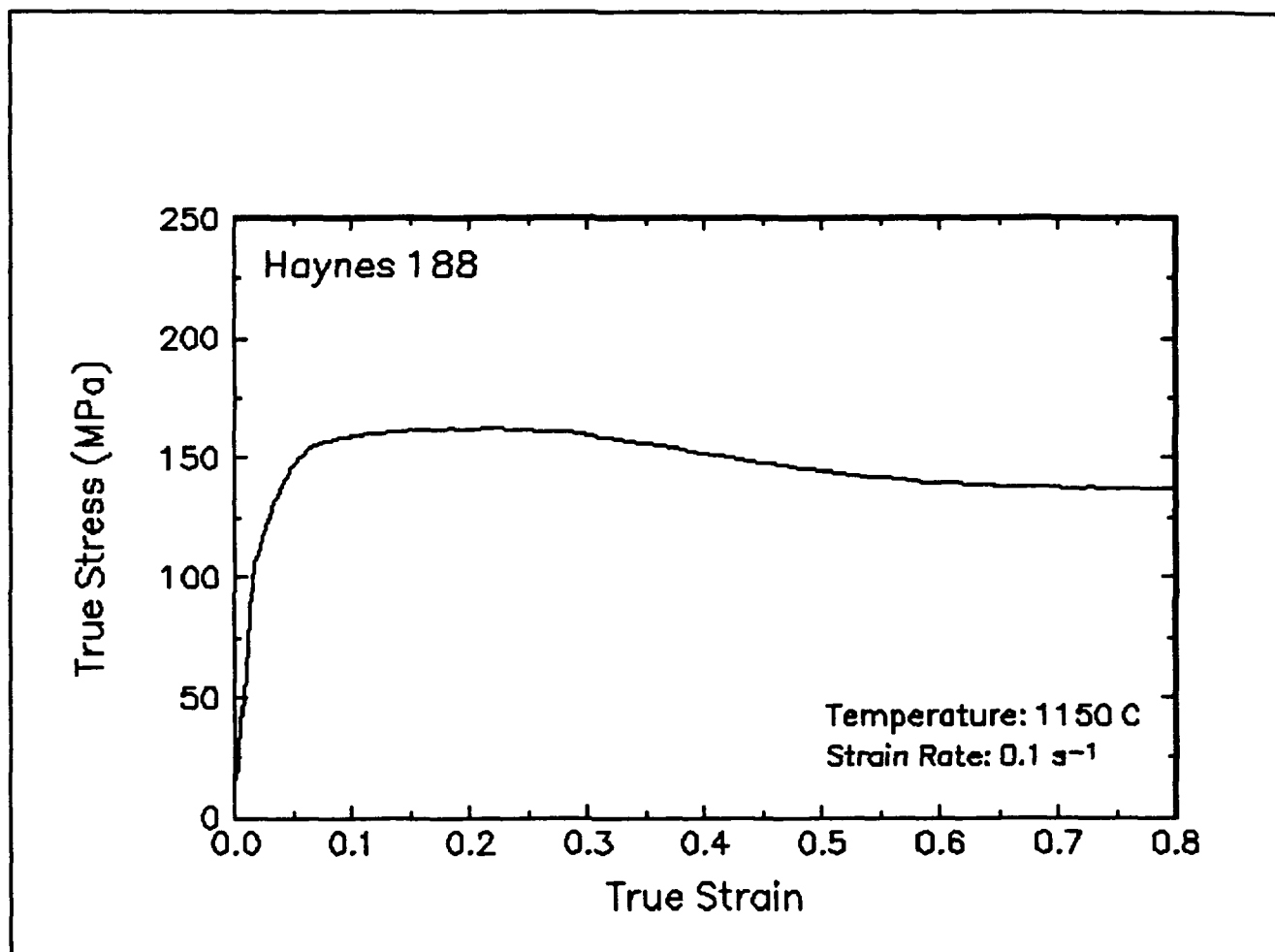
32

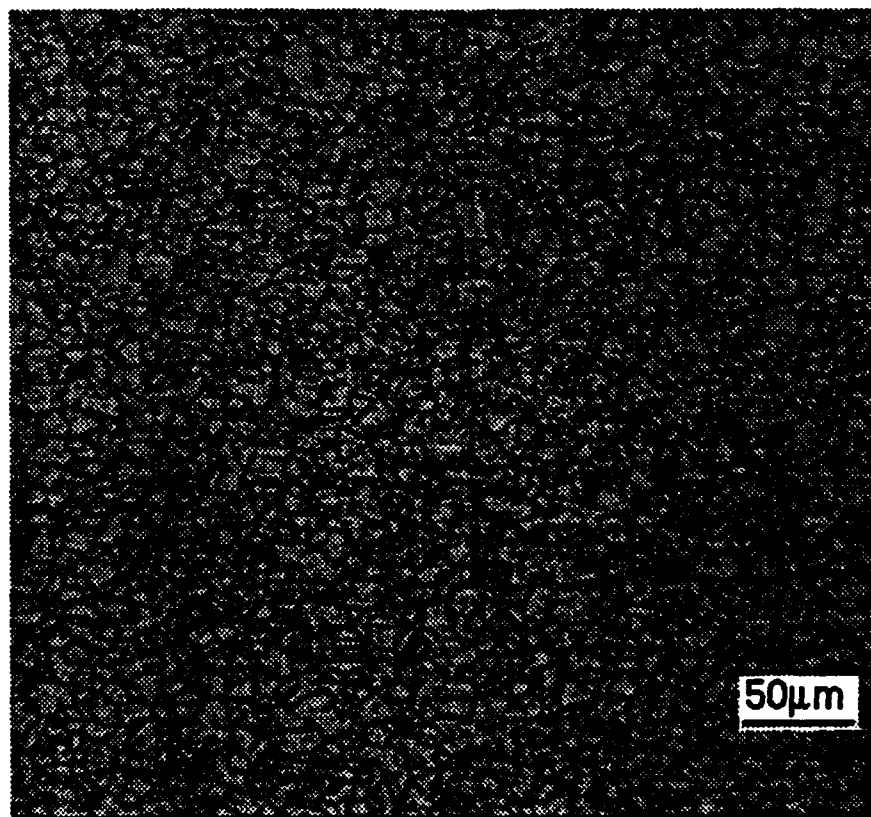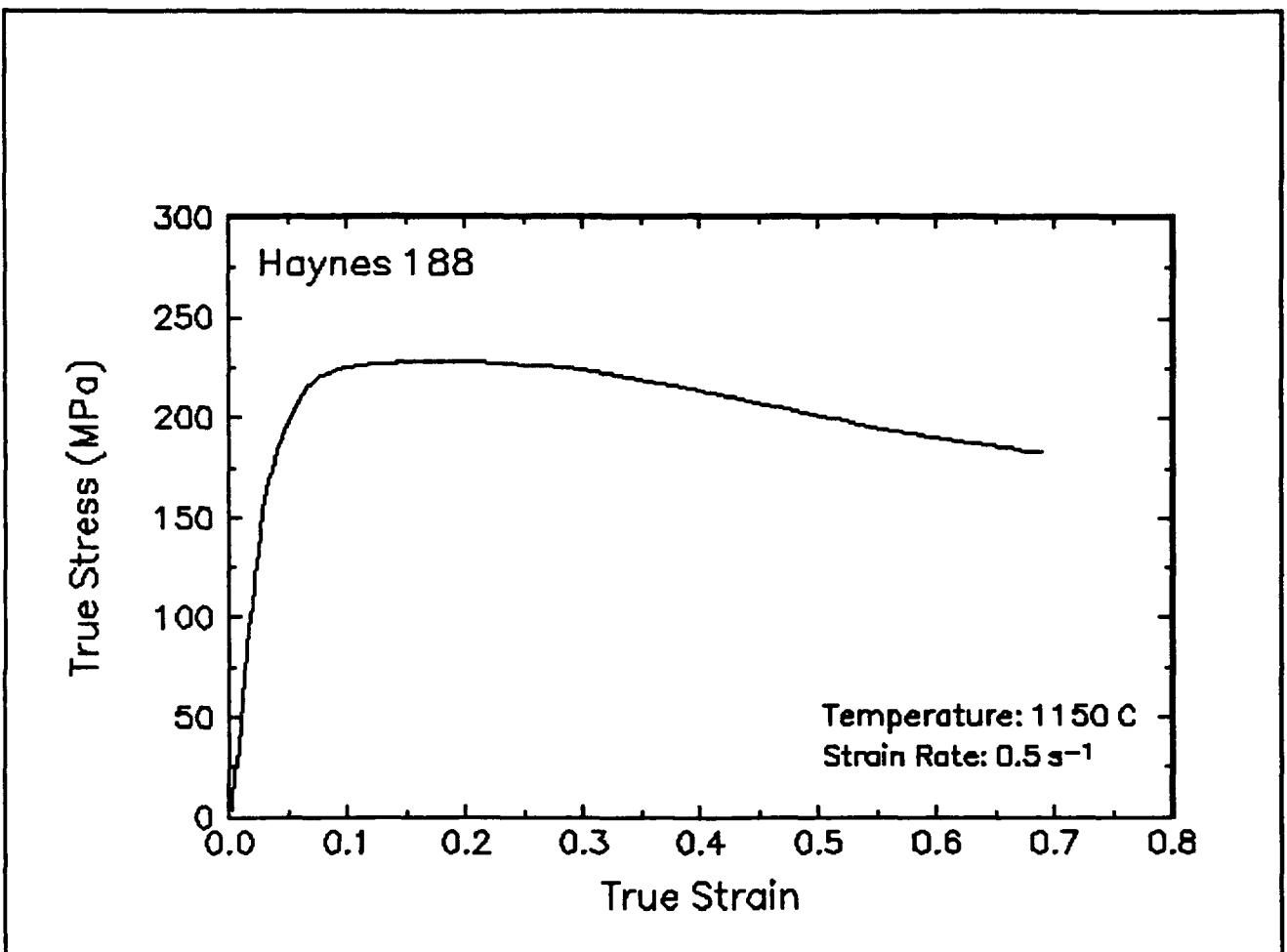Figure 30. True stress-true strain curve, 1100 C and 0.5 s^{-1}.

Figure 31. True stress-true strain curve and an optical micrograph from the center of the compressed sample cut through the compression axis, 1100 C and 1 s⁻¹.

Figure 32. True stress-true strain curve, 1100 C and 5 s^{-1}.

Figure 33. True stress-true strain curve and an optical micrograph from the center of the compressed sample cut through the compression axis, 1100 C and 20 s^{-1}.
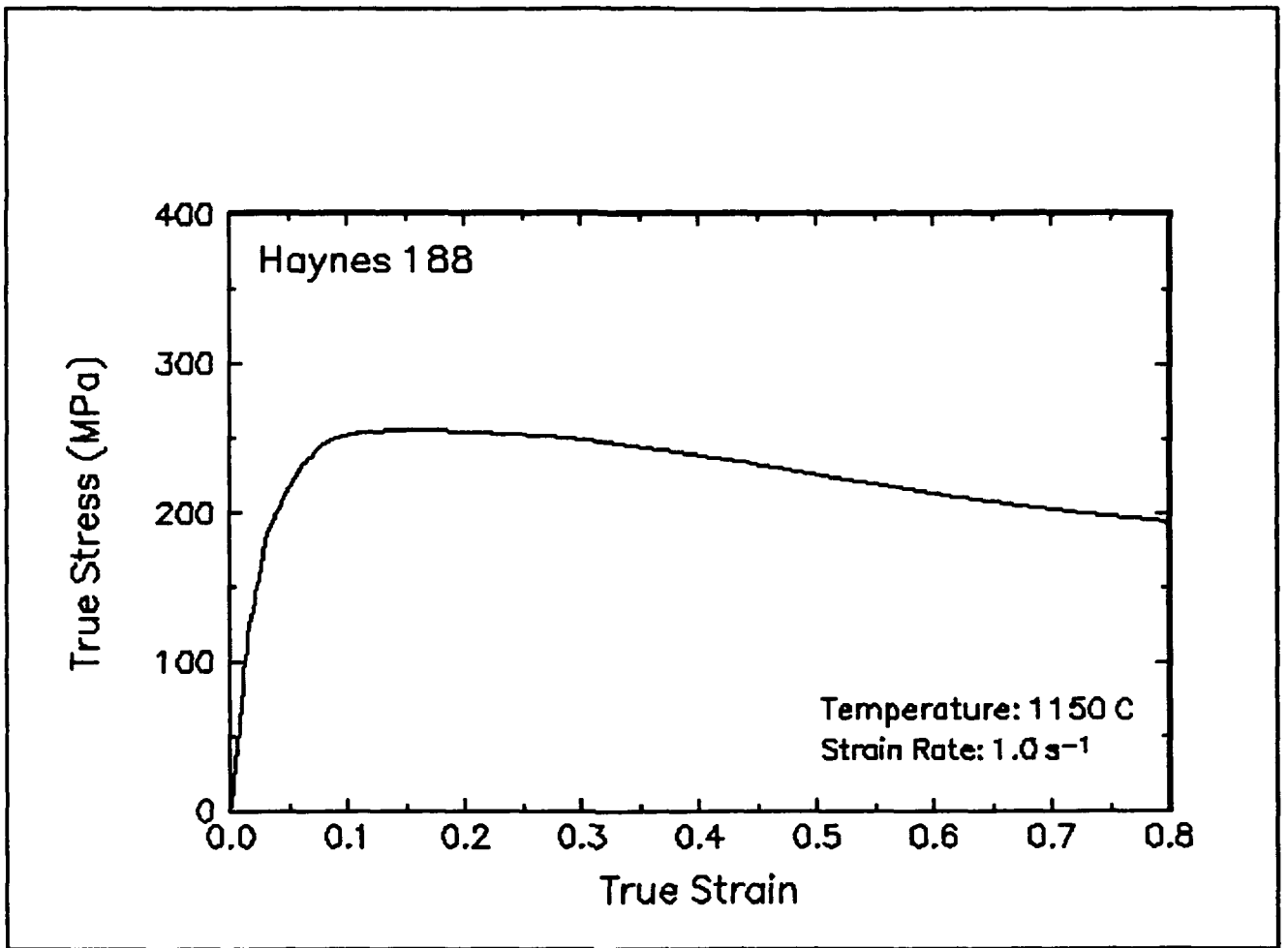
36

Figure 34. True stress-true strain curve and an optical micrograph from the center of the compressed sample cut through the compression axis, 1150 C and 0.001 s^{-1}.

37

Figure 35. True stress-true strain curve and an optical micrograph from the center of the compressed sample cut through the compression axis, 1150 C and 0.01 s⁻¹.
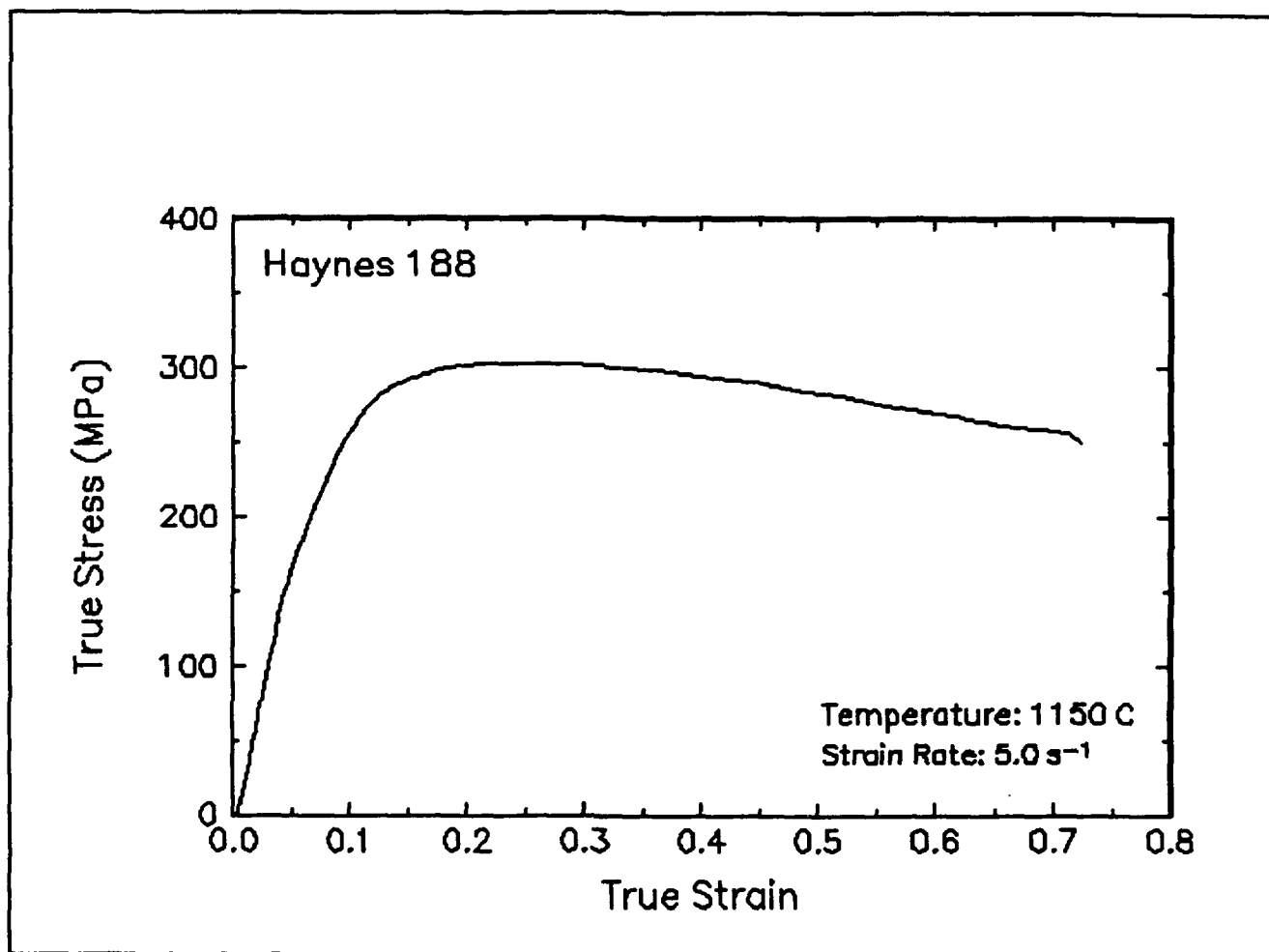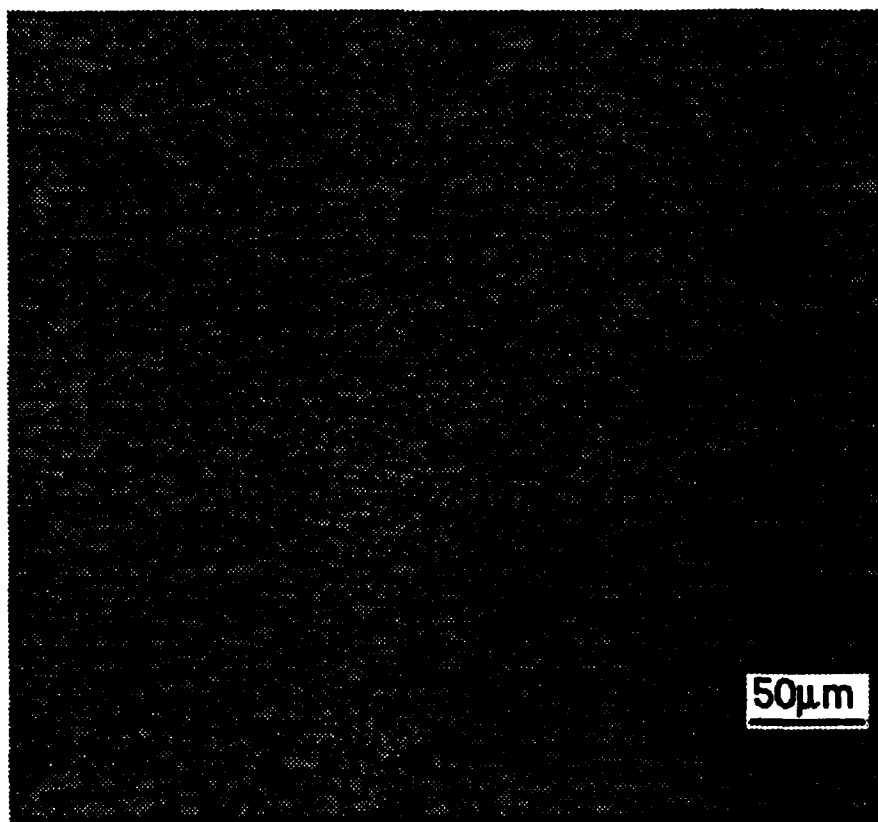
Figure 36. True stress-true strain curve, 1150 C and 0.05 s^{-1}.

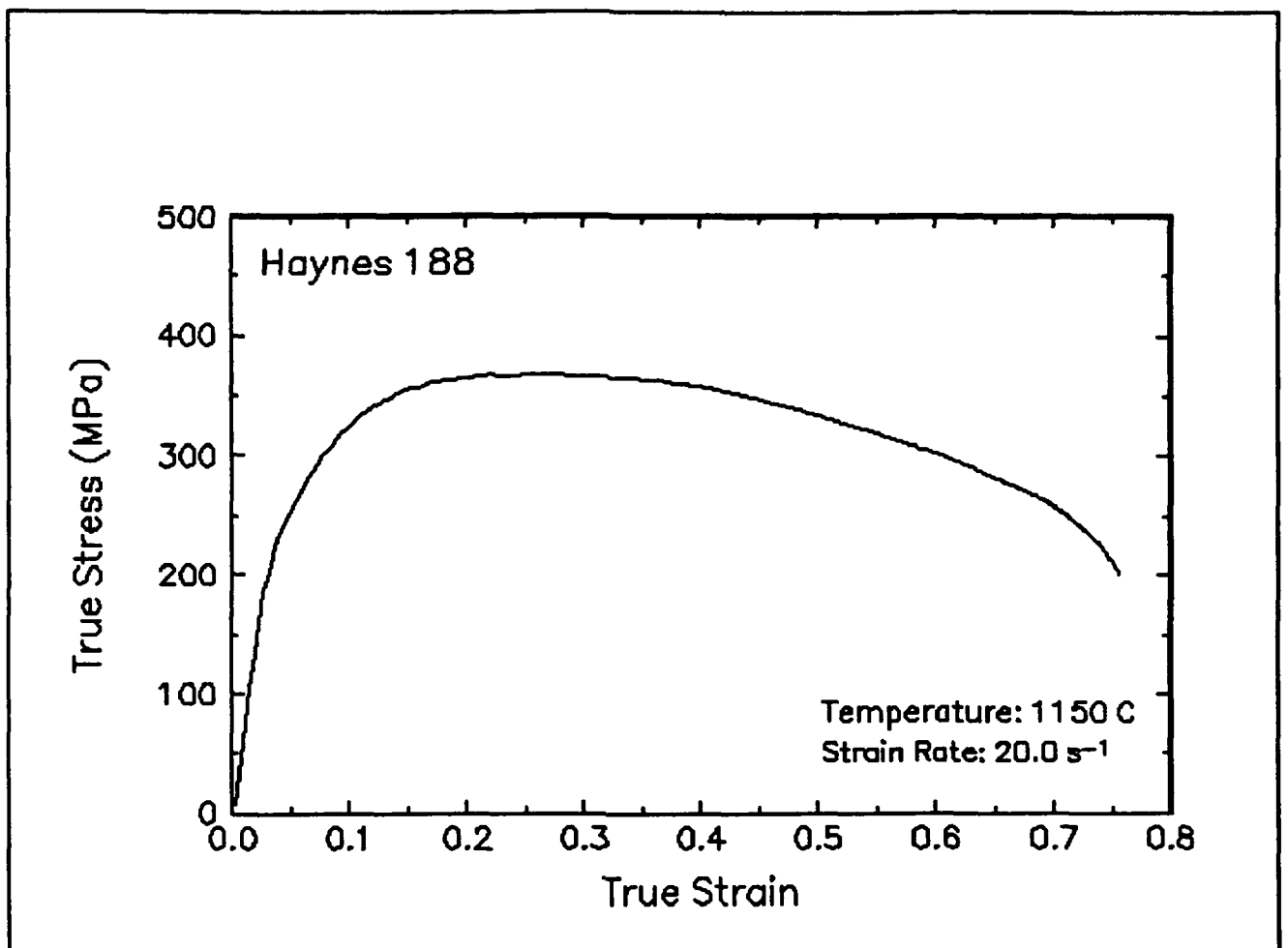Figure 37. True stress-true strain curve, 1150 C and 0.1 s^{-1}.

Figure 38. True stress-true strain curve and an optical micrograph from the center of the compressed sample cut through the compression axis, 1150 C and 0.5 s^{-1}.

Figure 39. True stress-true strain curve and an optical micrograph from the center of the compressed
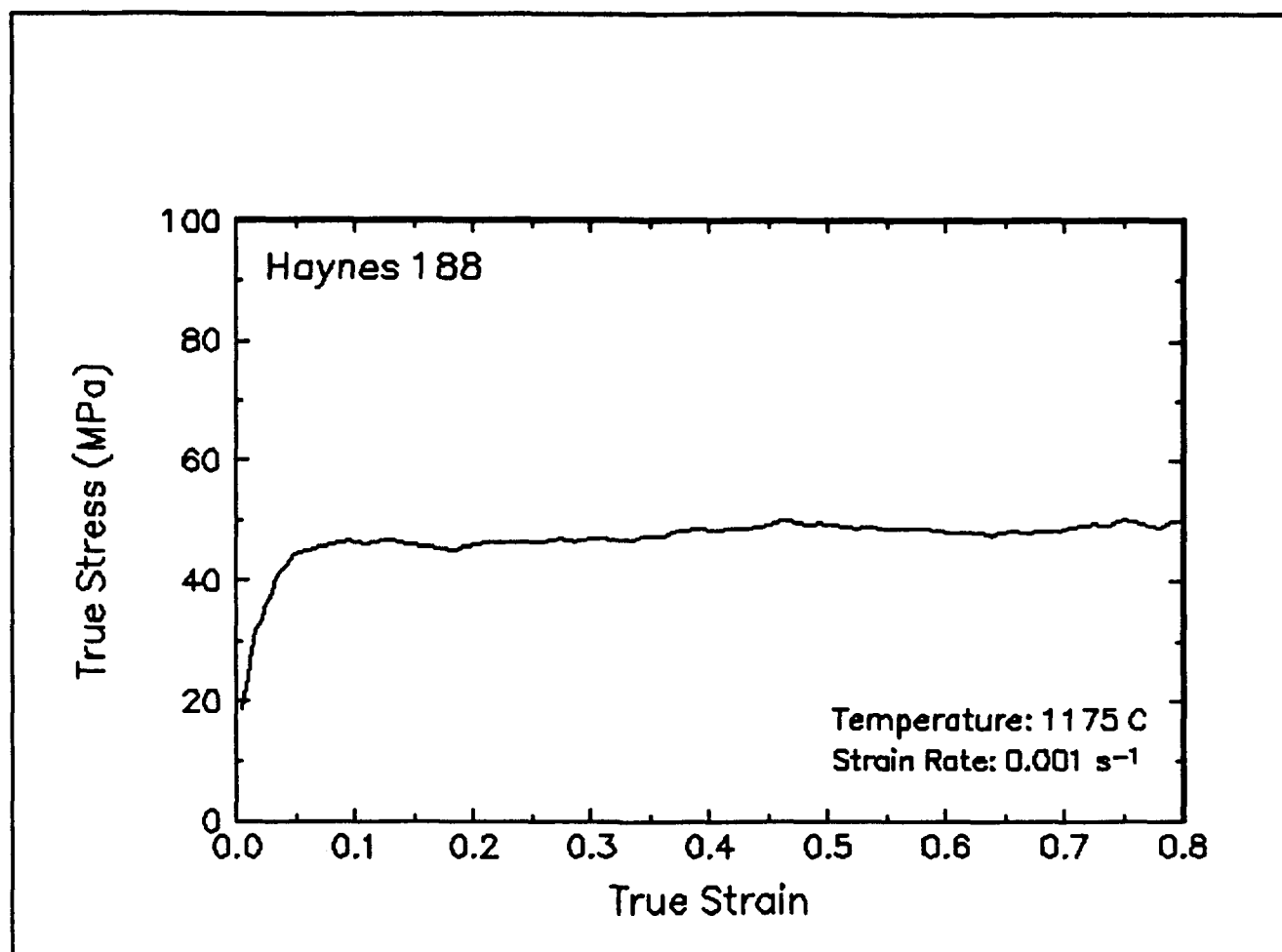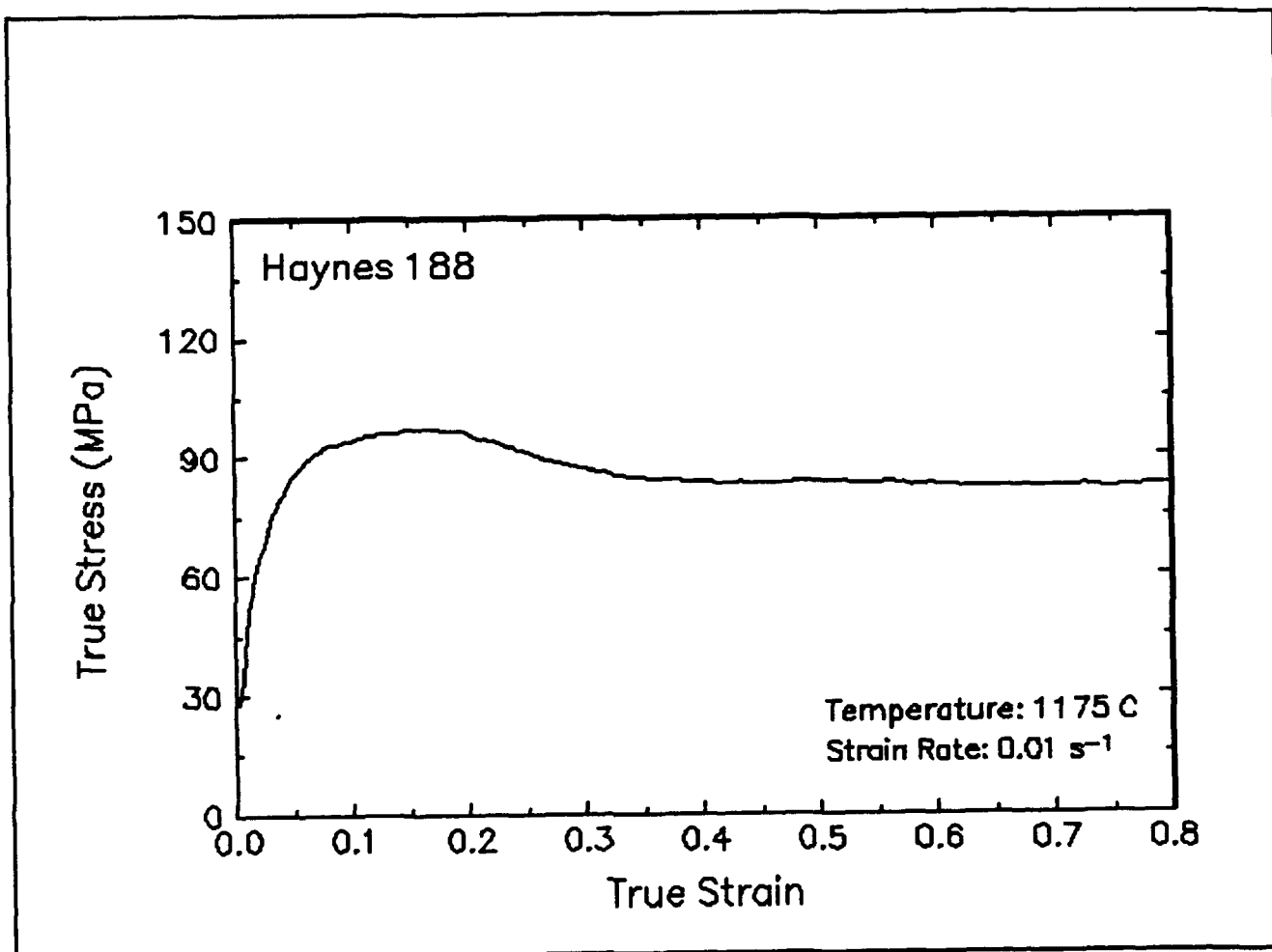sample cut through the compression axis, 1150 C and 1 s⁻¹.

Figure 40. True stress-true strain curve, 1150 C and 5 s^{-1}.

Figure 41. True stress-true strain curve and an optical micrograph from the center of the compressed sample cut through the compression axis, 1150 C and 20 s^{-1}.
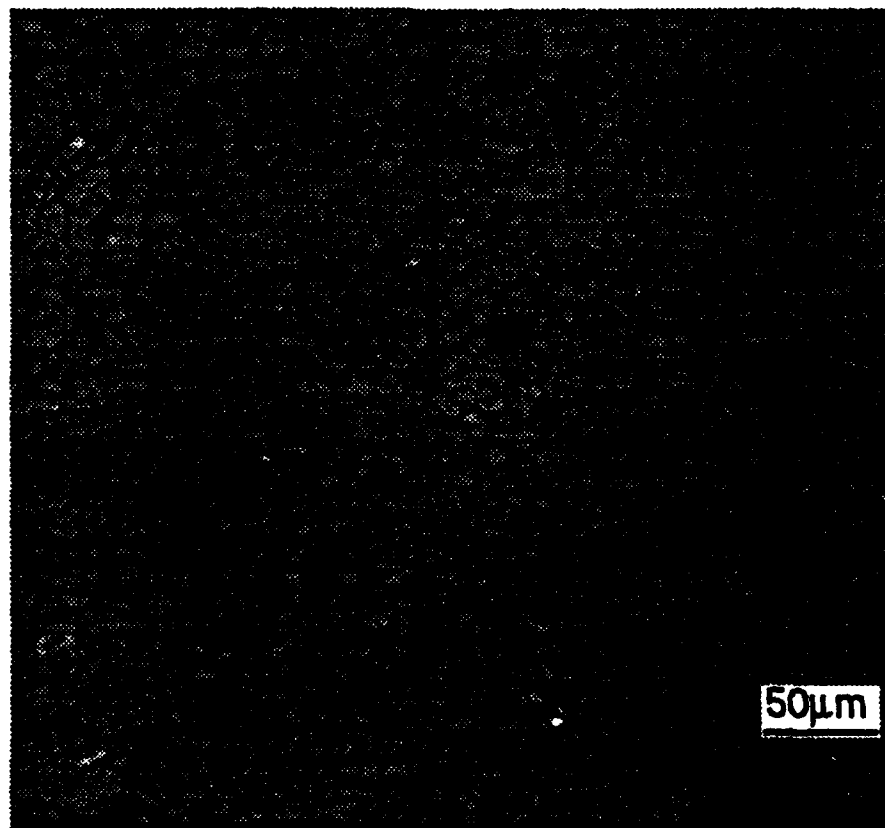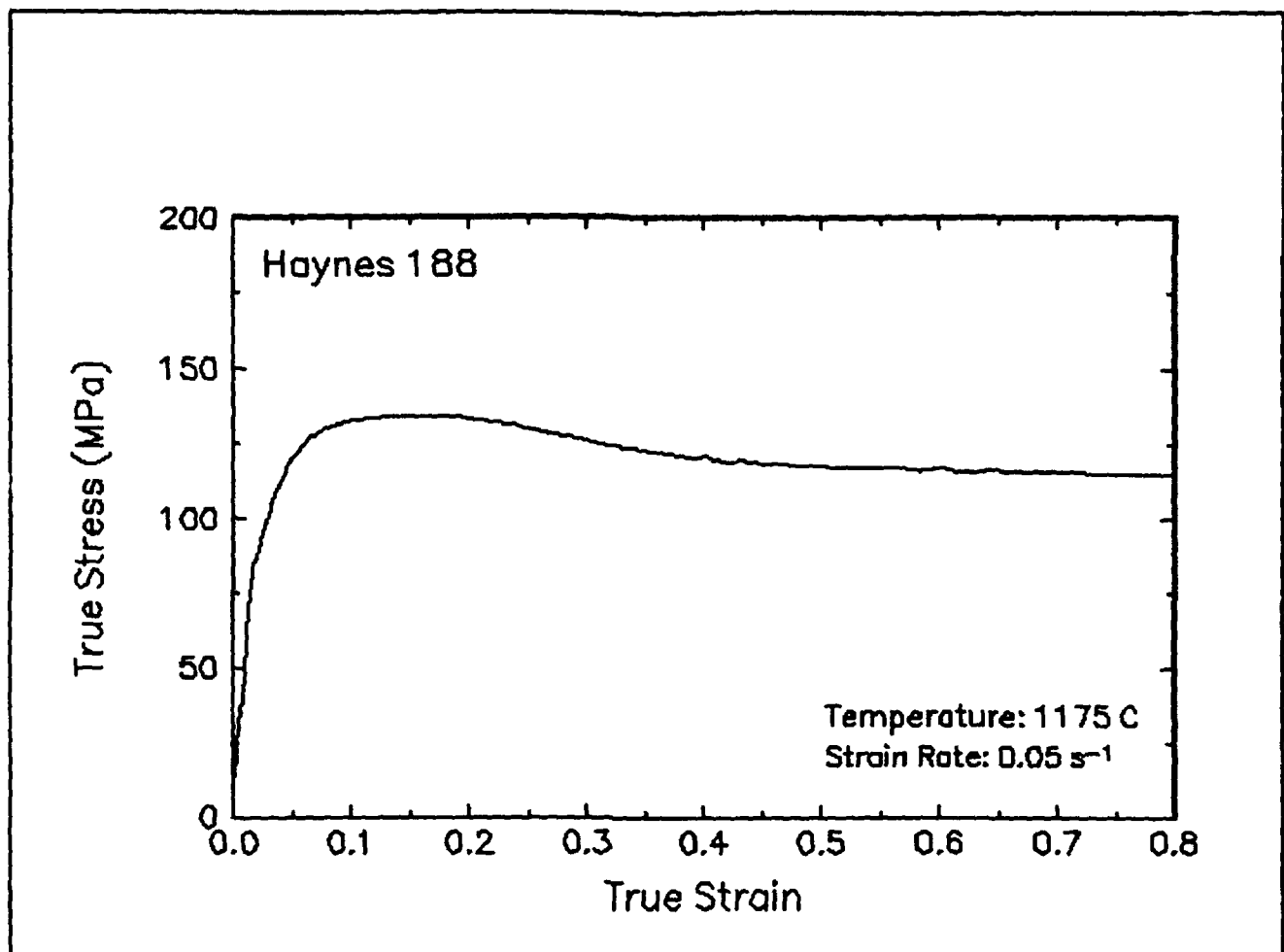
Figure 42. True stress-true strain curve and an optical micrograph from the center of the compressed
sample cut through the compression axis, 1175 C and 0.001 s^{-1}.

Figure 43. True stress-true strain curve, 1175 C and 0.01 s^{-1}.

Figure 44. True stress-true strain curve and an optical micrograph from the center of the compressed sample cut through the compression axis, 1175 C and 0.05 s^{-1}.
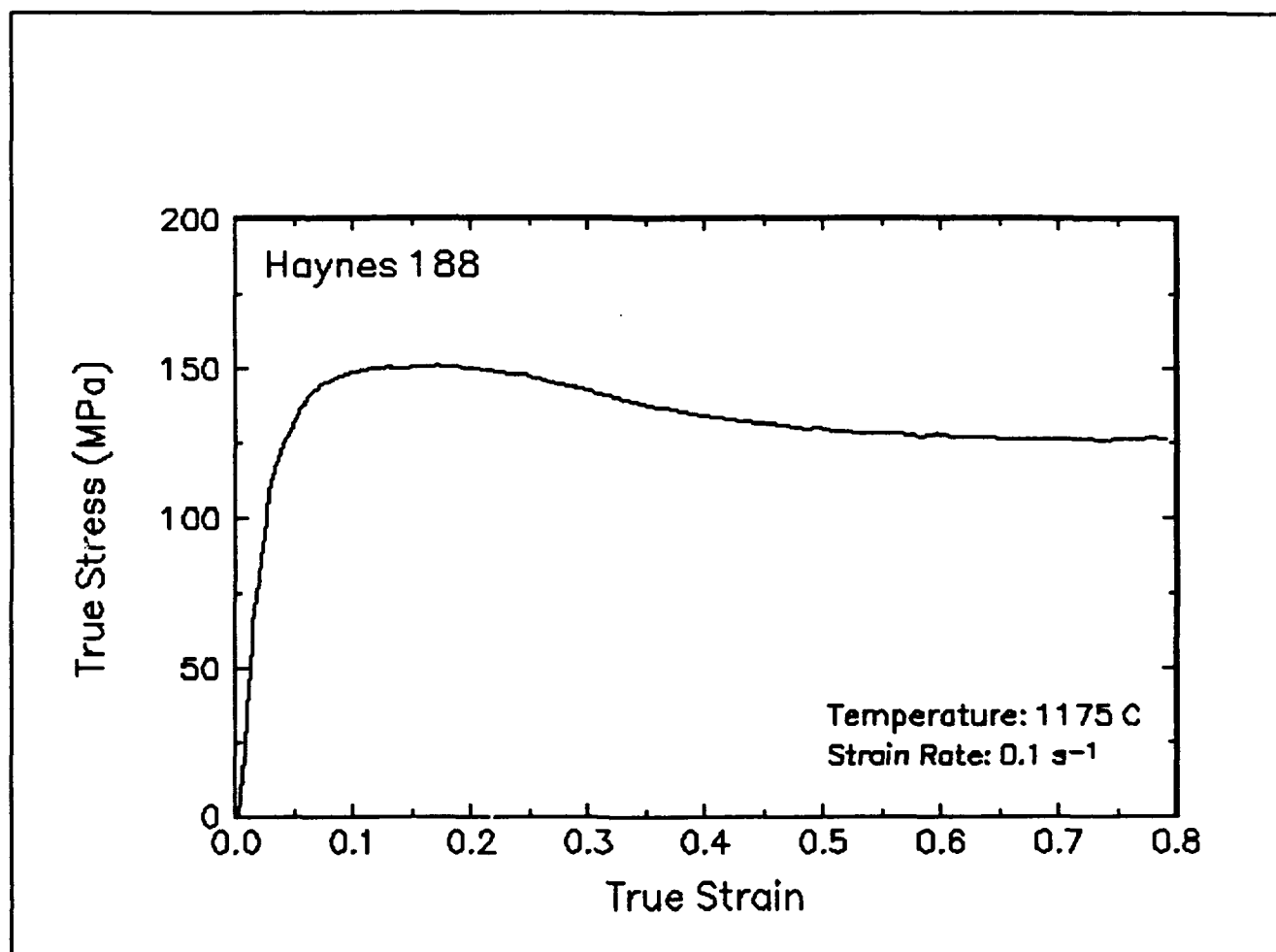
47

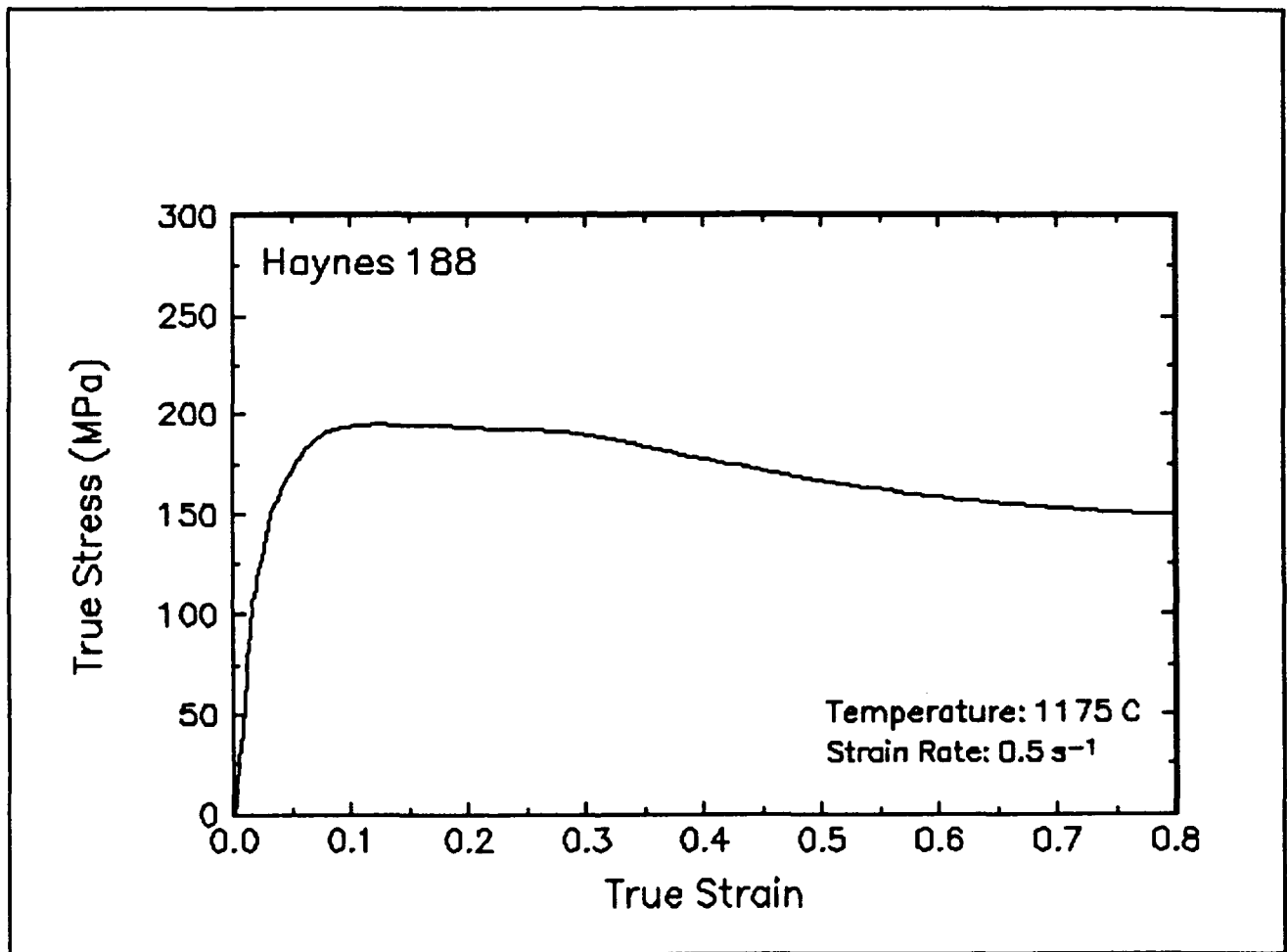Figure 45. True stress-true strain curve, 1175 C and 0.1 s^{-1}.

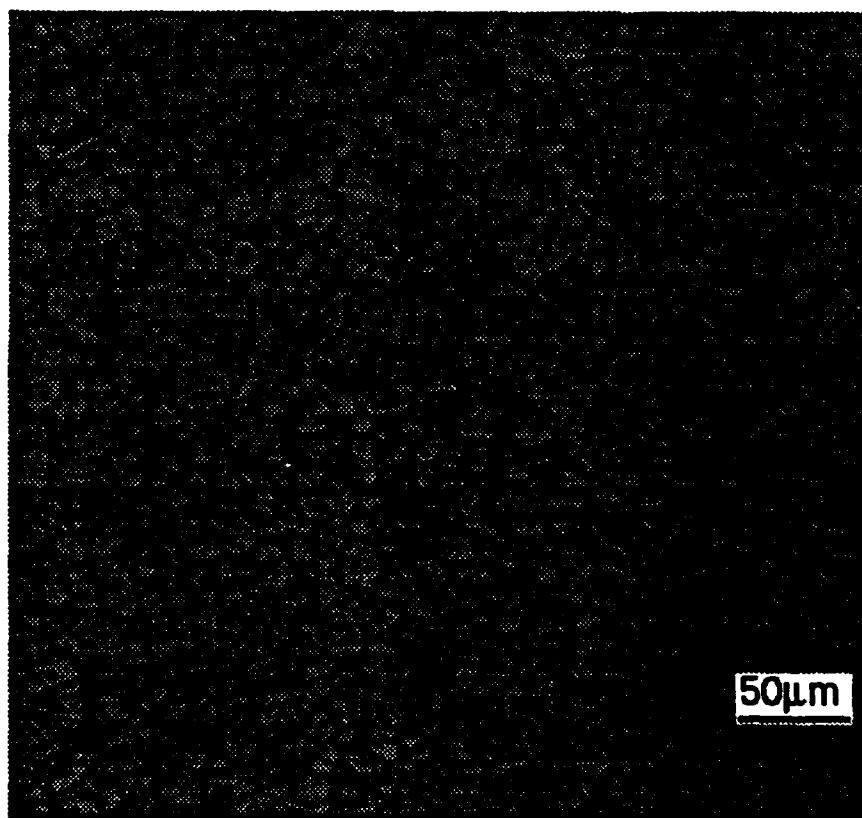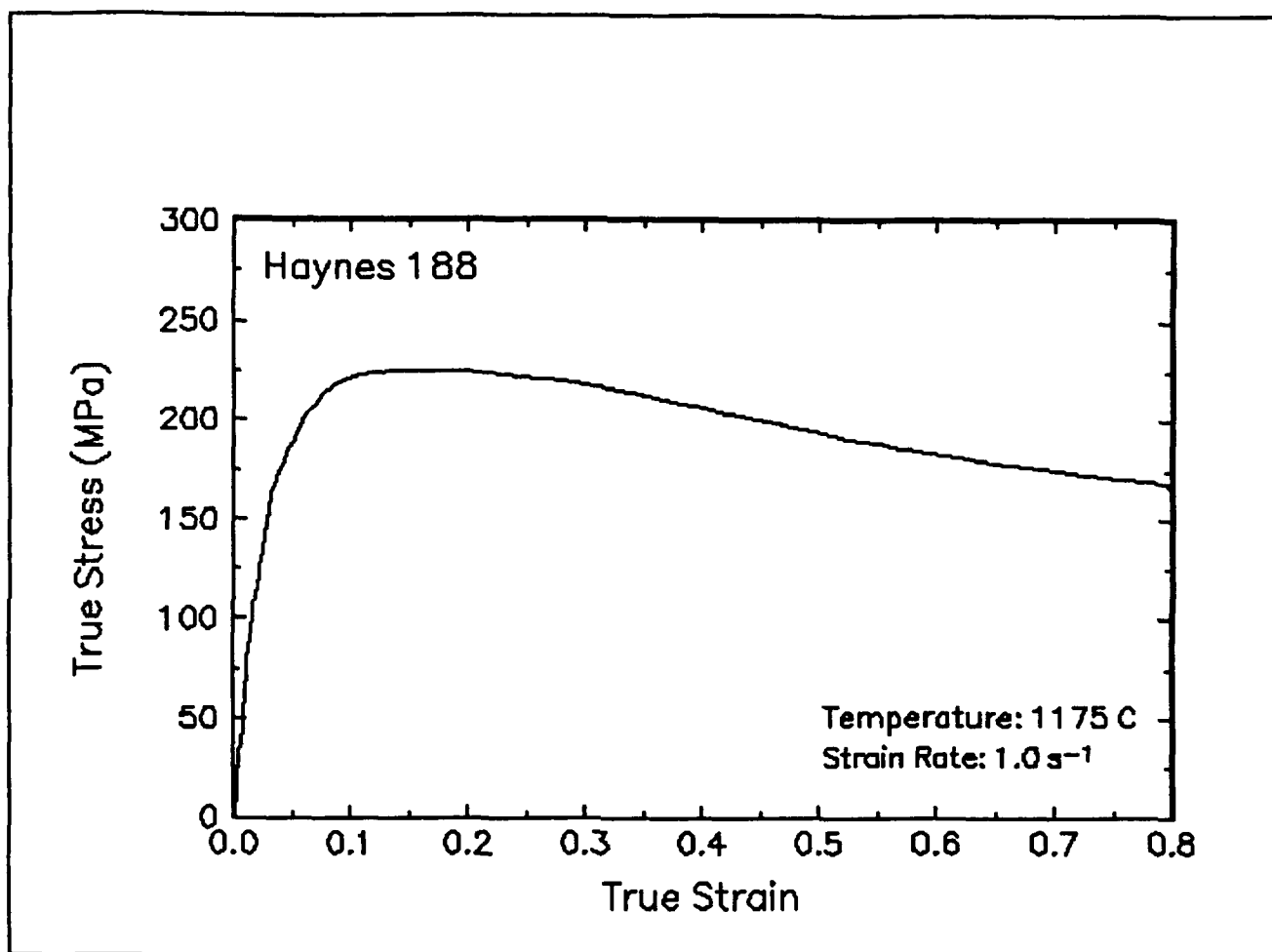Figure 46. True stress-true strain curve, 1175 C and 0.5 s⁻¹.

Figure 47. True stress-true strain curve and an optical micrograph from the center of the compressed sample cut through the compression axis, 1175 C and 1 s^{-1}.
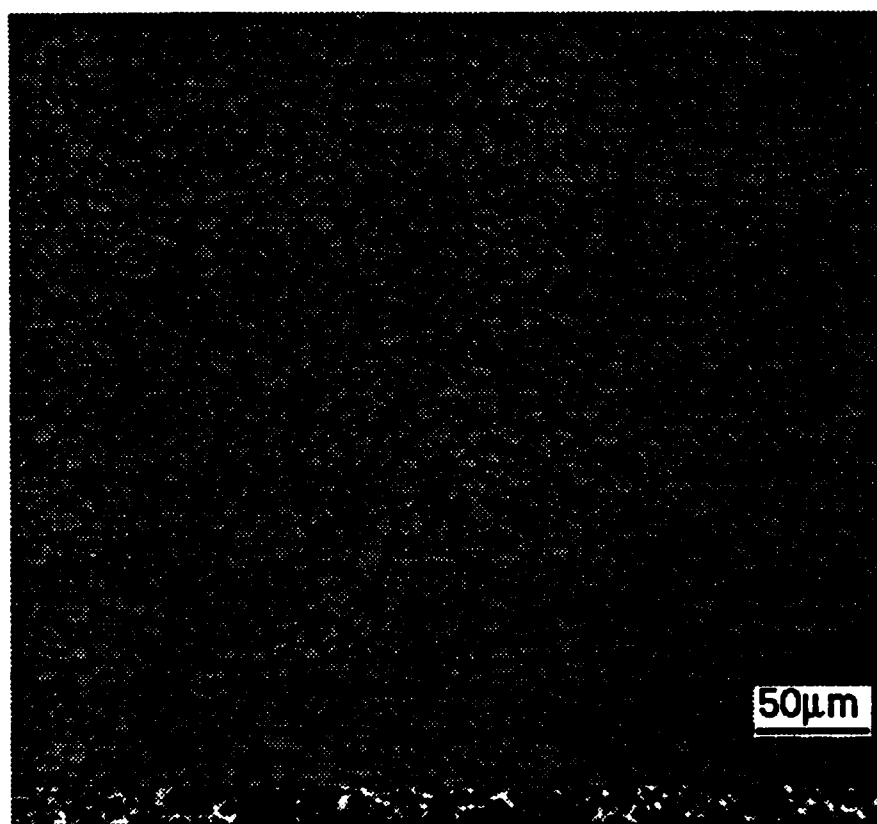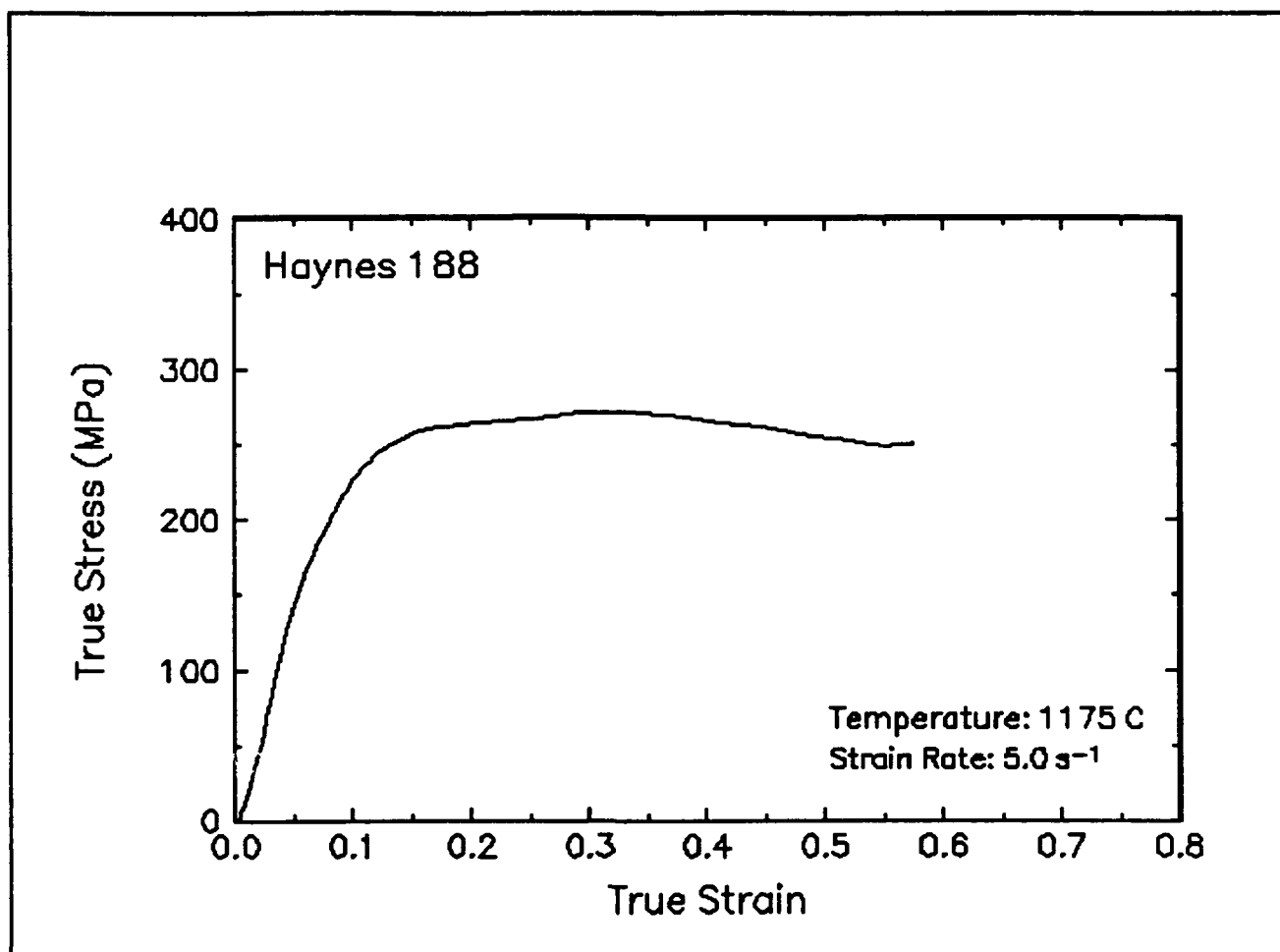
Figure 48. True stress-true strain curve and an optical micrograph from the center of the compressed sample cut through the compression axis, 1175 C and 5 s^{-1}.
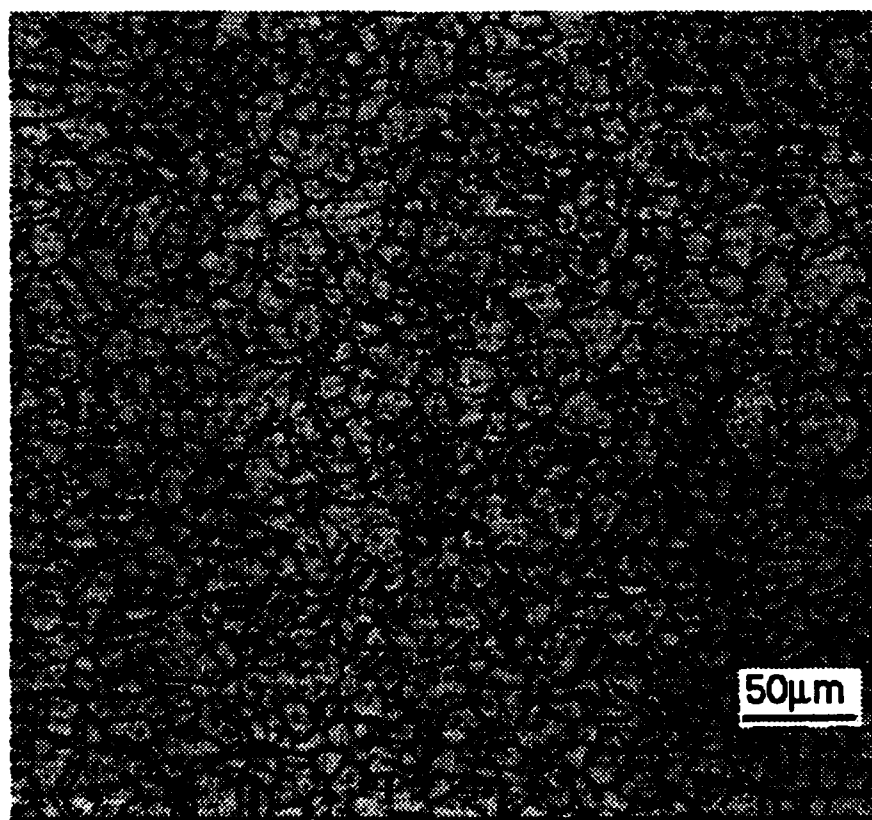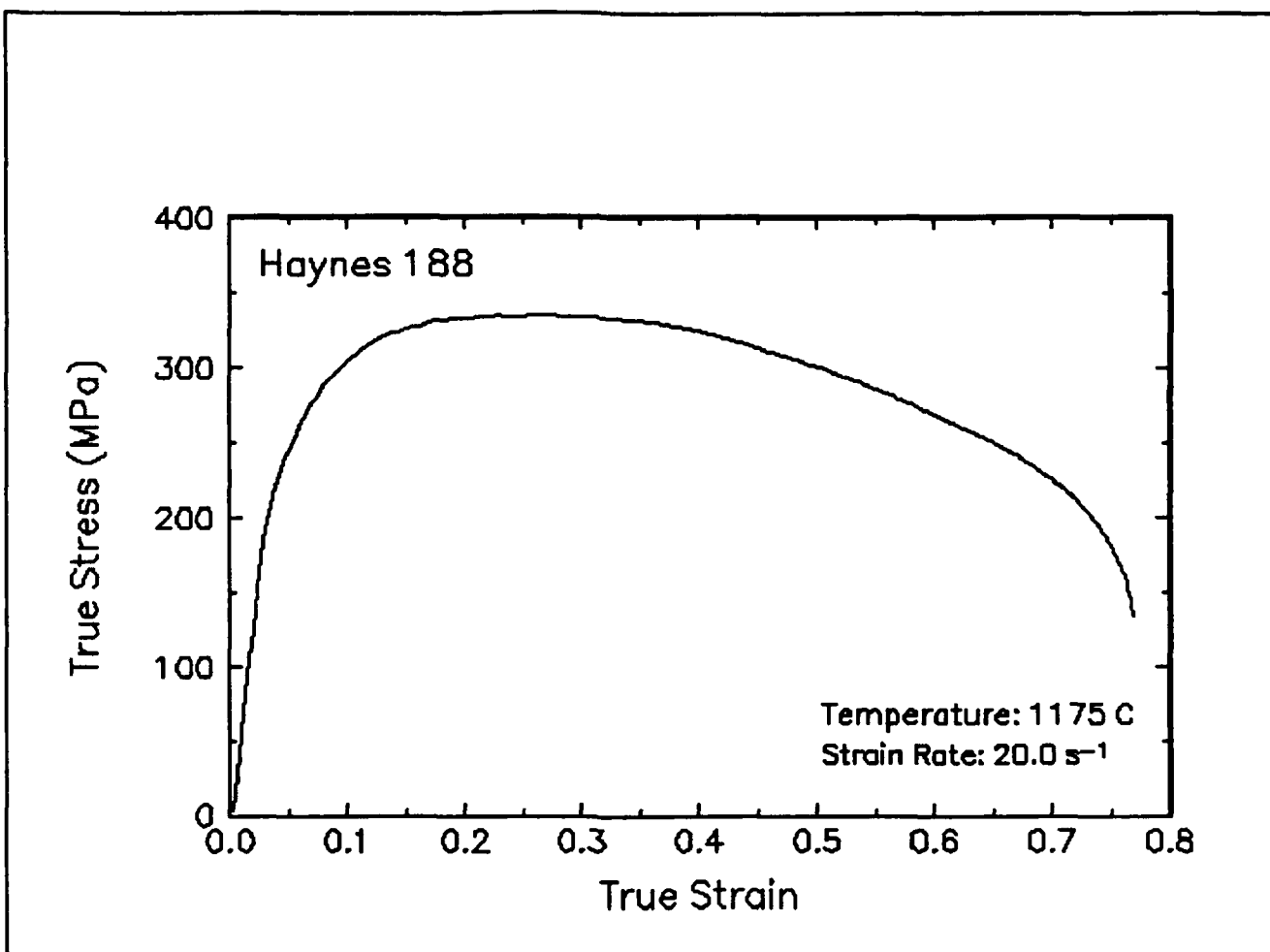
51

Figure 49. True stress-true strain curve and an optical micrograph from the center of the compressed sample cut through the compression axis, 1175 C and 20 s^{-1}.
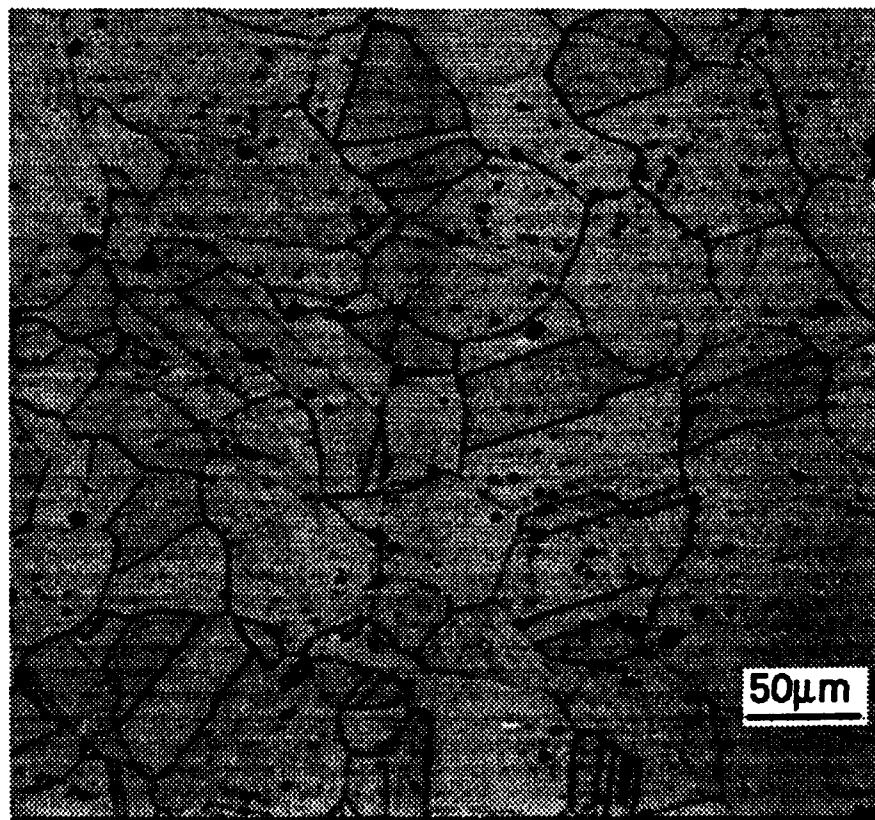
Figure 50. True stress-true strain curve and an optical micrograph from the center of the compressed sample cut through the compression axis, 1200 C and 0.001 s^{-1}.
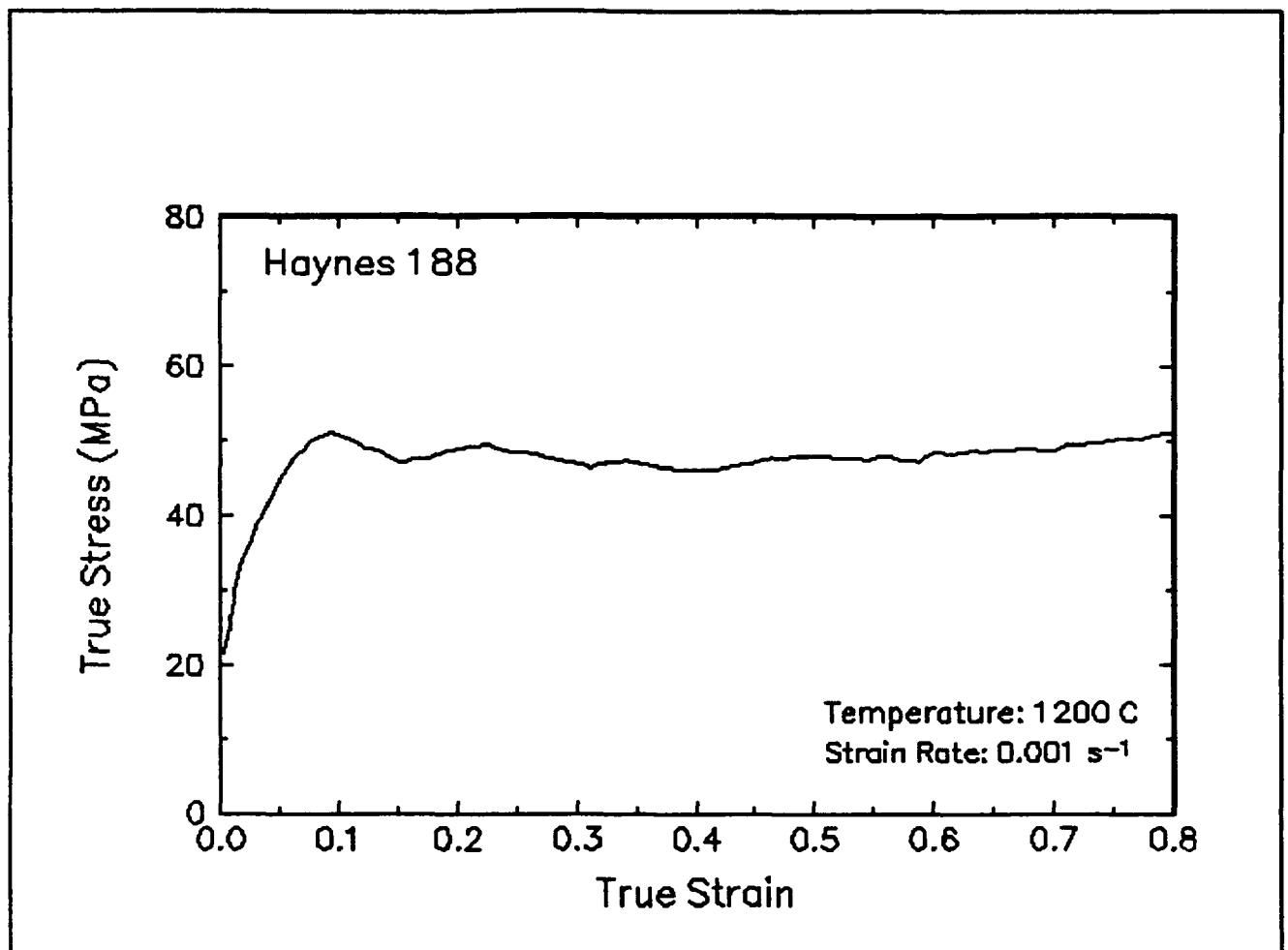
Figure 51. True stress-true strain curve and an optical micrograph from the center of the compressed sample cut through the compression axis, 1200 and 0.01 s^{-1}.

54
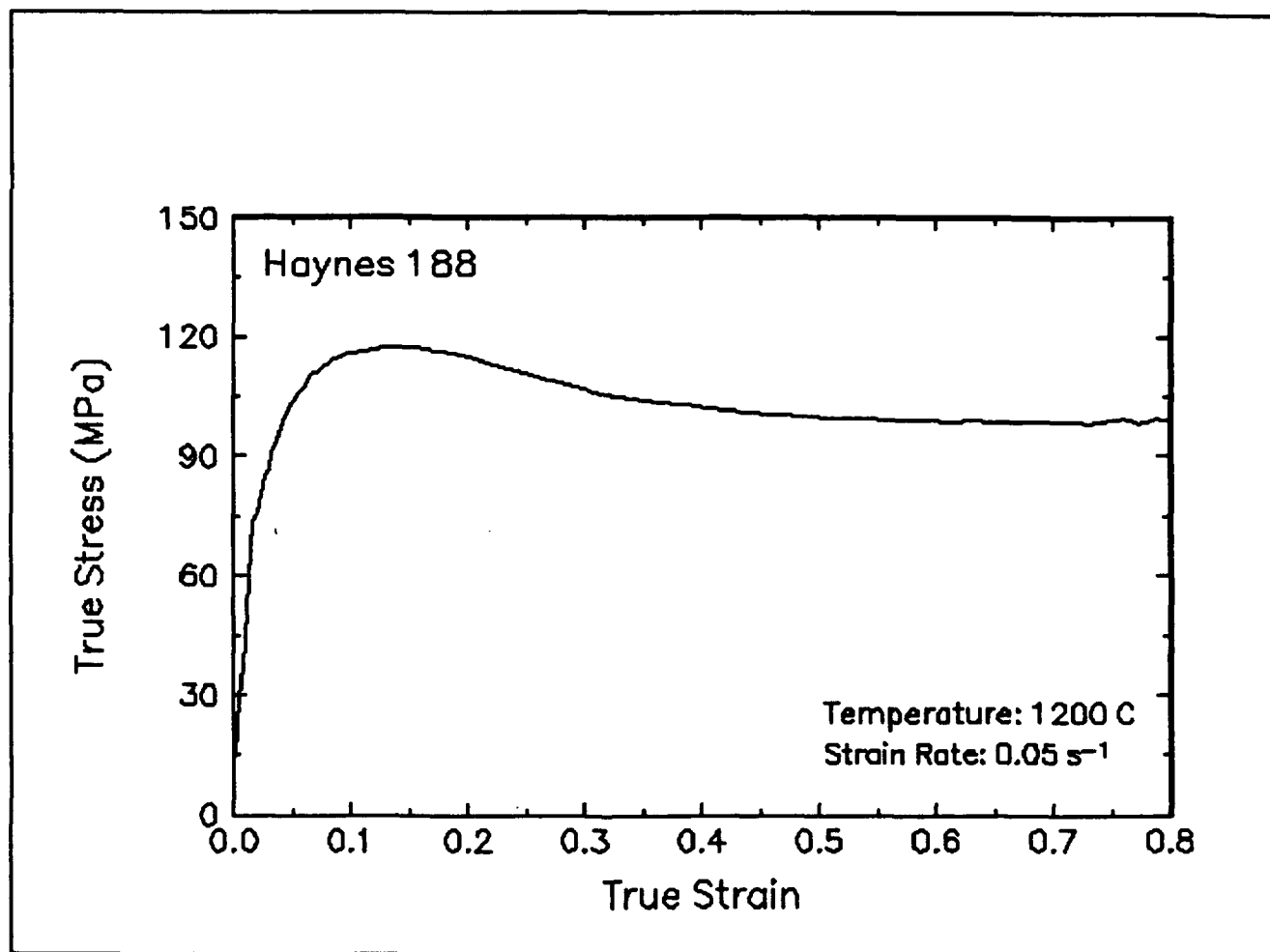
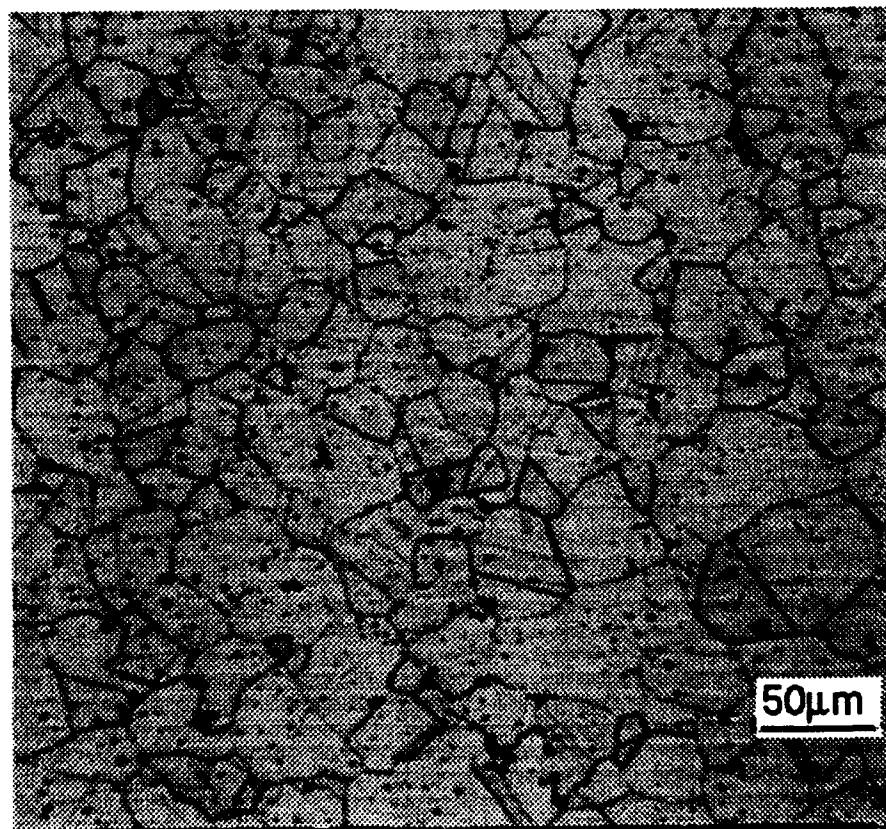Figure 52. True stress-true strain curve, 1200 C and 0.05 s^{-1}.
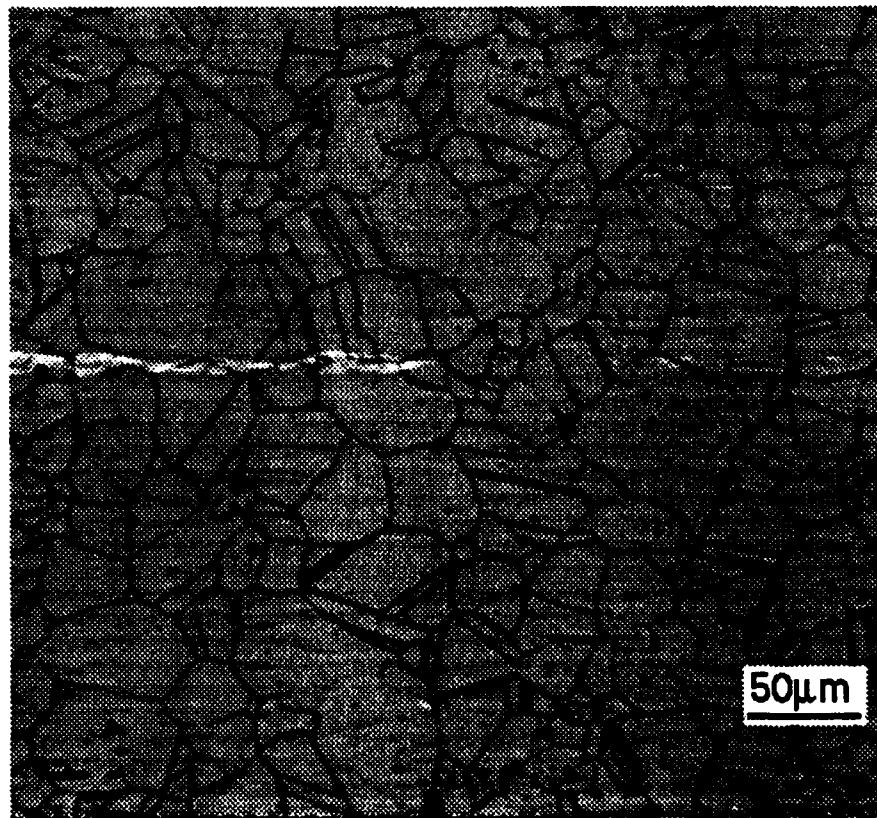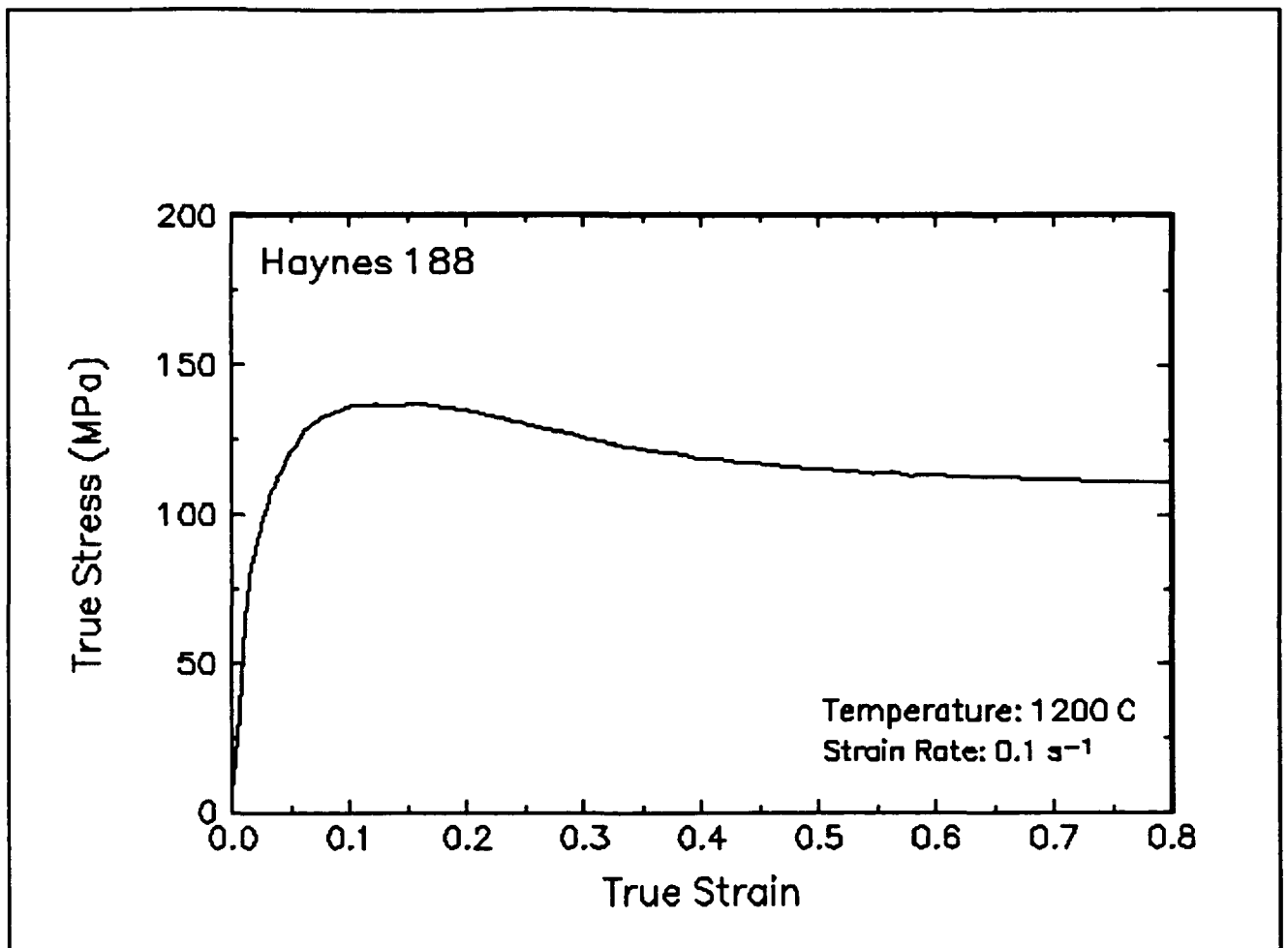
Figure 53. True stress-true strain curve and an optical micrograph from the center of the compressed
sample cut through the compression axis, 1200 and 0.1 s^{-1}.

Figure 54. True stress-true strain curve, 1200 and 0.5 s^{-1}.
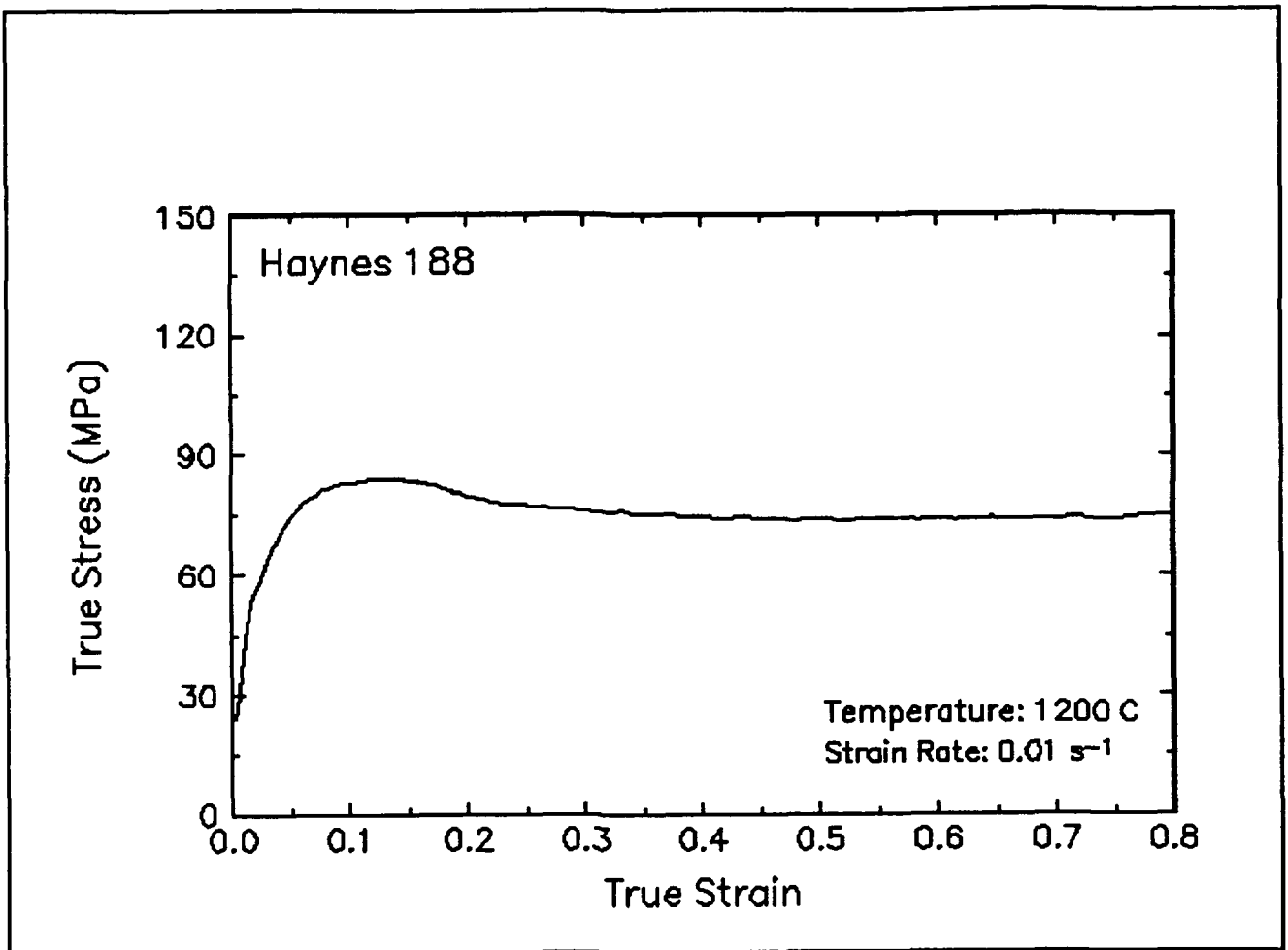
Figure 55. True stress-true strain curve and an optical micrograph from the center of the compressed
sample cut through the compression axis, 1200 and 1 s^{-1}.

Figure 56. True stress-true strain curve, 1200 and 5 s^{-1}.

Figure 57. True stress-true strain curve and an optical micrograph from the center of the compressed sample cut through the compression axis, 1200 and 20 s^{-1}.
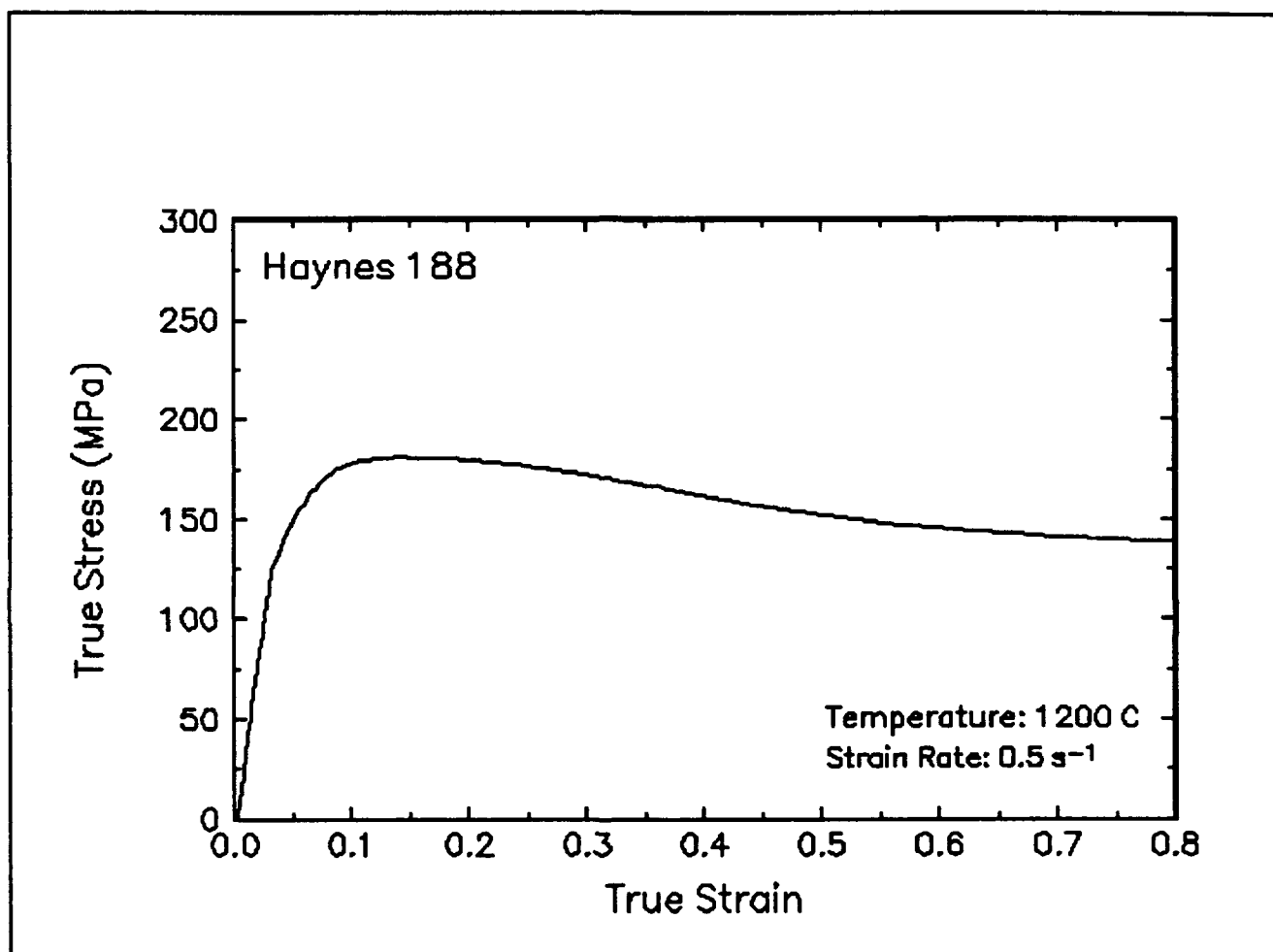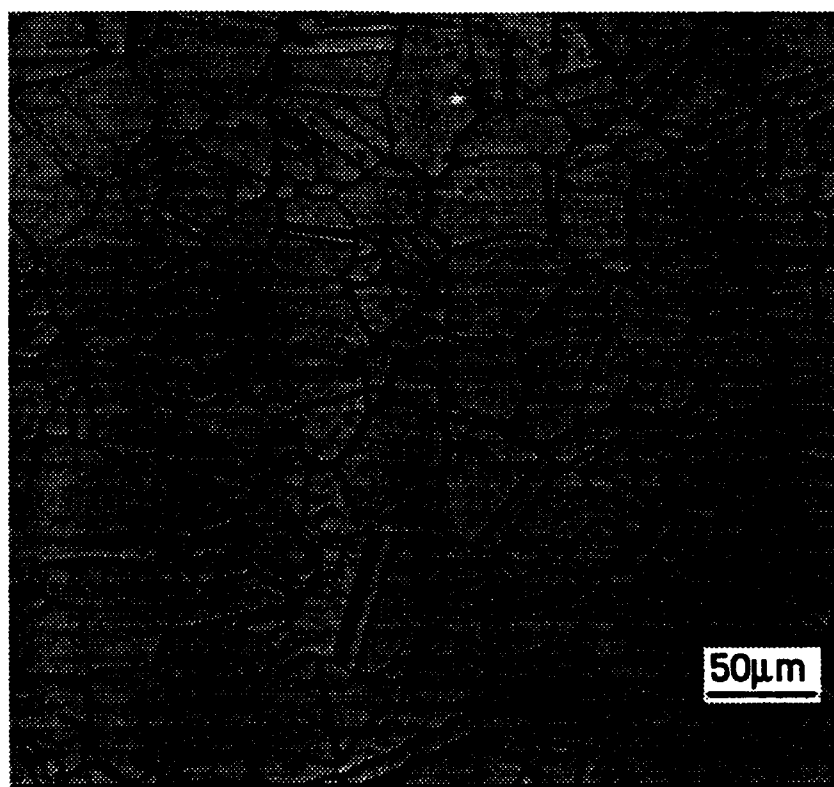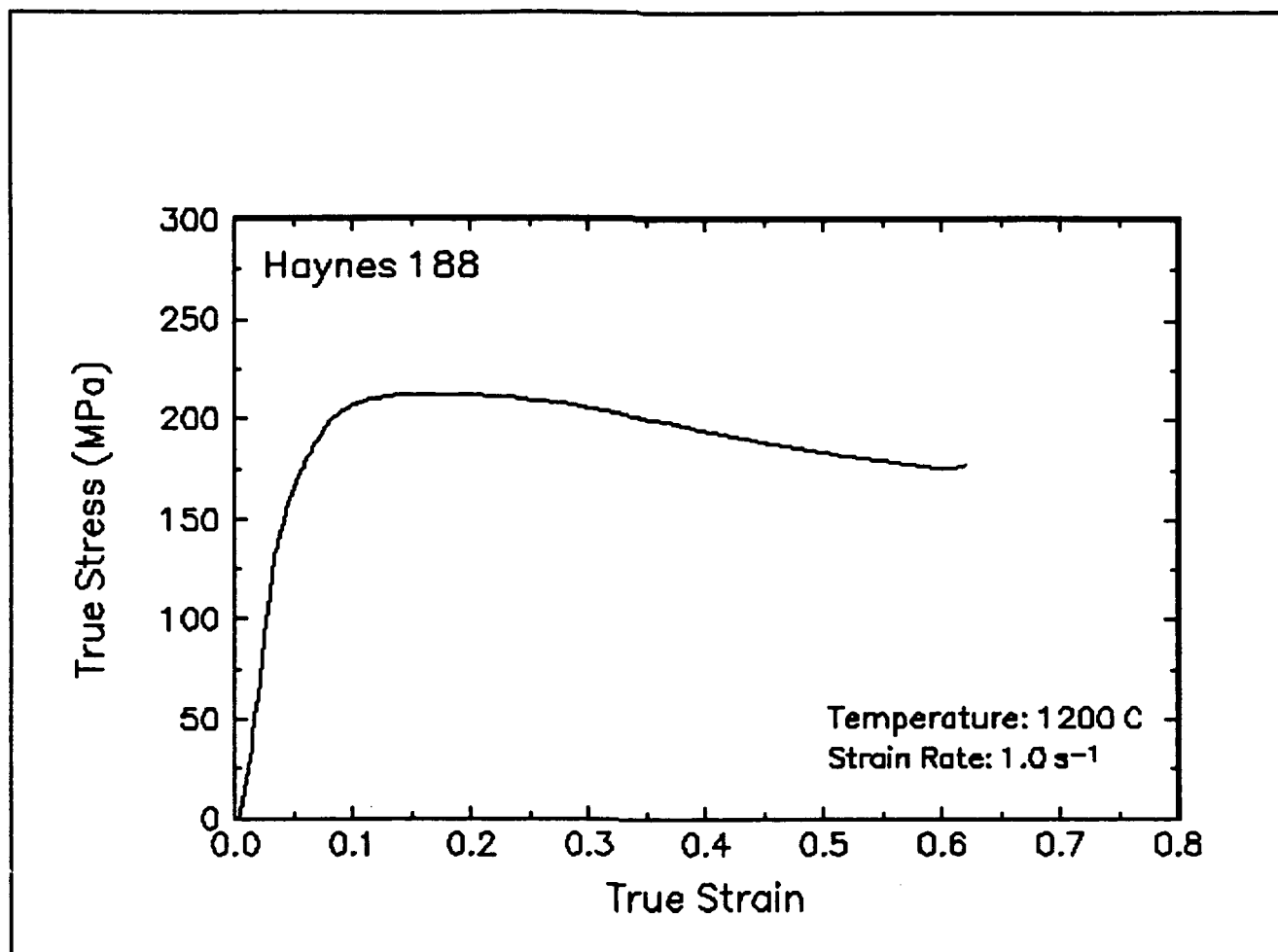
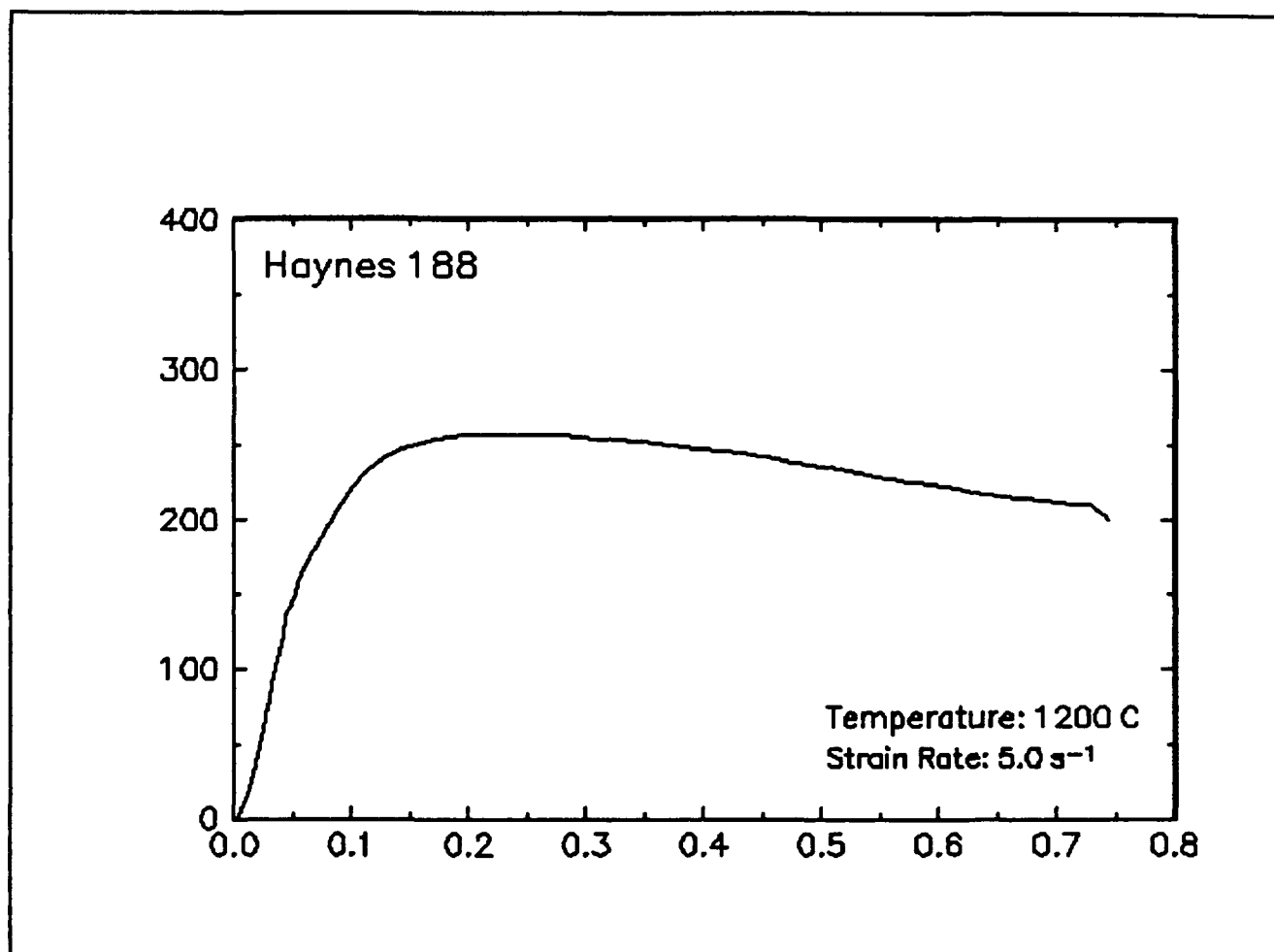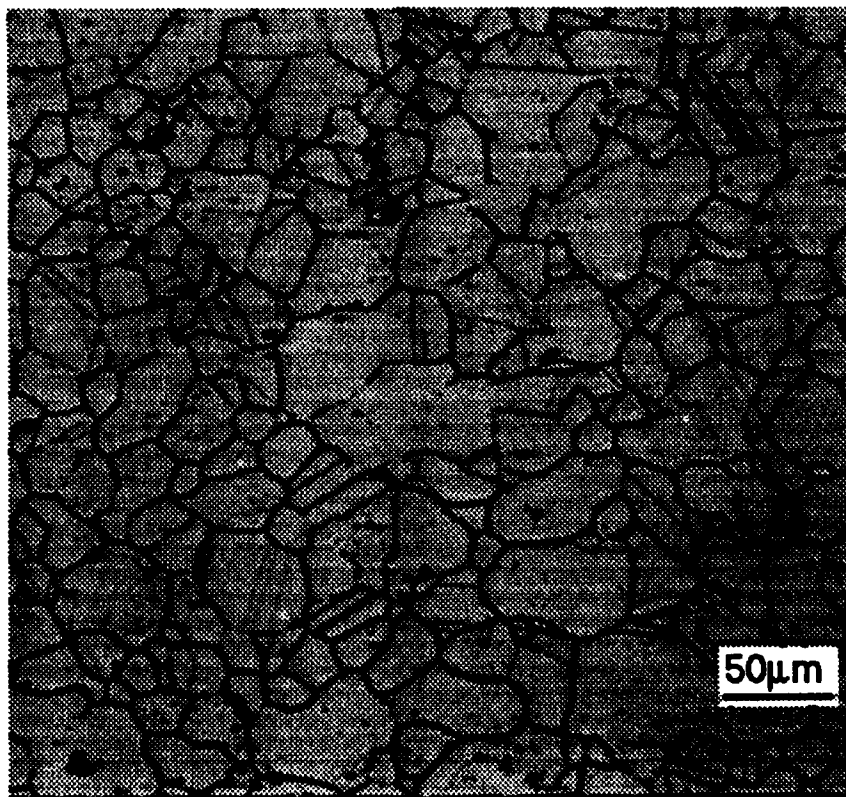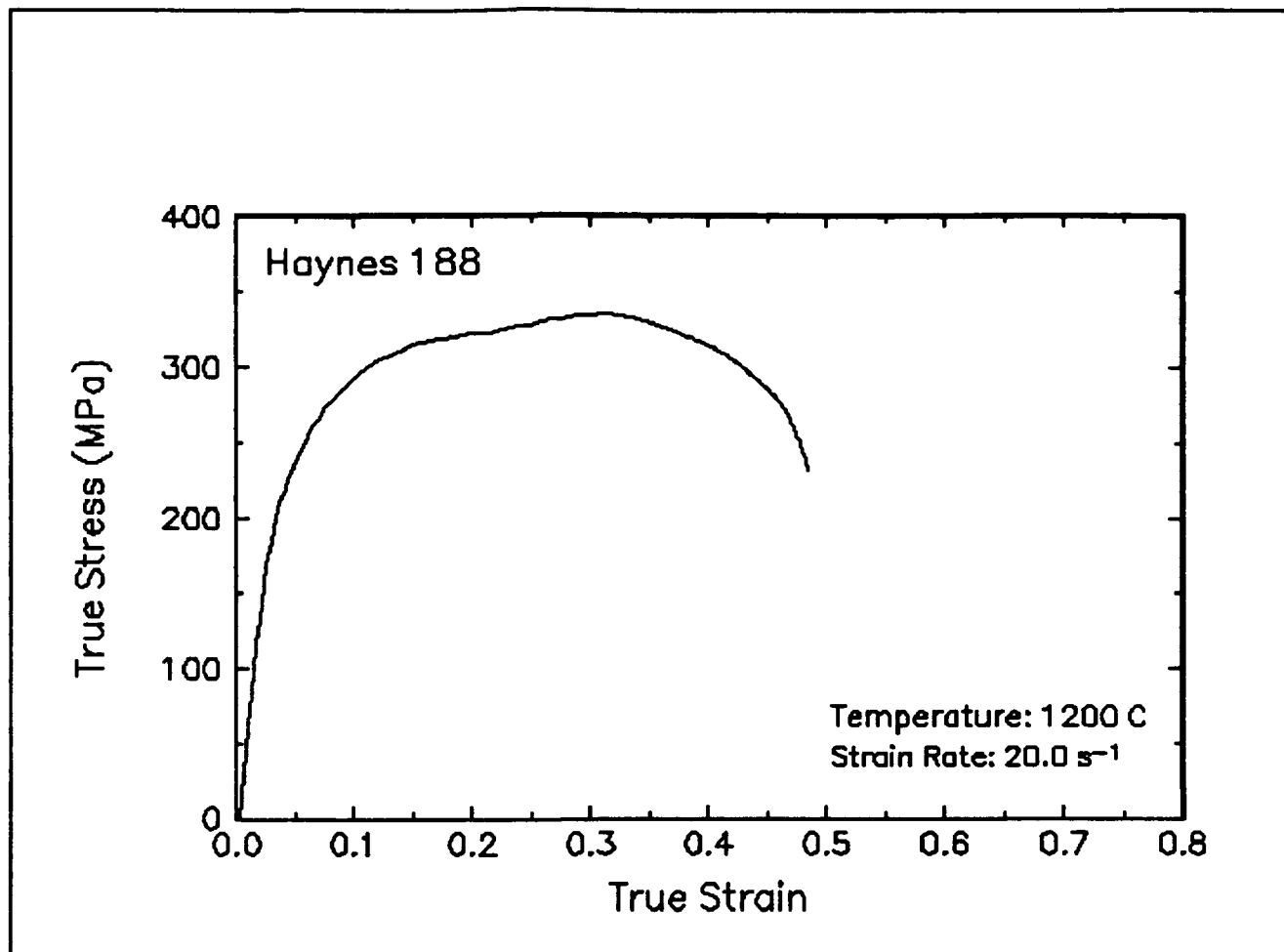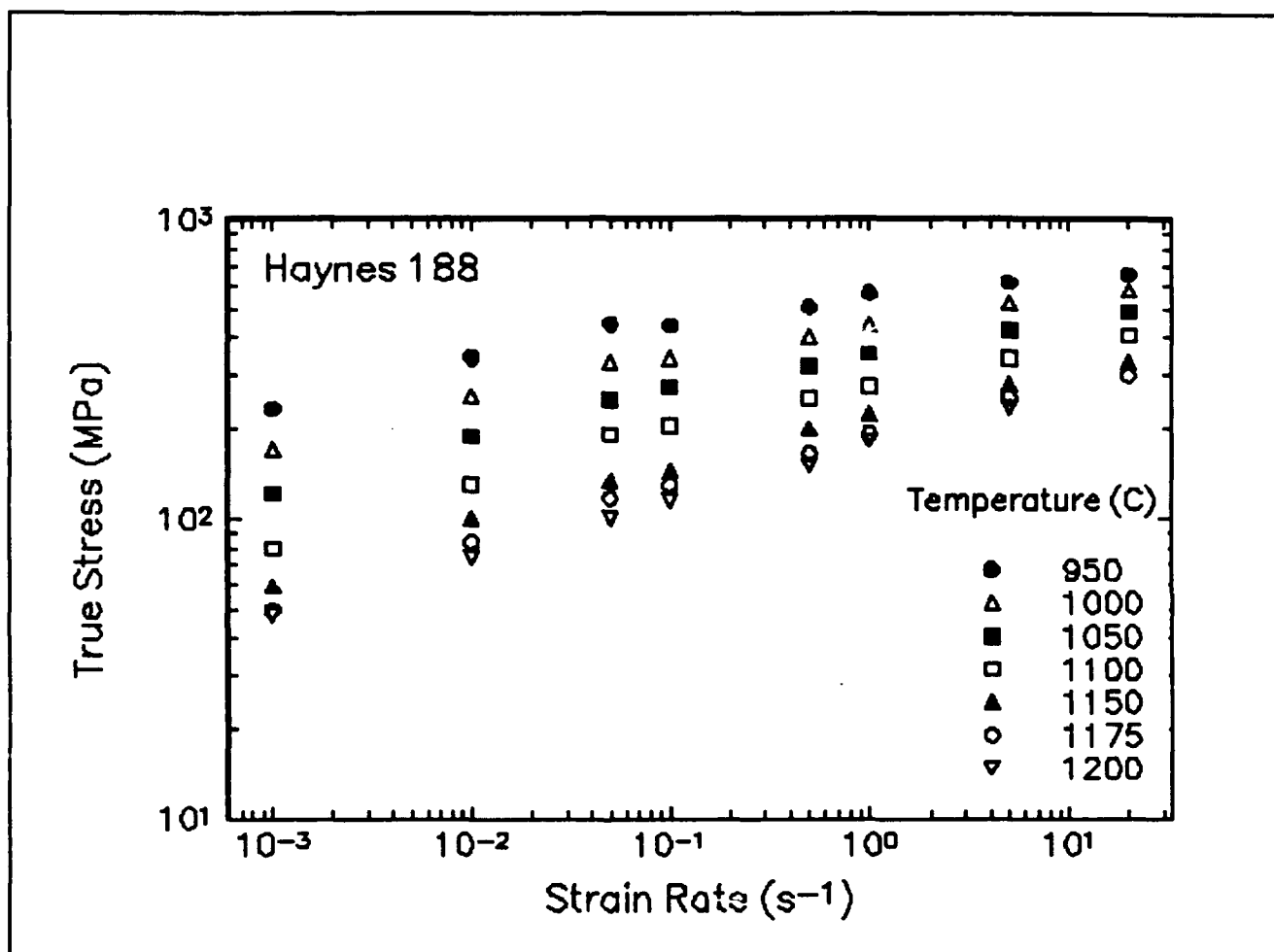Figure 58. Effect of strain rate on stress in log-log scale at a true strain of 0.5 for Haynes 188.
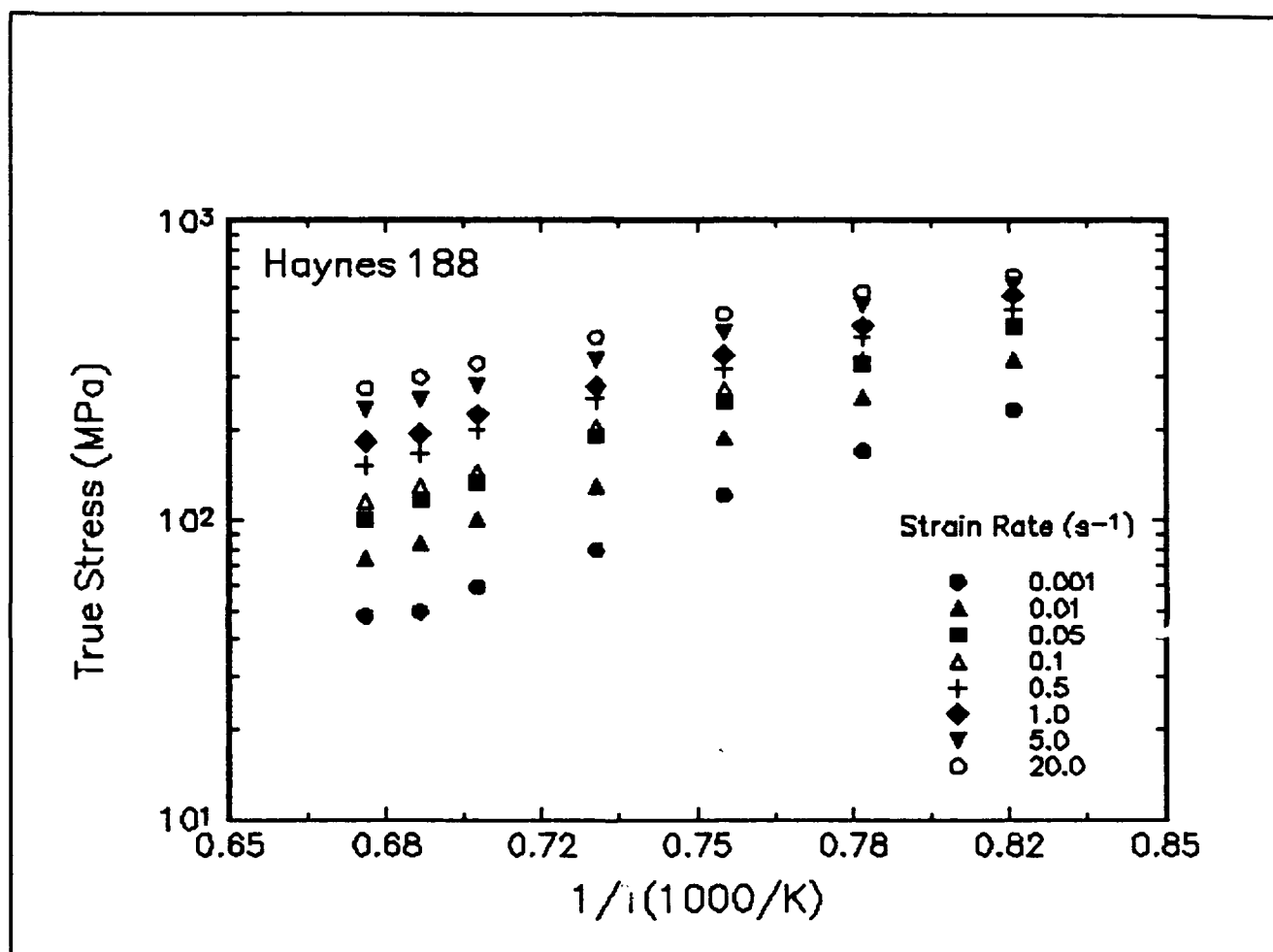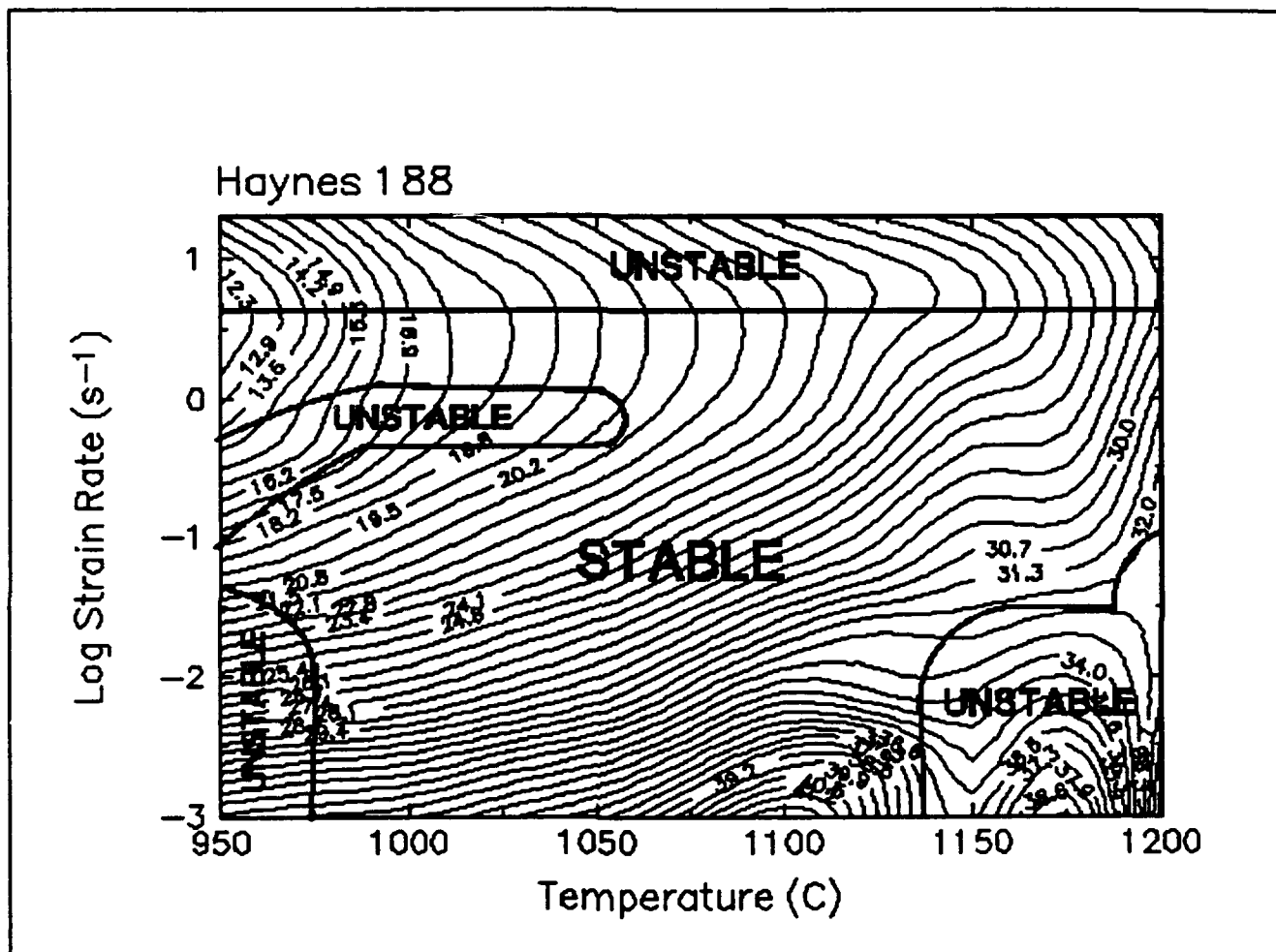
Figure 59. Effect of temperature on stress at a true strain of 0.5 for Haynes 188.

Figure 60. Processing map of Haynes 188 at a true strain of 0.5.

Summary

Compression tests have been performed on Haynes 188 over a wide range of temperatures and strain rates. The experimental conditions used in this work are representative of those in metalworking practice. From the true stress-true strain curves, the flow behavior was characterized and a processing map indicating the optimum processing condition was generated. This condition is 1100 C and 10^{-3} s^{-1}.

The deformed microstructures were characterized from the quenched specimens by optical microscopy and are presented for selective testing conditions together with the stress-strain curves.

Implementation of Data Provided by the Atlas of Formability

The *Atlas of Formability* program provides ample data on flow behavior of various important engineering materials in the temperature and strain rate regime commonly used in metalworking processes. The data are valuable in design and problem solving in metalworking processes of advanced materials. Microstructural changes with temperature and strain rates are also provided in the Bulletin, which helps the design engineer to select processing parameters leading to the desired microstructure.

The data can also be used to construct processing maps using the dynamic material modeling approach to determine stable and unstable regions in terms of temperature and strain rate. The temperature and strain rate combination at the highest efficiency in the stable region provides the optimum processing condition. A processing map has been developed in this Bulletin. In some metalworking processes, such as forging, strain rate varies within the workpiece. An analysis of the process with finite element method (FEM) can ensure that the strain rates at the processing temperature in the whole workpiece fall into the stable regions in the processing map. Furthermore, FEM analysis with the data from the *Atlas of Formability* can be coupled with fracture criteria to predict defect formation in metalworking processes.

The data provided by the *Atlas of Formability* are used in the design of metalworking processes, dynamic material modeling, FEM analysis of metalworking processes, and defect prediction at Concurrent Technologies Corporation. *CTC* can apply its expertise in metalworking area to solve related problems. For more information, please contact Dr. Prabir K. Chaudhury, Manager of Forming Department, by calling (814) 269-2594.